NOAA Technical Report NWS 48

SLOSH: Sea, Lake, and Overland Surges from Hurricanes

Silver Spring, MD
April 1992

UNITED STATES DEPARTMENT OF COMMERCE / National Oceanic and Atmospheric Administration / National Weather Service

NOAA TECHNICAL REPORTS

National Weather Service Series

The National Weather Service (NWS) observes and measures atmospheric phenomena; develops and distributes forecasts of weather conditions and warnings of adverse weather; collects and disseminates weather information to meet the needs of the public and specialized users. The NWS develops the national hydrologic measurements, and forecasts.

NWS series of NOAA Technical Reports is a continuation of the former series, ESSA Technical Report Weather Bureau (WB). Reports listed below are available by accession number (given in parentheses) from the National Technical Information Service, U.S. Department of Commerce, Sills Bldg., 5285 Port Royal Road, Springfield, Virginia 22161, or through the contact person (given in parentheses).

ESSA Technical Reports

WB 1 Monthly Mean 100-, 50-, 30- and 10-Millibar Charts January 1964 through December 1985 of the IQSY Period. Staff, Upper Air Branch, National Meteorological Center, February 1967, 7 p, 96 charts. (AD 651 101)

WB 2 Weekly Synoptic Analysis, 5-, 2-, and 0.4-Mb Surfaces for 1964 (based on observations of the Meteorological Rocket Network during the IQSY). Staff, Upper Air Branch, National Meteorological Center, April 1967, 19 p, 160 charts. (AD 652 696)

WB 3 Weekly Synoptic Analyses, 5-, 2-, and 0.4-Mb Surfaces for 1965 (based on observations of the Meteorological Rocket Network during the IQSY). Staff, Upper Air Branch, National Meteorological Center, August 1976, 173 p. (AD 662 053)

WB 4 The March-May 1965 Floods in the Upper Mississippi, Missouri, and Red River of the North Basins. J. L. H. Paulhus and E. R. Nelson, Office of Hydrology, August 1967, 100 p. (Contact: Ginny Radcliffe, 301-713-0640)

WB 5 Climatological Probabilities of Precipitation for the Conterminous United States. Donald L. Jorgensen, Techniques Development Laboratory, December 1967, 60 p.

WB 6 Climatology of Atlantic Tropical Storms and Hurricanes. M. A. Alaka, Techniques Development Laboratory, May 1968, 18 p.

WB 7 Frequency and Areal Distributions of Tropical Storm Rainfall in the United States Coastal Region of the Gulf of Mexico. Hugo V. Goodyear, Office of Hydrology, July 1968, 33 p. (Contact: Ginny Radcliffe, 301-713-0640)

WB 8 Critical Fire Weather Patterns in the Conterminous United States. Mark J. Schroeder, Weather Bureau, January 1969, 31 p.

WB 9 Weekly Synoptic Analyses, 5-, 2-, and 0.4 Mb Surfaces for 1966 (based on meteorological rocket-sonde and high-level rawinsonde observations). Staff, Upper Air Branch, National Meteorological Center, January 1969, 169 p.

WB 10 Hemispheric Teleconnections of Mean Circulation Anomalies at 700 Millibars. James F. O'Connor, National Meteorological Center, February 1969, 103 p.

WB 11 Monthly Mean 100-, 50-, 30-, and 10-Millibar Charts and Standard Deviation Maps, 1966-1967. Staff, Upper Air Branch, National Meteorological Center, April 1969, 124 p.

WB 12 Weekly Synoptic Analyses, 5-, 2-, and 0.4 Millibar Surfaces for 1967. Staff, Upper Air Branch, National Meteorological Center, January 1970, 169 p.

NOAA Technical Reports

NWS 13 The March-April 1969 Snowmelt Floods in the Red River of the North, Upper Mississippi, and Missouri Basins. Joseph L. H. Paulus, Office of Hydrology, October 1970, 92 p. (COM-71-50269)

NWS 14 Weekly Synoptic Analyses, 5-, 2-, and 0.4-Millibar Surfaces for 1968. Staff, Upper Air Branch, National Meteorological Center, May 1971, 169 p. (COM-71-50383)

NWS 15 Some Climatological Characteristics of Hurricanes and Tropical Storms, Gulf and East Coasts of the United States. Francis P. Ho, Richard W. Schwerdt, and Hugo V. Goodyear, May 1975, 87 p. (COM-7511088)

NWS 16 Storm Tide Frequencies on the South Carolina Coast. Vance A. Myers, June 1975, 79 p. (COM-75-11335)

NWS 17 Estimation of Hurricane Storm Surge in Apalachicola Bay, Florida. James E. Overland, June 1975, 66 p. (COM-75-11332)

NWS 18 Joint Probability Method of Tide Frequency Analysis Applied to Apalachicola Bay and St. George Sound, Florida. Francis P. Ho and Vance A. Myers, November 1975, 43 p. (PB-251123)

NWS 19 A Point Energy and Mass Balance Model of Snow Cover. Eric A. Anderson, February 1976, 150 p. (PB-254653)

NWS 20 Precipitable Water Over the United States, Volume I: Monthly Means. George A. Lott, November 1976, 173 p. (PB-264219)

NWS 20 Precipitable Water Over the United States, Volume II: Semimonthly Maxima. Francis P. Ho and John T. Riedel, July 1979, 359 p. (PB-300870)

(Continued on inside back cover)

NOAA Technical Report NWS 48

SLOSH:
Sea, Lake, and Overland Surges from Hurricanes

Chester P. Jelesnianski, Jye Chen and Wilson A. Shaffer
Office of Systems Development

National Weather Service
Silver Spring, MD
April 1992

UNITED STATES DEPARTMENT OF COMMERCE
Barbara H. Franklin, Secretary

National Oceanic And Atmospheric Administration
John A. Knauss, Under Secretary

National Weather Service
Elbert W. Friday, Jr., Assistant Administrator

TABLE OF CONTENTS

SLOSH

Sea, Lake, and Overland Surges from Hurricanes

by

Chester P. Jelesnianski, Jye Chen, and
Wilson A. Shaffer

Techniques Development Laboratory
Office of Systems Development
National Weather Service, NOAA
Silver Spring, Maryland 20910

ABSTRACT

A numerical-dynamic, tropical storm surge model, SLOSH, was developed for real-time forecasting of hurricane storm surges on continental shelves, across inland water bodies, along coastlines, and for inland routing of water--either from the sea or from inland water bodies. Overtopping of barriers such as levees, dunes, spoil banks, etc. is permitted. Also, channel flow and flow through barrier cuts are entertained. The model is two-dimensional, covering water bodies and inundated terrain. A curvilinear, polar coordinate grid scheme is used.

The model's equations and its sub-grid scale physics are developed. These equations are discretized and applied to the model's polar coordinate system. Attention must be paid to the adaptation of the model to specific geographical locations. The model's terrain and bathymetry must be specified, as well as a description of the sub-grid scale features within the model.

The SLOSH model is run to simulate the flooding caused by an individual hurricane. Since the model is designed for operational forecasting within the National Weather Service, the model's input parameters which describe the hurricane must be relatively simple and predictable. The hurricane's position, size and intensity all enter as input for the model.

Verification runs of the SLOSH model are presented for past hurricanes which have well-documented parameters and observed storm surges. These runs indicate that the accuracy of the model is ±20% when the hurricane is adequately described. In a forecast mode, the accuracy of the track will greatly influence the surge prediction's accuracy.

1. INTRODUCTION

Storm surge is an abnormal rise of water generated by a storm, over and above the predicted astronomical tide. For a hurricane, the surge typically has a duration of several hours and affects about 100 miles of coastline. Hurricane storm surges of over 20 feet have been observed; hurricane Camille in 1969 produced a surge of approximately 24 feet in the area of Gulfport, Miss. The destruction caused by such abnormally high water is truly astounding.

The National Weather Service's (NWS's) problem, of course, is to forecast the surge height well before a hurricane makes landfall. The forecast lead time should exceed the time required to evacuate people from vulnerable low-lying coastal regions to areas of safety. The NWS has this responsibility for any intensity hurricane which may affect its coastline.

Two general approaches can be used to forecast hurricane storm surges--statistical modeling and numerical modeling. In statistical modeling, past observations of storm surge heights are correlated statistically to observed or forecast hurricane characteristics. However, since hurricanes are relatively uncommon and are small scale in nature (compared to synoptic meteorological phenomena), insufficient data exist to allow such statistical correlations to be derived.

Numerical, or computer, modeling offers a viable alternative to statistical modeling for the hurricane storm surge problem. In computer modeling of storm surges, a set of differential equations describing fluid motion and surge height is represented in finite-difference form and applied to a grid mesh covering the forecast area. These finite-difference equations are marched forward in time in small time-steps, starting from a set of initial water-level conditions. Since a finite domain is used to cover the forecast area, boundary values must be imposed along the edges of the domain. In the case of storm surge forecasting, a set of "driving" forces must be specified to represent the surface wind stress and a pressure gradient body force. In modeling terms, such numerical models are referred to as "diagnostic" models (in contrast to true "forecast" models) because they do not forecast a hurricane's movement nor its intensity and radius. The storm surge model diagnoses the storm surge heights when given the hurricane's track and storm characteristics.

Surge modeling is an art. Modelers must decide which finite-difference scheme to use, what physical processes can be dropped from the equations of motion, how to incorporate any sub-grid scale features into the model, how to incorporate a wind model for supplying the driving forces, and how to present a final display of the surge forecast. The modeler must keep foremost in mind the final use of the model and the computer system that the model will run on, since a myriad of possible models can be developed--each having substantial differences and used for different purposes.

The NWS began its efforts in hurricane storm surge modeling with a relatively simple model referred to as SPLASH—the Special Program to List the Amplitudes of Surges from Hurricanes. This model, like several other simple models for computing storm surge, was restricted to a continental shelf only, with the coastline acting as an artificial vertical wall. No flow through the wall is permitted. Such a model can not consider inundation across terrain or surges across inland water bodies (Jelesnianski, 1972; Wanstrath, et. al., 1976). An earlier shelf model by Bodine (1971) was even more restricted. His model required computations carried out on only one seaward line from the coast. Also, the storm track was restricted to being nearly perpendicular to the coast.

The National Weather Service embarked on an effort to develop a more comprehensive model to forecast storm surges which incorporated features not possible with SPLASH. This follow-on model, called SLOSH, for Sea, Lake and Overland Surges from Hurricanes, uses a polar grid system to allow greater resolution in the area of forecast interest, computes surges over bays and estuaries, retains some non-linear terms in the equations of motion, and allows sub-grid scale features such as channels, barriers, and flow of surge up rivers. The SLOSH model was created to run on NWS computers to make real-time, operational forecasts of storm surge heights. Output from the SLOSH model was originally intended to aid forecasters at the NWS's National Hurricane Center in preparing their forecast bulletins. More recently, the model has been used to delineate coastal areas susceptible to hurricane storm surge flooding.

A continuously varying polar grid system was chosen for the SLOSH model. Such a grid system overcomes many of the problems associated with specifying boundary conditions encountered with earlier models. Reid and Bodine (1968) developed a surge model for bays which was limited to the nearby offshore region in shallow waters and a small onshore region. Such models, limited to a small region, force a boundary condition at a region of significant surge activity; e.g., in shallow waters. In this case, boundary conditions are complex and vary in both time and space.

One way of prescribing such boundary values is to extract them from another dynamic surge model. A simple shelf model covering a large basin with a coarse mesh (or even a one-dimensional surge model) is used to compute input boundary values for the limited-area, fine-mesh, bay model. If the two models are dynamically uncoupled, then the approach can be troublesome. The bay is not incorporated in the shelf model, and the computed input boundary values are then suspect.

The use of coarse-mesh models with invariant grid spacing is sometimes permissible to cover an area extending from deep water to high inland terrain, with a bay fully covered by the mesh. Inland, the numerical solution is coarse, but dynamic feedback effects from the bay onto the shelf are approximated. A coarse mesh does not give a detailed description of inland surges across terrain complicated by obstructions and small inland water bodies. However, it can give adequate detail along open coastlines. Only in a gross sense can the inland surge distribution be useful as a guide for forecasting or planning purposes. Such a model could supply boundary values for a fine mesh, limited area surge model.

Instead of limiting an invariant fine mesh to a small region or small basin, the SLOSH model's coordinate system begins as a fine mesh in the limited area nearest the pole point and stretches continuously to a coarse mesh at distant boundaries of a large basin. The geographical area covered by the entire grid is large and there is detailed description over the fine-mesh region. Moreover, in many cases, simple boundary conditions are sufficient. Such a procedure is not limited to a polar grid system, but can use any simple, but continuous, grid transformation from real space onto an image plane.

The SLOSH model incorporates finite amplitude effects but not advective terms in the equations of motion. It uses time-history bottom stress (Platzman, 1963; Jelesnianski, 1967), corrected for finite amplitude effects. The grid system--in Cartesian or image space--is a series of two-dimensional, equal-area squares. Overtopping of barrier systems, levees and roads, is incorporated. Also, inland inundation is permitted by simply turning squares on and off as waters inundate or recede. A few sub-grid size events, such as flow through barrier gaps, adverse river flow, and deep passes between bodies of water, are incorporated via simple hydraulic procedures. Normal river flow and rain are not incorporated at this time because their periods are long and affect the transient surge in only a minor way. River flow upstream could be incorporated as a boundary condition, and rain as a "source", if amenable to quantification with a forecasted storm. Astronomical tide is ignored except for superposition onto the computed surge; it is difficult to phase storm landfall and astronomical tide. A small error in time on track positions will invalidate computations with astronomical tide.

The computed surge is designed to reproduce the time-history amplitude of a long-period, long-gravity wave. Short period phenomena--such as crests and troughs of wind waves, and their periodic "run-up"--are ignored. An example of a surge is a smoothed tide gage hydrograph or stage record. Any non-linear interactions on the surge between the short-period, short-gravity, wind waves are crudely approximated at best. The surge does not break but does partially reflect from the coast; the coastlines are not static and move inland or recede seaward with the surge. Wind waves riding atop the surge break near coastlines with severest action limited to the

nearshore region. The superposition of a train of short period waves on a high surge can be destructive to installations along coastlines, especially so if offshore water depths are deep or descend rapidly, and with breaking wave activity now closer to the original coast.

In coastal regions, the action of breaking waves can create a quasi-steady-state, long period "set-up" (if not a "set-down") whereby the unadulterated storm surge is altered. This wave action can affect bottom stress in shallow waters. Also, exotic effects occur such as an increase of density from suspended sand particles. Along coastal regions, during passage of a tropical storm and onset of inundation, the totality of wind-wave effects on the surge is not well understood or even well observed. Many theoretical studies of an idealized and piecemeal nature, as well as idealized wave tank experiments, have been made. It is not sufficient to correct a computed surge for one or more long term interactions--based solely on guidance from theory or experiment--if other remaining interactions tend to compensate. Accordingly, the SLOSH model lumps the long term interactions into an ad hoc generalized calibration according to observed surge data generated by a multitude of historical storms; that is, the short term action from windwaves is absent but crude approximations for the long term effects may be present. The SLOSH model does give an indication of inland flooding but not the pulsating action of windwaves, such as short term, periodic, sheet flow over barriers. Thus the model can not give perfect answers, but the computed results are useful for forecasting and for planning purposes.

Not to be lightly overlooked in surge modeling is the almost insurmountable difficulty of applying meteorological driving forces on a water surface. The forces are the surface stress and a pressure gradient body force. These must be described in detail, in space and time, to compute a detailed description of surges. A storm wind model is just as important--if not more so--as a surge model.

With SLOSH, the vector field of driving forces on a water surface, with respect to space and time, are determined with a simplified model storm (Jelesnianski and Taylor, 1973). To activate the storm model, simple meteorological parameters are used; no wind input is required. The storm model balances surface forces, including surface friction. Friction coefficients must be specified; these were ascertained empirically, and thus are not physically justifiable. They were set in the model once and for all. Although the wind speed computed by the storm model is sensitive to the friction coefficients, the surge generated by the surge model is not because of compensating effects. The storm model was not designed to accurately forecast surface winds, but to form a vector field of driving forces. The simple, storm input parameters (central pressure, distance from storm center to maximum winds, storm track and speed along track) must, of course, be accurate. In the surge computations, there are compensating effects in surge generation when the surface stress field, via the computed wind field, is inaccurate due to erroneous friction. Strong friction gives weaker winds but more convergence in the wind field, whereas weak friction gives stronger winds but less convergence in the wind field. This bias desensitizes the wind field for surge generation.

The same surface stress formulation and accompanying drag coefficient, as well as other undetermined coefficients, are used in both the shelf model SPLASH (Jelesnianski, 1972) and the SLOSH model. We use a constant drag coefficient, even though it may well be a function of storm, storm track, basin terrain, basin geometry, wind speed, etc. We resist the temptation to treat undetermined coefficients as random or tuning parameters, to be arbitrarily varied in a local region for a historical storm event. Such a procedure will, of course, give an excellent comparison of observed and computed surge for that one storm event. However, there is no guarantee that the same coefficients will do as well for alternate storms and alternate regions. There are large inherent errors, or noise, in both surge and meteorological observations. Hence, determining coefficient values from one storm event is a dangerous procedure. Sometimes the procedure is called calibration or tuning. We prefer, instead, more generalized coefficients to serve all storms in all regions, even if computed results are not ideal for a particular storm event.

In the absence of suitable data to empirically formulate a variable drag coefficient for surface stress, a constant was chosen by comparing observed and computed surges for 43 historical storms (Jelesnianski, 1972). The constant drag coefficient is presently used to forecast or hindcast surges generated by all tropical storms in all basins.

When comparing computed results or models, the calibration dependency needs to be examined. Do the computed values result from a controlled, local calibration for a single storm event or from a generalized calibration? If one storm is used for calibration, it is suspect for verification purposes. Also, are the driving forces computed directly from a storm wind model, or derived from smoothed, analyzed charts of after-the-event observed winds?

The SLOSH model was designed for use in an operational mode: a forecast is run without recourse to a controlled, local calibration or to observed winds. The same values, or functions, for undetermined coefficients in the equations of motion, and the storm wind model, are applied in the same way for both hindsight/verification and operational/forecast runs, regardless of the basin or storm used.

The SLOSH model must be adapted to a given geographical area (the "basin") before it can be run. The basin accommodates some or all of the following: 1) inland terrain, 2) inland water bodies such as lakes, bays, and estuaries, and 3) a segment of a continental shelf.

Near the coastline, terrain is usually complicated by numerous vertical obstructions such as dunes, ridge lines, levees, railroads, spoil banks, and other barriers of long horizontal extent. Offshore, there may be barrier islands, reefs, etc. These natural and man-made abutments protect inland terrain against encroachment from the sea. However, when an offshore surge is high enough to overtop barriers, then water can penetrate inland until impeded by other barriers further inland or by naturally rising terrain. It is possible for a tropical storm to produce massive inundation across low lying terrain for many miles inland.

Across inland terrain, there may be shallow or deep water bodies such as lakes, bays, or estuaries. Deep channels may connect them to other water bodies or the sea. An inland water body, far removed from the coast, can respond to storm driving forces and channel flow, even in the absence of direct inundation from the sea.

To compute surges with a surge model and a constructed input basin, complicated input boundary values may be required as a function of time. An exception is a basin for an isolated lake, unconnected to and unaffected by events in any other body of water. Boundary inputs can be partially relaxed if a portion of the basin's boundary lies in deep waters, with the remaining portions in shallow waters or on high terrain. Now, if the core of a storm crosses (or exits) the basin through deep waters of a boundary, and exits (or crosses) through high terrain, then simple boundary conditions may be adequate throughout.

Computed surge and wind were compared on Lake Okeechobee, Florida, for the 1949 storm. To date, this storm's time dependent surge and surface wind observations are the most dense and abundant in the world. For SLOSH model simulations in the Lake Okeechobee basin, a fine, invariant mesh of one-mile spacing between surge points was used. The basin area is small, barely exceeding the lake area, but does encompass all surge activity.

Comparisons of the computed surge for four historical storms have been made with observed surges on Lake Pontchartrain, Louisiana, the surrounding inland terrain, the surrounding lakes, and the nearby coasts along the Gulf of Mexico. A coarse mesh (4-mile spacings between height points) and a variable mesh (1-4 mile spacings) were used, separately, for the storm events. The basin for each mesh was large in area. In general, the two computed surges varied little with grid size, but there was more detail in the fine grid region of the variable mesh.

Comparisons of the computed surge, for a variable grid and a basin of large areal extent, were made for Galveston Bay, Texas, and surrounding terrain with observed surges generated by Hurricane Carla, 1961, and the 1949 hurricane.

Comparisons of computed and observed surges have been made for several other basins not included in this report; results are similar. Basin preparation and verification with historical storms is an ongoing project in the National Weather Service of NOAA. Improvements and techniques in the SLOSH surge model are continually evolving and being updated. Some of the material in this report may already be out of date and superseded.

2. THE EQUATIONS OF MOTION

a. The Equations of Motion on a Cartesian Frame of Reference

The transport equations of motion on a Cartesian frame of reference are derived in Appendix A. These equations are:

$$\frac{\partial U}{\partial t} = -g(D+h)\left[B_r\frac{\partial(h-h_o)}{\partial x} - B_i\frac{\partial(h-h_o)}{\partial y}\right]+f(A_rV+A_iU)+C_r{}^{x}{}_{\tau}-C_i{}^{y}{}_{\tau}$$

$$\frac{\partial V}{\partial t} = -g(D+h)\left[B_r\frac{\partial(h-h_o)}{\partial y} + B_i\frac{\partial(h-h_o)}{\partial x}\right]-f(A_rU-A_iV)+C_r{}^{y}{}_{\tau}+C_i{}^{x}{}_{\tau} \qquad (1)$$

$$\frac{\partial h}{\partial t} = -\frac{\partial U}{\partial x} - \frac{\partial V}{\partial y}$$

where

U,V	= components of transport
g	= gravitational constant
D	= depth of quiescent water relative to a common datum
h	= height of water above datum
h_o	= hydrostatic water height
f^o	= Coriolis parameter
x_τ, y_τ	= components of surface stress
$A_r,\ldots,C_i$	= bottom stress terms

These equations were developed by Platzman (1963) and modified with a bottom slip coefficient by Jelesnianski (1967). They are presently designed to include a finite amplitude effect with D replaced by the instantaneous or total depth, D+h. The friction terms $A_r,\ldots,C_i$ are functions of the total depth. The equations are different from those used in many other studies where bottom stress is of the Chezy or Manning type (Chow, 1959).

Advective terms are ignored (Whitaker, et al., 1975). Depending on the Rossby number, the Coriolis term can also be omitted for lakes and inland inundation. However, this term is retained in case surge amplitudes become extraordinarily large in lakes or if inundation covers a large inland area, (see Appendix B).

A horizontal viscosity term can also be included. The effects of this term are small compared to the effect of vertical viscosity. In general, horizontal viscosity has little effect on the surge. However, it does partly ameliorate computational waves of two grid lengths and can be used for this purpose.

Much theoretical effort can be expended on the equations of motion, computational methods, and grid type when designing a surge model. These are not the only--nor even main--themes for a

surge model. There are hidden demons of omission and commission in the equations of motion that are generally dealt with empirically. These demons have as much to say about surge generation as any theoretical and computational aspects of the equations of motion. An example is the surface stress or meteorological driving forces. Merely writing it down as " τ " and assuming an outside arbiter will supply it is not realistic.

A storm wind model must be used to generate the necessary driving forces. It is just as difficult--if not more so--to design a storm model as a surge model. Hidden in " τ " and the bottom stress are undetermined coefficients; these are set empirically through comparisons of computed and observed meteorological and surge data from a multitude of historical storm events.

The depths required by the model--topography over land, bathymetry under seas, vertical barriers and channels--must be obtained and reduced to a common datum. Compiling the depth data is not a simple process; it requires the skill and experienced artistry of a modeler familiar with the model and its requirements.

The equations of motion for a surge wave always have some simplifications for computational convenience; they are not complete for specialized phenomena such as weir flow, overtopping of barriers, and onset or ebbing of inland inundation. Special techniques or refurbishment of the equations are required to handle such special situations.

b. The Equations of Motion in an Arbitrary, Conformal, Frame of Reference

There are computational benefits to transforming the equations of motion from their Cartesian grid into a non-Cartesian grid system. Although the transformed equations appear more complicated, they have useful properties which can be exploited for economy in numerical computations.

It is convenient to rewrite the equations of motion (1) with the hydrostatic height; h_o, absorbed in the stress terms ^{x}T, ^{y}T. With the following identities:

$$z = x + iy$$

$$W = U + iV,\ U = \frac{1}{2}(W+W^*),\ V = \frac{1}{2i}(W-W^*)$$

$$\frac{\partial}{\partial x} = \frac{\partial}{\partial z} + \frac{\partial}{\partial z^*}\ ,\ \frac{\partial}{\partial y} = i\left(\frac{\partial}{\partial z} - \frac{\partial}{\partial z^*}\right) \qquad (2)$$

$$\frac{\partial}{\partial z} = \frac{1}{2}\left(\frac{\partial}{\partial x} - i\frac{\partial}{\partial y}\right)\ ,\ \frac{\partial}{\partial z^*} = \frac{1}{2}\left(\frac{\partial}{\partial x} + i\frac{\partial}{\partial y}\right)$$

where "*" denotes the complex conjugate, the third equation in (1), the continuity equation, becomes

$$\frac{\partial h}{\partial t} = -\left(\frac{\partial}{\partial z} + \frac{\partial}{\partial z^*}\right)\frac{1}{2}(W+W^*) - \left(\frac{\partial}{\partial z} - \frac{\partial}{\partial z^*}\right)\frac{1}{2}(W-W^*)$$

or,

$$\frac{\partial h}{\partial t} = -\left[\frac{\partial W}{\partial z} + \left(\frac{\partial W}{\partial z}\right)^*\right] \qquad (3)$$

In Eqs. (1), we can also substitute the forms $A = A_r + iA_i$, $B = B_r + iB_i$, $C = C_r + iC_i$ and $T = {}^{x}T + i\,{}^{y}T$. The first two equations of (1) can now be combined into one equation in complex form, by using Eq. (2), as

$$\frac{\partial W}{\partial t} = -\,g(D+h)2B\,\frac{\partial h}{\partial z^*} - ifAW + T \qquad (4)$$

We can now consider a general, conformal transformation as,

$$\zeta = F(z) = P + iQ \qquad (5)$$

where " ζ " is analytic and $\frac{d\zeta}{dz^*} = \frac{d\zeta^*}{dz} = 0$. It is convenient to use the following identities,

$$P = \frac{1}{2}(\zeta+\zeta^*)\ ,\ Q = \frac{1}{2i}(\zeta-\zeta^*)$$

$$\frac{\partial}{\partial z} = \frac{\partial P}{\partial z}\frac{\partial}{\partial P} + \frac{\partial Q}{\partial z}\frac{\partial}{\partial Q}$$

$$= \frac{1}{2}\frac{d}{dz}(\zeta+\zeta^*)\frac{\partial}{\partial P} + \frac{1}{2i}\frac{d}{dz}(\zeta+\zeta^*)\frac{\partial}{\partial Q}$$

$$= \frac{1}{2}\frac{d\zeta}{dz}\left(\frac{\partial}{\partial P} - i\frac{\partial}{\partial Q}\right) \qquad (6)$$

$$\frac{\partial}{\partial z^*} = \frac{1}{2}\left(\frac{d\zeta}{dz}\right)^*\left(\frac{\partial}{\partial P} + i\frac{\partial}{\partial Q}\right)$$

$$\frac{\partial}{\partial P} = \frac{\partial\zeta}{\partial P}\frac{\partial}{\partial\zeta} + \frac{\partial\zeta^*}{\partial P}\frac{\partial}{\partial\zeta^*} = \frac{\partial}{\partial\zeta} + \frac{\partial}{\partial\zeta^*}$$

$$\frac{\partial}{\partial Q} = i\left(\frac{\partial}{\partial\zeta} - \frac{\partial}{\partial\zeta^*}\right)$$

$$\frac{\partial}{\partial\zeta} = \frac{1}{2}\left(\frac{\partial}{\partial P} - i\frac{\partial}{\partial Q}\right)\ ,\ \frac{\partial}{\partial\zeta^*} = \frac{1}{2}\left(\frac{\partial}{\partial P} + i\frac{\partial}{\partial Q}\right)$$

Rearranging Eqs.(6) yields

$$\frac{\partial}{\partial z} = \frac{1}{2}\frac{d\zeta}{dz}\left[\frac{\partial}{\partial\zeta} + \frac{\partial}{\partial\zeta^*} - i(i)\left(\frac{\partial}{\partial\zeta} - \frac{\partial}{\partial\zeta^*}\right)\right] = \frac{d\zeta}{dz}\frac{\partial}{\partial\zeta} \qquad (7)$$

$$\frac{\partial}{\partial z^*} = \left(\frac{d\zeta}{dz}\right)^*\frac{\partial}{\partial\zeta^*}$$

Applying Eq. (7) to Eq. (3) gives

$$\frac{\partial h}{\partial t} = -\left[\frac{d\zeta}{dz}\frac{\partial W}{\partial\zeta} + \left(\frac{d\zeta}{dz}\right)^*\left(\frac{\partial W}{\partial\zeta}\right)^*\right] \qquad (8)$$

and Eq. (4) becomes

$$\frac{\partial W}{\partial t} = -g(D+h)2B\left(\frac{d\zeta}{dz}\right)^*\frac{\partial h}{\partial\zeta^*} - ifAW + T \qquad (9)$$

It is convenient to use the following form

$$\mathcal{W} = \left(\frac{dz}{d\zeta}\right)^* W \qquad (10)$$

Then Eq. (8) becomes

$$\frac{\partial h}{\partial t} = -\frac{d\zeta}{dz}\frac{\partial}{\partial \zeta}\left[\left(\frac{d\zeta}{dz}\right)^* W\right] - \left(\frac{d\zeta}{dz}\right)^* \frac{\partial}{\partial \zeta^*}\left[\frac{d\zeta}{dz} W^*\right]$$
$$= -\left|\frac{d\zeta}{dz}\right|^2 \left[\frac{\partial W}{\partial \zeta} + \left(\frac{\partial W}{\partial \zeta}\right)^*\right] \qquad (11)$$

on noting that

$$\frac{d}{d\zeta}\left(\frac{d\zeta}{dz}\right)^* = \frac{d}{d\zeta^*}\frac{d\zeta}{dz} = 0$$

In component form, Eq. (10) is expressed as $W = U + iV$. Using Eq. (6) in Eq. (11) yields

$$\frac{\partial h}{\partial t} = -\left|\frac{d\zeta}{dz}\right|^2 \tfrac{1}{2}\left[\frac{\partial}{\partial P}(U + iV) - i\frac{\partial}{\partial Q}(U + iV)\right.$$
$$\left. + \frac{\partial}{\partial P}(U - iV) + i\frac{\partial}{\partial Q}(U - iV)\right]$$

or

$$\frac{\partial h}{\partial t} = -\left|\frac{d\zeta}{dz}\right|^2 \left(\frac{\partial U}{\partial P} + \frac{\partial V}{\partial Q}\right) \qquad (12)$$

which is the same format as the third equation of (1), except for the Jacobian, $\left|\frac{d\zeta}{dz}\right|^2$

Equation (9) can be rewritten as,

$$\frac{\partial W}{\partial t} = -\,g(D+h)B\left[\left(\frac{\partial}{\partial P} + i\frac{\partial}{\partial Q}\right)h\right] - ifAW + \left(\frac{dz}{d\zeta}\right)^* T$$

since $\left|\frac{d\zeta}{dz}\right|^2$ is independent of time. This can be expressed in component form as

$$\frac{\partial U}{\partial t} = -g(D+h)\left(B_r\frac{\partial h}{\partial P} - B_i\frac{\partial h}{\partial Q}\right) + f(A_r V + A_i U)$$
$$+\left[Re\left(\frac{dz}{d\zeta}\right)^*\right] x_T - \left[Im\left(\frac{dz}{d\zeta}\right)^*\right] y_T$$
$$\frac{\partial V}{\partial t} = -g(D+h)\left(B_r\frac{\partial h}{\partial Q} + B_i\frac{\partial h}{\partial P}\right) - f(A_r U - A_i V) \qquad (13)$$
$$+\left[Re\left(\frac{dz}{d\zeta}\right)^*\right] y_T + \left[Im\left(\frac{dz}{d\zeta}\right)^*\right] x_T$$

where

$$x_T = g(D+h)\left[B_r\frac{\partial h_o}{\partial x} - B_i\frac{\partial h_o}{\partial y}\right] + C_r x_\tau - C_i y_\tau \qquad (13a)$$

$$y_T = g(D+h)\left[B_r\frac{\partial h_o}{\partial y} + B_i\frac{\partial h_o}{\partial x}\right] + C_r y_\tau + C_i x_\tau$$

Notice that the stress terms are kept in their original Cartesian form for computational convenience.

Equations (13) and (12) are similar to Eq. (1) except for the Jacobian $|d\zeta/dz|^2$ in the continuity equation (12), and the conjugate of the complex magnification factor, $(d\zeta/dz)^*$, in the stress terms of momentum equations (13); the components of W, (U,V), are given by Eq. (10).

c. The Equations of Motion on a Polar Frame of Reference

If the general transformation, Eq. (5), is particularized by

$$\zeta = \ln(z/R_0) = P + iQ = \ln(r/R_0) + i\theta \qquad (14)$$

where R_o is a convenient scale, then we have a stretched grid that increases or magnifies with r. This is a particularly useful transformation because the Jacobian of the transformation depends on only r, not θ, so that the stretching can then be controlled by R_o. From

$$\frac{d\zeta}{dz} = \frac{1}{z}, \quad \frac{dz}{d\zeta} = re^{i\theta}, \quad \left|\frac{dz}{d\zeta}\right|^2 = r^2$$
$$Re\left(\frac{dz}{d\zeta}\right)^* = r\cos\theta, \quad Im\left(\frac{dz}{d\zeta}\right)^* = -r\sin\theta \qquad (15)$$

and the equations of motion, (13) and (12) become

$$\frac{\partial U}{\partial t} = -g(D+h)\left(B_r\frac{\partial h}{\partial P} - B_i\frac{\partial h}{\partial Q}\right) + f(A_r V + A_i U)$$
$$+ r[\cos\theta\ x_T + \sin\theta\ y_T]$$
$$\frac{\partial V}{\partial t} = -g(D+h)\left(B_r\frac{\partial h}{\partial Q} + B_i\frac{\partial h}{\partial P}\right) - f(A_r U - A_i V) \qquad (16)$$
$$+ r[\cos\theta\ y_T - \sin\theta\ x_T]$$
$$\frac{\partial h}{\partial t} = -\frac{1}{r^2}\left(\frac{\partial U}{\partial P} + \frac{\partial V}{\partial Q}\right)$$

The transformation Eq. (14) maps a polar grid onto an image plane, Fig. 1. The (P,Q) system of Fig. 1 is non-dimensional. It is convenient to set $\Delta P = \Delta Q = \Delta\theta$. This assumption gives a set of equally spaced, mutually orthogonal lines. To do so, suppose a circular arc of distance $\Delta s = R_o \Delta\theta$ is chosen on the circle R_o. Suppose further there are points

$$N = \ldots,-n,-n+1,\ldots\ldots,-1,0,1,2,\ldots\ldots,n,n+1,\ldots.$$

on any ray from the origin of Fig. 1, with R_o positioned at N = 0. Then at N = 0,

$$\Delta P = \ln(R_1/R_0) - \ln(R_0/R_0) = \ln(R_1/R_0). \qquad (17)$$

Similarly,

$$\Delta P = \ln(R_n/R_{n-1}), \qquad (18)$$

hence, for ΔP constant, the discrete circles are then positioned with respect to the polar origin at

$$R_n = R_{n-1}e^{\Delta P} = R_0 e^{n\Delta P} \qquad (19)$$

Since P is non-dimensional, we choose $\Delta Q = \Delta P = \Delta\theta$ where $\Delta\theta = \Delta s/R_o$ is to be specified.

When the transformed equations of motion (16) are used with the (P,Q) grid on the image plane, Fig. 1, the computations are only slightly different compared to the equations of motion (1) on a Cartesian frame. The continuity equation has an extra multiplication by the Jacobian, r^{-2}. The Jacobian depends on r but not θ, and can be programmed as a table lookup at discrete R_n points with only a small increase in computer memory. In each of the momentum equations of (16), there are extra multiplications by the components of the complex magnification and rotation factor (cos θ, sin θ) and one extra addition. The harmonics cos θ and sin θ are at discrete intervals on the grid and similarly for r at distances R_n on a ray. Since the variables r and θ are separated, the extra computer memory required for table lookups is minor. The extra computations involved with Eq. (16) are minor compared to the total required.

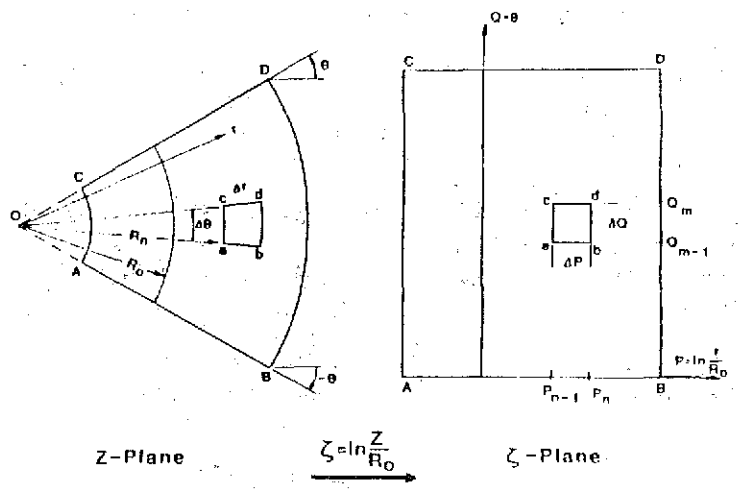

Figure 1. Transforming an (R,θ), unequally spaced polar grid in the Z-Plane onto an (P,Q), equally spaced, rectangular grid in the -Plane.

For practical applications, a plane with polar coordinates is placed tangent to the earth, usually at the entrance of a bay or estuary. The earth is represented as a Clark ellipsoid and is projected conformally onto the polar grid for geographical orientation. A grid distance Δs and circle of radius R_o are pre-selected at the tangent point; R_o and Δs determine $\Delta\theta$ through $\Delta\theta = \Delta s/R_o$. The ray direction from the tangent point to the origin of the polar grid is arbitrary, e.g., along the major axis of an estuary. To maintain constant grid spacing in the image plane, the geographical spacing on the polar grid is compressed as one moves from the tangent point to the pole and stretched when one moves in the opposite direction. Thus, this is a continuous and monotonic variation of geographical spacing on the polar grid. Placement and orientation of the polar grid on the Clark ellipsoid allow the area of fine grid mesh to cover a particular area of interest.

3. MODEL COEFFICIENTS

The final product of a surge model consists of still-water, surge heights, with the short period wind waves filtered out. All subsidiary fields--such as internal currents, surface and bottom currents, and surface stress--serve only as means to that end; that is, surge computations. The surge height, in general, is much more conservative than other fields. Hence, surge computations may be adequate even though other computed fields may have considerable error. If a surge model is used with meteorological input parameters, and if high accuracy for the surge computations is not required, then it is possible to compute coarse, but useful, surge values for coastal and inland regions.

In any surge model there are undetermined coefficients which must be specified. For the SPLASH and SLOSH surge models, these are:

C_D, the surface drag coefficient
ν, vertical eddy viscosity coefficient
and s, bottom slip coefficient.

For the storm wind model within SLOSH, there are additional undetermined coefficients:

k_s, wind friction coefficient in the tangential direction
and k_n, wind friction coefficient in the radial direction.

In addition, the SLOSH model has subsidiary coefficients for non-linear channel flow and horizontal viscosity. Other surge models may use different physical approaches, with alternate types of coefficients--e.g., Manning or Chezy friction coefficients for bottom stress. Other storm models may use different physical approaches, such as an empirical decrease of gradient winds due to friction and empirical or arbitrarily specified inflow angles.

Extreme caution should be exercised in specifying such undetermined coefficients. Coefficient values could be chosen to bring observations and forecast surges into agreement for one storm event in a particular area. This approach is especially tempting if observed data are limited. Such a practice is particularly dangerous if there are more unknown coefficients than available data permits. There is no guarantee that the same coefficients will hold for alternate storms, storm tracks, or basins.

Measurements of meteorological storm parameters and surge heights frequently exhibit large errors. The character of a storm--strength and size--and its track are not precisely known, even from post-storm analysis. The still-water surge height measured by a stilling gage is the most accurate surge measurement available. High water marks are inherently inaccurate. Although the surveying procedures for measuring high water marks inside buildings are accurate, the stilling action of the buildings is questionable; e.g., the data are not necessarily still-water surge heights. Any model calibration for a single storm event may hide observational errors within the chosen coefficient values.

To date there are insufficient, simultaneously-observed data of storm parameters, storm track, and surge heights to statistically assemble precise values for the unknown coefficients. Nor are there sufficient data to vary the coefficients for feedback effects from local terrain,

changing storm parameters, or tides. The SPLASH and SLOSH procedures preset values for some of the coefficients, providing the resulting computed surge is insensitive or only mildly sensitive to these coefficients. The remaining coefficients are set empirically from comparisons of computed and observed surges, while taking into account empirical sensitivity checks.

The storm friction coefficients are arbitrarily preset as

$$k_s = 1.15\ k_n = \alpha\left[\frac{10^{-4}R}{0.3V_R+60}\right]^{1/2}, \qquad (20)$$

where R = radius of maximum winds in stature miles, V_R=maximum wind speed in mph for a stationary storm, and $\alpha = 1$ for ocean winds, and $\alpha = 4\sqrt{22/R}$ for lake winds. The maximum wind is not an input parameter. Instead, it is computed from the storm's pressure drop, Δp, and size, R. Equation (20) is based on empirical studies of many past hurricanes, but lacks a physical basis. The resulting computed winds frequently disagree with observations.

The storm friction coefficients were not designed with any intention to give an accurate wind speed field; their design has conservative properties for surge computations with the SPLASH/SLOSH equations of motion. The storm wind model balances forces. Hence, strong friction gives weak winds with strong convergence (large inflow across pressure isobars), whereas weak friction yields strong winds with weak convergence of the wind field. These properties have compensating effects on the surge. Although large frictional changes give large changes for the absolute surface stress or the computed wind speed, it does not mean large changes for the computed surge. The computed surge is only mildly sensitive to Eq. (20). If storm forces are balanced, it is not necessary to have an accurate maximum wind value or wind speed field for a given storm. However, it is necessary to accurately specify storm parameters--the pressure drop, storm size, and storm track. It is doubtful that any present-day storm model can accurately portray a surface vector-wind field for all storms, for any geographical area, with simple input storm parameters as input.

Classical bottom stress formulations--such as Manning or Chezy--are not used in the SPLASH and SLOSH surge models except for sub-grid sized phenomena, such as channel flow. Instead, Ekman formulations are used with invariant eddy viscosity and slip coefficients for all storms and in all geographical regions. With a fast moving storm (>20 mph), empirical tests with the SPLASH model generate a storm surge (forced wave) that is insensitive to large changes in bottom stress coefficients.

If a fast-moving storm landfalls or moves alongshore, and if waters just offshore are deep or intermediate in depth, then a surge model need not include bottom stress to compute peak coastal surges associated with the storm. In some cases, however, after passage of an alongshore moving storm, secondary, or free, waves are generated. These waves are trapped between the nearshore region and the coast, and are sensitive to bottom stress. Such a two-part phenomena, one part insensitive to bottom stress and the other part sensitive to bottom stress, is used to empirically determine approximate values for the eddy and slip coefficients.

There were three historical, alongshore-moving storms with adequate meteorological and surge data for such tests--September 1944, Carol 1956, and Donna 1960. Each generated a forced wave during its passage and free waves after its passage. A tide gage was operative just offshore at Atlantic City, New Jersey during and after each of these storm's passage. All three storms were traveling at high speed (>30 mph). The waters just offshore are deep (>25 foot depths). The SPLASH surge model was tested with a preset value of 3×10^{-6} for the drag coefficient $C_D\ \rho_a/\rho_w$, with the coefficients of Eq. (20) set in the storm model and with no bottom stress. Results gave acceptable comparisons (within one foot) for the observed peak surges at Atlantic City during storm passages. However, the comparison with the free waves was unacceptable. Tests were then made with the addition of bottom stress and a no-slip condition. A value of 0.25 ft^2/s for the eddy viscosity, ν, gave an acceptable comparison with the free waves, with no significant change in the forced wave. Unfortunately, the amplitudes of the free waves were sensitive to small changes in ν. Finally, a value of 0.006 ft/s was set for the slip coefficient, s, and the computed free wave amplitudes were then insensitive to a broad range about $\nu = 0.25\ ft^2/s$. In fact, the peak surge of the forced wave, and the amplitude of free waves, were insensitive to a broad range of ν and s, when both were included in the bottom stress formulation (Jelesnianski, 1967). This may not always hold for shallow waters (<10 feet) or for slow moving storms. Special tests with the SLOSH model for shallow depths and inland inundation with real observed data in Lakes Okeechobee and Pontchartrain imply the adopted values of ν and s are acceptable in a universal sense, at least for the level of accuracy needed in operational storm surge forecasting.

Comparisons of surge data from a single tide gage for only three storms is barely adequate. The comparisons may be tainted by inaccurate storm parameters. Along the New Jersey coast, hurricanes are typically moving rapidly. Also, the position of the storm relative to the coast is difficult to determine. Thus, the derived coefficients for the unique, localized, surge dynamics generated by the storm may not hold for alternate regions with different storm tracks. More comparison tests are needed and have been partially done with the SPLASH model.

Surges generated by 43 historical, landfall storms on the Gulf and Atlantic coasts of the United States were used for comparisons (Jelesnianski, 1972). The surge data are measured high-water marks. These marks are not positioned uniformly along the coast, nor is the stilling action in buildings equal for each measured mark. The data contain wave set-up, but not generally the crest heights of breaking short gravity waves; e.g., the data is the still-water surge relevant to the stilling action inside structures, with complicated wave set-up according to distance from shore, and hence of

questionable accuracy. A value of 3×10^{-6} for the drag coefficient (multiplied by the ratio of air/water density) gave a standard error estimate of 1.6 feet with the observed marks (Jelesnianski, 1972). One can, of course, find an alternate C_D according to storm character and local geography.

By choice, the SPLASH equations of motion are linear. When the finite amplitude effect is included in the equations of motion, the computed surges are smaller whenever the offshore depths are very shallow and the surge amplitude is large. Test runs show these changes to have little effect statistically on the best fit C_D according to storm character and local geography.

When computing peak surges with the SPLASH and SLOSH models, the most sensitive coefficient is C_D. The computed surge is directly sensitive to the value of C_D, and for practical purposes varies linearly with C_D. There are many formulations for the drag coefficient, some very complicated; laboratory measurements are not in good agreement with natural measurements. Because of the great uncertainty of its value and variations, C_D is held constant at this time.

4. SURFACE STRESS AND SURFACE WINDS

A surge modeler is interested in surface stress and usually formulates it from surface winds. To this end, a modeler may anticipate an appropriate wind specification from meteorological forecasts. However, a meteorologist is interested in wind as an end product, not in surface stress per se. A "good" wind to the meteorologist may, in fact, be "bad" for modeling surface stress, and the other way around.

The surface stress, $\vec{\tau}$, is an important term in the equations of motion. It is as important as any aspect of a surge model, and the manner in which it is employed strongly affects computed surges. Generally, the wind stress per unit mass on the sea surface is formulated as,

$$\vec{\tau} = C_D \frac{\rho_a}{\rho_w} |\vec{W}| \vec{W} \qquad (21)$$

where C_D is the drag coefficient, ρ_w and ρ_a are densities of water and air, and W is the vector wind. Applying this formula to meteorological winds is not as simple as it looks. The stress term has coordinates

$$\vec{\tau} = \vec{\tau}(x,y,t), \quad \text{at } z = z_s,$$

where z_s is a specified height above the sea surface, usually 10 meters. On the other hand, wind from meteorological sources may have coordinates

$$\vec{W} = \vec{W}(x,y,t), \quad \text{on } p = p_o,$$

where p_o is a constant pressure surface. Such winds must be converted to the level z_s, or the drag coefficient in Eq. (21) must be varied in some complex fashion. Because surge models require massive amounts of surface stress data in space and time, it is useful to design a storm model dependent on simple meteorological parameters and to directly compute a wind vector at or near the z_s level.

The absolute value of stress is sensitive to errors in wind speed at a parabolic rate. Also, stress varies with the drag coefficient. But neither C_D nor $\vec{W}$ are known with consistent accuracy, and it would appear the art of surge computation is at a terrible disadvantage. However, a storm wind model can be designed so that surge computed with a surge model is only mildly sensitive to errors in $\vec{W}$. C_D can then be approximated empirically from historical storm surge data.

A water surface recognizes the converging wind field of a storm when the core passes by, and herein lies a physical property to reduce surge sensitivity to wind speed errors. A storm model can be designed with the following useful property: If the forces used to compute a wind field are in balance, then the computed surge under the core of a storm is not overly sensitive to consistent errors in the computed wind field, providing input storm parameters are accurate. This property exists if the model winds are in vector form such that a computed wind field of low wind speed is accompanied with a larger convergent wind field, whereas a computed wind field of large wind speed is accompanied with a smaller convergent wind field. In other words, a change of friction force in a storm model couples wind speed and direction in a biased manner. This property reduces surge sensitivity to wind speed.

The underlying surface greatly affects wind speed due to differing frictional effects. For a storm affecting a sea, an inland water body, or terrain, the winds are highest over the sea, less over inland water bodies, and least over terrain. The differences can be enormous. Winds over the center of the inland body of water can be higher than across its boundaries. Furthermore, at land/water boundaries, winds directed from water to land are stronger than from land to water, with strange distortions in the wind direction. There is an added complication when water inundates land or recedes--moving boundaries. Wind and stress are not merely functions of storm intensity, size, and motion, but also of local terrain, relative direction of the wind over shorelines, and the history of the wind and its past trajectory.

Let us consider changes in friction by using the SPLASH storm wind model (Jelesnianski and Taylor, 1973). This model is described in Section 4.c. First, assign values of central pressure, peripheral pressure, and storm size as input to the model. The computed profiles of wind speed, inflow angle, and pressure are shown in Fig. 2. The display is shown radially from the storm center. For ease of presentation, the profiles are plotted for a stationary, circularly-symmetric storm. The "Ocean" wind profiles are computed as functions of pressure and storm size by the SPLASH storm model on seas, using preassigned friction coefficients.

Suppose friction is arbitrarily increased to compute lower wind speeds called "Lake" winds. Then, to balance forces, the inflow angle must be significantly larger. The ratio of the absolute stress for the two wind fields is about 1.5, and

one might expect the surge computed with "Ocean" winds would be about 50% greater than with "Lake" winds. However, test computations with the SPLASH surge model gave only a 17% increase of the surge on the open coast when the three storm profiles were dynamically coupled. If only the wind speed profile is allowed to change without coupling the two remaining profiles, then there

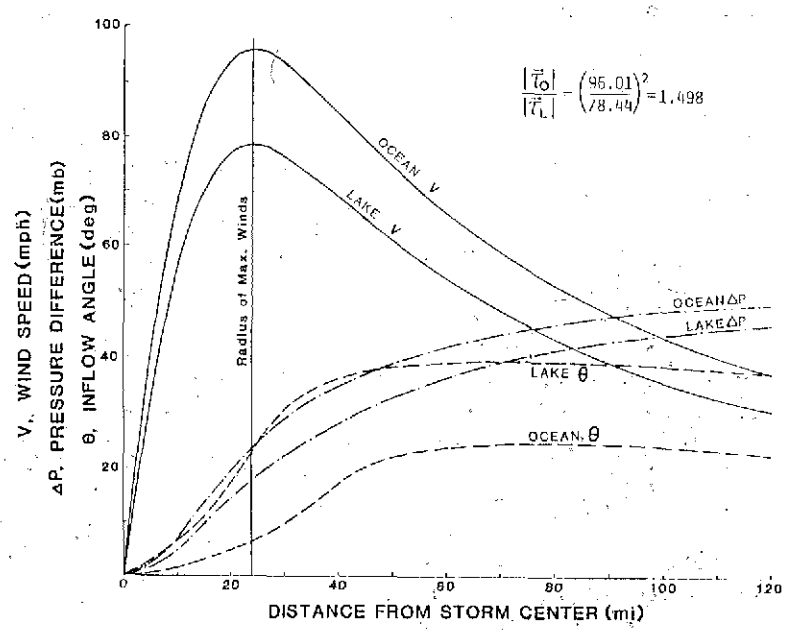

Figure 2. Comparing model profiles of wind speed, pressure difference, and inflow angle for a tropical storm over an ocean and across a lake. The profiles are for a stationary, circularly-symmetric storm.

is about a 50% change in the computed coastal surge. For combinations of coupled and uncoupled profiles, the surge changes between 17%-50%. The biased change in the convergence of the wind field due to changes in the inflow angle and pressure gradient reduce computed surge sensitivity with respect to wind errors. A wind model that balances forces needs only limited accuracy for the vector wind field. Hence, when computing surges with a storm model that has accurate storm parameters, the end product is not how well computed winds reproduce real winds, but rather how well computed surges reproduce real surges.

For an inland water body, it is not advisable to use "Ocean" type winds. The terrain surrounding the water body exerts extra friction, strongly decreasing the wind speed. The winds increase as they cross the inland water body, but rarely reach "Ocean" wind strength unless the water body is deep and has a much larger areal extent than the storm. In effect, wind has a memory of its past trajectory. The winds may be greatly lowered over an inland body of water due to its immediate past trajectory so that the larger inflow angle no longer compensates adequately in surge generation. Unlike a sea, an inland body is affected by only a part of a storm. The smaller a lake relative to storm size, the less able the lake is to recognize a convergent wind field and the less likely it is to experience "Ocean" winds. For a very small lake, the vector wind is nearly constant over the lake at any instant. For surge generation, the convergence of the wind field is negligible and no longer compensates for errors in the computed wind field. Even here, there is a trade off: the smaller a lake, the smaller a surge--if all other things are the same.

a. A Comparison of Observed and Computed "Lake" Winds

To get a feel and appreciation of "Lake" type winds, consider the 1949 storm which passed across Lake Okeechobee, Fig. 3. The wind speed and direction, observed by instruments on the lake, were extracted from Project Bulletin No. 2, (1950). They are subjective 10-minute averages extracted from anemometer traces. Input parameters for the storm model are as follows: hourly data for the central pressure were extracted from Hydrometeorological Report No. 26, (Weather Bureau, 1951) and a peripheral pressure of 1012 mb was used to form pressure drops. The input track of the storm followed the observed lowest central pressure. An invariant radius of maximum winds of 22 miles was used as the hurricane's size as it crossed the lake. The central pressure, storm size, and storm positions are accurate at the time of the storm passage across the lake. For the remainder of the track, a subjective analysis was made of scattered and peripheral data during storm passage across southern Florida.

To compute "Lake" winds with the input storm parameters, the friction coefficients of the SPLASH storm model were increased until the computed wind speed--for a moving storm--had a useful agreement with observed winds over two interior gaging stations LS 14 and LS 16, Fig. 3. Since gage elevations relative to the lake's surface did not differ greatly in time, no attempt was made to reduce winds to a constant level. The friction coefficients were four times greater than those normally used by the SPLASH storm model for "Ocean" winds. There is no guarantee the same friction coefficients would serve for different storms, different lakes, and different storm tracks. Lake bathymetry, local terrain features, distance from coastal regions of the sea, and shelf topography all interfere with wind generation in a most complex fashion.

The observed and computed winds are compared in Fig. 3. Model winds are initially computed with circular isobars and then altered with empirical corrections for storm motion and isobar distortion. The observed inland isobars were pear shaped with the greatest distortion away from storm center. There are periods when boundary positioned gages are exposed to dry land, and the winds are then "Terrain" type winds; these are ignored and the wind model computes "Lake" type winds. By "Lake" winds, we mean winds over an inland body of water, unaffected by terrain except for memory of its overland history; by "Ocean" winds we mean winds over the continental shelf, unaffected by terrain and without any memory of an overland history. Comparisons of "Lake" winds on lake boundaries are best for winds with an overwater trajectory, worst with an overland trajectory. It is assumed that winds seaward from a solid boundary have a strong wind speed gradient, localized to a narrow strip offshore.

For the following wind comparisons, HGS means "Hurricane Gage Station" and LS means "Lake Station":

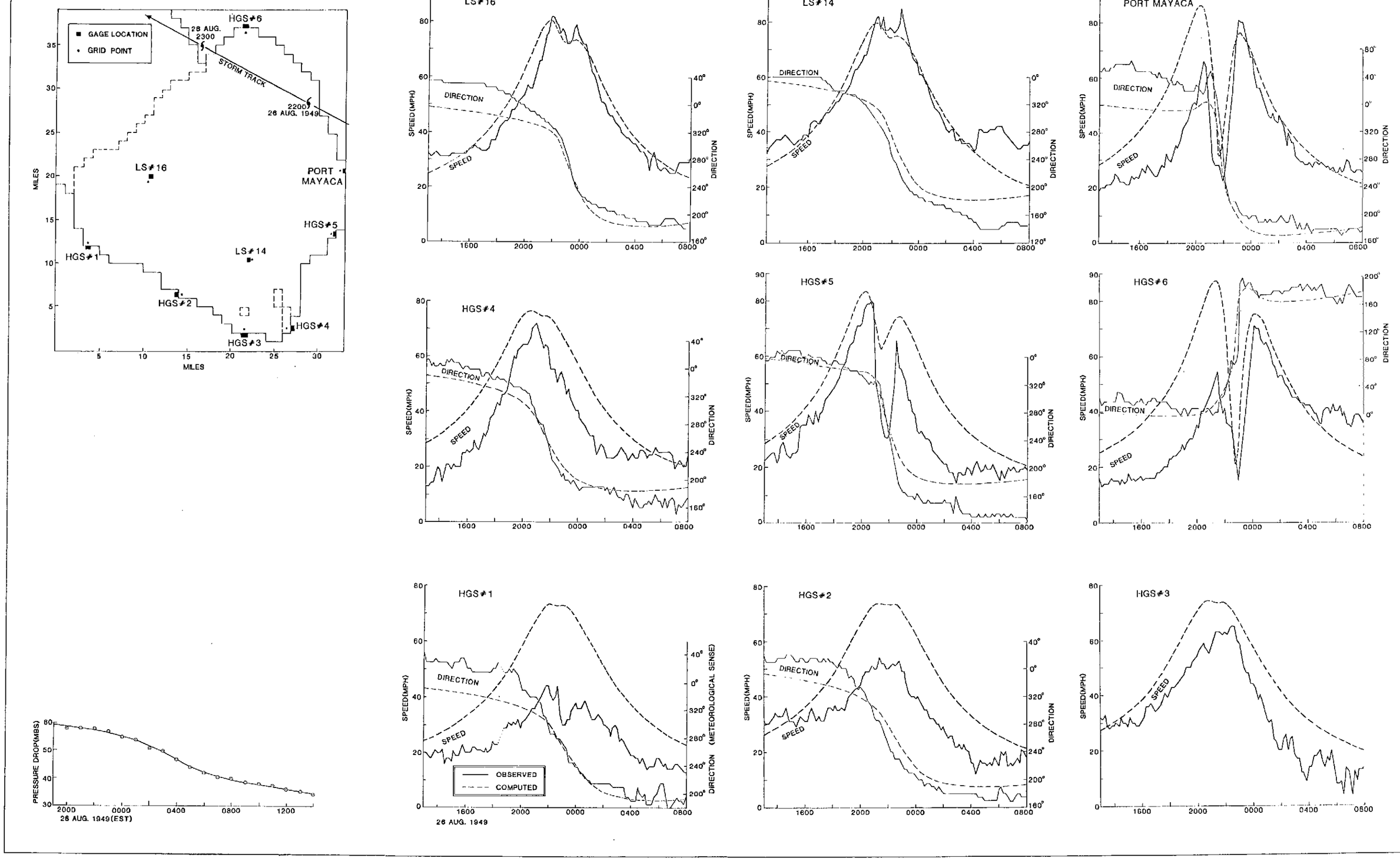

Figure 3. Observed and computed winds for the 1949 hurricane over Lake Okeechobee, Florida. The station locations and the hurricane's track over the lake are given in the insert at the upper left. The pressure as a function of time is shown in the lower left. Observed wind speeds and directions are shown with solidlines; computed values are shown as dashed lines.

LS 14 and LS 16: These two gages lie on the interior of the lake. The trajectory of the wind is overwater, for all time. The computed winds agree with observations. The surrounding terrain to the west of LS 16 is marsh land with little water elevation above terrain for all time.

HGS 1: Before, during, and after storm passage there was no significant overwater trajectory of the wind field, except well before storm passage. The surrounding terrain is marshy and generally exposed, with at most one foot of water above terrain. The observed "Terrain" type winds are much smaller than computed "Lake" winds, except well before storm passage.

HGS 2, 3, and 4: During and after storm passage, there was no significant overwater trajectory field. Before storm passage, the winds were nearly parallel to the boundaries, and well before storm arrival there was an overwater trajectory except at HGS 4. After storm passage, the local terrain was exposed or under very little water. The winds are generally smaller than computed, except well before storm arrival.

HGS 5 and PORT MAYAGA: These two gages are close to each other but with different lake boundary orientations. Comparison of these two gages powerfully illustrates the effects of trajectory of the wind field as follows:

1. Before storm arrival,

   a. HGS 5 winds have an overwater trajectory and computed winds agree.

   b. PORT MAYACA winds have an overland trajectory and winds do not agree.

2. After storm arrival,

   a. HGS 5 winds have an overland trajectory and computed winds do not agree.

   b. PORT MAYACA winds have an overwater trajectory and computed winds agree.

HGS 6: This was the only operating gage north of (i.e., to the right of) the storm track. Before storm passage, the winds were from the north with an overland trajectory and computed winds do not agree. After storm passage, the winds were from the south with an overwater trajectory and the winds agree.

Observed wind speeds far from the storm center are generally greater than computed speeds. There are two possible causes of this discrepancy: 1) in these regions, the storm model may be inappropriate, or 2) the input storm parameters are improperly set before and after storm passage on the lake. Improperly computed peripheral winds have little affect on maximum surge generation near a storm's core. Of course, if a storm's core traverses far from a basin and peripheral winds affect the basin, then computed surges, although small, may be in error.

Real winds have strong gradients at water boundaries. It is assumed the gradient is localized to the near shore region with rapid readjustment to "Lake" or "Ocean" winds a short distance offshore. The localized wind gradient is assumed narrow enough not to significantly affect the overall surge. The biased inflow angle with computed winds partially compensates for wind errors that do not recognize a narrow, localized wind gradient.

Empirical tests with the SLOSH model show the computed surge is insensitive to exact demarcation between "Ocean" and "Lake" winds. This is a useful property since the positioning of "Ocean" and "Lake" winds is subjective.

The inland isobars of the 1949 storm were distorted and non-circular. The computed "Lake" winds are crudely corrected for distorted isobars by assuming the distortion axis lies along storm path. The real axis of distortion, however, was significantly removed from storm path.

b. Surface Drag Coefficient

A constant, empirical value of 3×10^{-6} is assigned to $C_D \rho_a / \rho_w$ in Eq. (21). This number was derived by comparing observed high-water marks along the coast to computed surge for 43 historical storms. The SPLASH surge model with "Ocean" winds (Jelesnianski, 1972), was used to compute the coastal surges. The number is a gross approximation in a best fit sense. "Good" surge comparisons did not occur for all 43 storm events. One could align data according to storm parameters, storm track, basin geometry, etc., and then vary the drag coefficient statistically as a function of data parameters. However, this was not attempted because of the limited sample of storm and surge data. The empirical value of C_D has proven useful in field trials to forecast coastal surges in real time, with actual storm situations. The SPLASH surge model uses linearized equations of motion, and the derived drag coefficient does not necessarily apply to non-linear models. However, if the finite amplitude effect is included in the SPLASH model, there is little overall change in surges on the continental shelf except in very shallow waters or for extreme surge heights. The SLOSH model of this report considers finite amplitude effects, and an alternate drag coefficient may be desirable. However, results with real data for the basins of this study are acceptably accurate for operational forecasting.

Our procedure for SLOSH uses a drag coefficient identical to that of SPLASH. Results indicate no major readjustment of the drag coefficient is required.

c. The SPLASH and SLOSH Storm Models

Let us begin by examining the wind model used in SLOSH, which is among the most important features of the model. This wind model evolved from the SPLASH storm model (Jelesnianski and Taylor, 1973) which computes pressure and wind direction for a stationary, circularly-symmetric storm.

The computations are based on a balance of forces given by

$$\frac{1}{\rho_a}\frac{dp}{dr} = \frac{k_s V^2}{\sin\Phi} - V\frac{dV}{dr} \qquad (22)$$

$$\frac{1}{\rho_a}\frac{dp}{dr}\cos\Phi = fV + \frac{V^2}{r}\cos\Phi - V^2\frac{d\Phi}{dr}\sin\Phi + k_n V^2 \qquad (23)$$

These equations are adapted from Myers and Malkin (1961). Here, r is the distance from the storm center, p(r) is the pressure, $\Phi(r)$ the inflow angle across circular isobars toward the storm center, and V(r) is the wind speed. The terms k_s and k_n are empirically determined coefficients, and f is the Coriolis parameter. The two equations can be solved for p and Φ, on a ray from the storm center, if the form of the wind speed profile V(r) is supplied. One benefit of this procedure is that the maximum wind falls exactly at r = R. The SPLASH storm model uses the following wind speed profile for a stationary storm:

$$V(r) = V_R\frac{2Rr}{R^2 + r^2} \qquad (24)$$

The parameter R is the radius of maximum wind (the distance from storm center to the maximum wind), and V_R is the maximum wind speed.

Figure 2 shows an example of profiles computed by Eqs. (22-24). For real applications, the maximum wind, V_R, for a stationary storm is not readily available on a sea's surface. For a moving storm, the central and peripheral pressure, and storm size, R, are likely to be available. To solve these equations, an iteration procedure is used. V_R is approximated (using a table look-up procedure from pre-computations) and Eqs. (22-24) are then solved for p(r) and $\Phi(r)$. The discrepancy between computed and required pressure is then obviated by changing V_R until the pressure discrepancy is less than a preassigned value.

In polar coordinates (r,θ), the vector wind for the stationary storm is

$$\vec{V} = V_R\frac{2Rr}{R^2 + r^2}\, e^{i[\pi/2+\theta+\Phi(r)]} \qquad (25)$$

Consider storm motion such that the track of the storm is relative north and $\theta = 0$ is relative east. Then a vector correction for storm motion is empirically formulated as

$$\vec{V}_1 = |\vec{U}_S|\frac{Rr}{R^2 + r^2}\, e^{i\pi/2} \qquad (26)$$

where $|\vec{U}_S|$ is the speed of the storm. The maximum value of the storm correction is $\frac{1}{2}|\vec{U}_S|$ at r = R. Correction values taper off to zero at r = 0 and $r = \infty$. This correction could be faulty for a weak storm moving rapidly, but such storms create little surge. Empirical tests with the SPLASH surge model show coastal surges are not overly sensitive to the correction vector, $\vec{V}_1$, for moderate to extreme intensity storms.

The wind for a moving storm superposes Eqs. (25) and (26) as

$$\vec{W}_0 = \vec{V} + \vec{V}_1 \qquad (27)$$

For a given r, winds are maximum at $\theta = -\Phi(r)$. Hence, maximum winds occur in the right rear quadrant if $\vec{V}_1$ is used for storm motion correction. $\vec{W}_0$ is used for "Ocean" winds; the friction coefficients k_s and k_n must be supplied, and they are chosen as functions of storm parameters, Eq. (20), (Jelesnianski, 1967). Since position of a storm is known as a function of time, with $\vec{V}$ computed with respect to "r", and with $\vec{U}_S$ given, it is then easy (albeit laborious) to compute $\vec{W}_0$ and hence wind stress at each grid point located at "r" from storm center.

A storm moving across open terrain or over lakes has pressure isobars distorted due, in part, to increased friction. The additional friction, of course, modifies $\vec{V}$. The axis of distortion follows no precise orientation, but can lay in the vicinity of storm track. Such pressure distortion increases winds before storm arrival and lowers them after storm passage. One can partially correct the winds for pressure distortion by appending a linear pressure gradient perpendicular to the distortion axis and computing an additional geostrophic wind from the added pressure gradient. However, geostrophic wind is sensitive to the distorted pressure gradient. A gradient of 1 mb/100 miles, at latitude 30°, gives a 15 mph wind. There is no precise way to forecast the pressure distortion for individual storms. The pressure field is further complicated if the storm is imbedded in a synoptic scale pressure field.

The SLOSH model uses the SPLASH storm model. For inland water bodies, stronger friction is used, and an additional correction for pressure distortion is included. The higher friction and additional correction are applied only to inland water surfaces and not to continental shelves. The additional correction is

$$\vec{V}_2 = |\vec{U}_S|\frac{R|Y|}{R^2+Y^2}\, e^{i7\pi/6} \qquad (28)$$

where Y is the normal component of r along the track direction. The additional correction is a directed wind, perpendicular to the track, plus a 30° backing for friction effects. We control the correction by means of storm speed instead of actual pressure distortion. Distortion is directly related to storm speed. For a stationary storm, we assume no pressure distortion and the wind is then $\vec{V}$.

The "Lake" wind then is a superposition of two corrections to the stationary storm as

$$\vec{W}_L = \vec{V} + \vec{V}_1 + \vec{V}_2 \qquad (29)$$

The additional correction $\vec{V}_2$ is qualitative in nature. The maximum value is $\vec{U}_S$ along two lines perpendicular to storm track at $\pm R$ from storm center. Values taper off to zero at Y = 0 and $Y = \pm\infty$. The maximum winds now occur in the right-front quadrant. Empirical tests show only minor changes in overland and lake surges if $\vec{V}_2$ is omitted. The nature of the change corrects wind and surge qualitatively and therefore is used for its cosmetic effect.

For operational convenience, "Lake" winds are used across inundated terrain even though

vegetative material over terrain is considerably different from the beds of bays and lakes. An extinction coefficient (based on vegetation height) is used on the stress terms across dense foliage such as mangroves and forests. In reality, the friction terms k_s and k_n should be higher over inundated terrain and vary according to type of terrain; e.g., the heavily concentrated mangroves over part of the Florida Everglades. There are not enough observed data during storm surge flooding of densely foliated terrain to empirically ascertain friction values for the wind profile. Accordingly, computed surge values may be suspect over densely foliated terrain.

5. THE GRID SCHEME AND EXPLICIT, FINITE DIFFERENCE SCHEME

The fields, surge and transport of Eq. (1), or surge and transformed transport of Eq. (13), are separately computed at discrete, equally-spaced points on a horizontal grid mesh. The grid scheme treats a surface of surges in a two-dimensional, stair-step fashion. A template of the grid scheme is shown in Fig. 4. The grid is used with Cartesian or transformed coordinates. For illustration, the Cartesian form for equations of motion (1) is discussed. (The transformed form is equivalent but uses a different notation.) A '+' point is the center of a square; a '$_\circ$' point lies on each corner of a square. Surge is computed on the '+' points and transport on the '$_\circ$' points. Both components of transport are computed at each '$_\circ$' point. Predetermined fields, such as depths relative to a horizontal datum, meteorological driving forces, etc., are appropriately positioned on grid points as needed.

The grid scheme of Fig. 4 is labeled 'B' by Mesinger and Arakawa (1976), who also discuss an alternate scheme, 'C'. For some purposes, scheme 'C' is preferred. However, we chose to use scheme 'B' instead to better accommodate the Coriolis terms, to treat cases of shallow water depths, and to allow computations of both components of surge gradient at '$_\circ$' points.

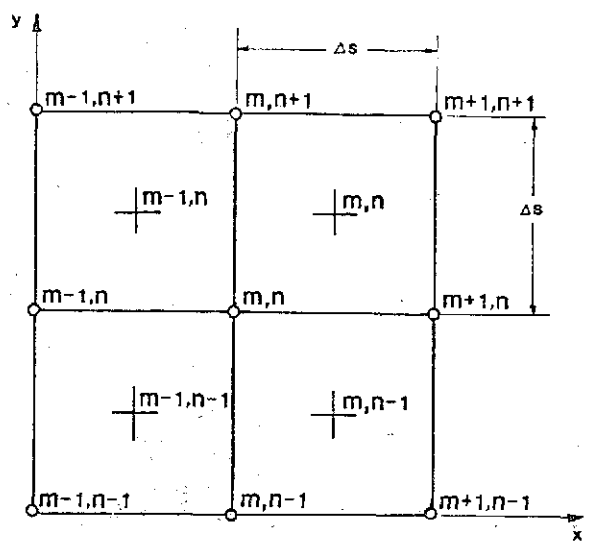

Figure 4. A grid template for the finite difference scheme used in the SLOSH model. The '+' points are surge or height points on the grid, located at the center of squares. The '$_\circ$' points are momentum points on the grid, located at the corner points of squares.

Relative to a transport point, a surge point is offset by a distance $1/2\Delta s$ in the x- and y- directions A template with two separate labeling schemes, for surge and transport points, could be represented as shown on Fig. 4. There are other, more-compact, labeling schemes (Mesinger and Arakawa, 1976), that are more elegant for theoretical work. The separate labeling for height and transport fields in this report is convenient for computer use.

Any field value, $F(x,y,t)$, can be labeled at a grid point as $F^k_{m,n} = F(m\,\Delta s, n\,\Delta s, k\,\Delta t)$, where m and n are integer grid positions and k is an integer to represent the number of discrete time intervals Δt. For finite difference computations, a given field value is labeled either on a surge or transport point, as required.

For continuous changes in time, the time derivative can be approximated for three* levels in time--past, present and future--as,

$$\frac{\partial F}{\partial t} = \frac{1}{2\Delta t}\,(F^{k+1}_{m,n} - F^{k-1}_{m,n}) \quad . \tag{30}$$

In numerical computations, the spatial surge derivative is computed at transport points, and spatial transport derivatives are computed at surge points. A spatial surge derivative at an (m,n) transport '$_\circ$' point is approximated as

$$\frac{\partial h}{\partial x} = \frac{1}{2\Delta s}\,[h^k_{m,n} - h^k_{m-1,n} + h^k_{m,n-1} - h^k_{m-1,n-1}], \tag{31}$$

$$\frac{\partial h}{\partial y} = \frac{1}{2\Delta s}\,[h^k_{m,n} + h^k_{m-1,n} - h^k_{m,n-1} - h^k_{m-1,n-1}],$$

m,n subscripts at '+' points

A spatial transport derivative at an (m,n) surge '+' point can be approximated as

$$\frac{\partial U}{\partial x} = \frac{1}{2\Delta s}\,[U^k_{m+1,n+1} - U^k_{m,n+1} + U^k_{m+1,n} - U^k_{m,n}], \tag{32}$$

$$\frac{\partial V}{\partial y} = \frac{1}{2\Delta s}\,[V^k_{m+1,n+1} + V^k_{m,n+1} - V^k_{m+1,n} - V^k_{m,n}],$$

m,n subscripts at '$_\circ$' point

*Two levels in time can be used, with savings in computational time and computer memory. Empirical tests show minor changes in computed peak surges and small changes in inland inundation.

The spatial derivatives (31) and (32), when acting on a surge or transport field, are now defined as $D(\ )^k/2\ \Delta s$; the symbol $(\ )^k$ stands for U^k, V^k, h^k or h^k_o. In finite difference form, we then rewrite Eq. (1) as

$$U^{k+1}_{m,n} = (1+a\bar{A}_i)U^{k-1}_{m,n} - b\bar{H}^k_{m,n}[B_rD_x - B_iD_y]h^k + aA_rV^k_{m,n} + c\ {}^xT^k_{m,n}$$

$$V^{k+1}_{m,n} = (1+a\bar{A}_i)V^{k-1}_{m,n} - b\bar{H}^k_{m,n}[B_rD_y + B_iD_x]h^k - aA_rU^k_{m,n} + c\ {}^yT^k_{m,n} \qquad (33)$$

where $a = 2f\,\Delta t$, $b = g\,\Delta t/\Delta s$, $c = 2\,\Delta t$ and components of 'T' are given by (13 a). $\bar{H}^k_{m,n}$ <u>at a transport '$_o$' point</u> is the arithmetic mean of total depth values on four surrounding surge '+' points, e.g.,

$$\bar{H}^k_{m,n} = \frac{1}{4}[(D+h)^k_{m,n} + (D+h)^k_{m-1,n} + (D+h)^k_{m,n-1} + (D+h)^k_{m-1,n-1}]. \qquad (34)$$

Depths, $D_{m,n}$, not to be confused with derivatives with respect to a datum, are fixed at surge '+' points. If a barrier is not overtopped by all four surrounding squares at a momentum point, special techniques are used which are described in a later section. The friction coefficients $A_r, A_i, B_r, B_i, C_i, C_r$ are functions of H at a transport point '$_o$'. These coefficients show only very small variations for depth changes in shallow or deep water. However, the friction term, A, varies strongly in very shallow waters with small changes in depth. Hence, the arithmetic mean of A_i on the four squares is used. The surface stress ${}^xT^k_{m,n}$, ${}^yT^k_{m,n}$ are computed at transport '$_o$' points.

The water surface of the SLOSH model, and bed of the model basin, are approximated as two-dimensional stair steps. Figure 5 shows an example of stair steps that are dry or wetted. If water initially enters a dry square, or exhausts a wet square, specialized computational techniques are implemented. A wetted square has a volume of water with plane surface 'abcd' $= (\Delta s)^2$ and total depth 'H'. The space gradient on the water surface is the height difference between squares measured from a common datum. A corner of a wetted square cannot have two-dimensional flow if a stair-step-rise or barrier is not overtopped. Two-dimensional flow exists at points 'a' and 'b', but not at points 'c' and 'd' unless a contiguous square(s) surrounding these points overtops the barrier height. In the absence of a barrier, two-dimensional flow exists at a momentum point only if at least one of the four surrounding squares is wetted and higher than the highest bed depth of the four surrounding squares.

Barriers specified within the model can run only along the sides of a square, can turn 90° at a corner point, and must terminate at a corner point. Separate barriers can cross at a corner point. The height of a barrier at a corner point is the mean height along its length Δs; that is,

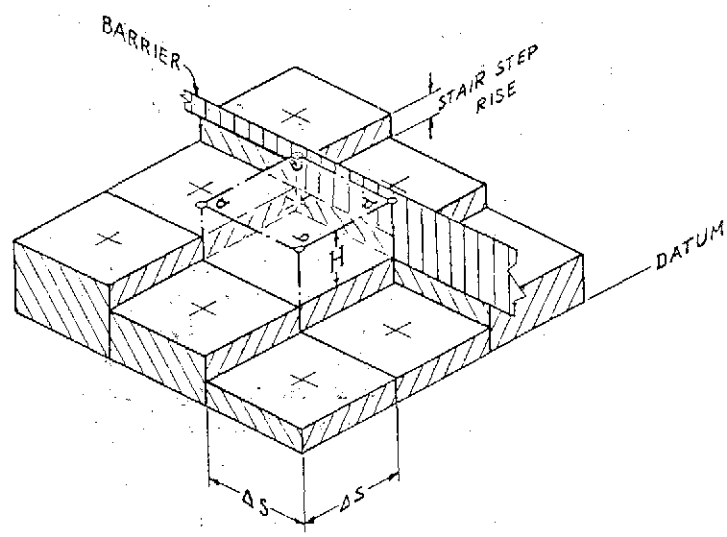

+ = SURGE POINT
⊙ = TRANSPORT POINT
H = WATER DEPTH ABOVE A SQUARE
a,b,c,d = WATER SURFACE ABOVE A SQUARE

Figure 5. Dry and wetted grid squares. The squares form two-dimensional stair steps.

1/2 Δs on both sides of a corner point, except at the termination of a barrier at a corner point. For a barrier to exist, it must be higher than the highest square at a corner point. Gaps through barriers, are treated separately as special cases.

When barriers or stair-step rises are not overtopped, horizontal (as opposed to bottom) slip or no-slip conditions must be chosen along barriers for finite difference computations. The SLOSH model, at this time, uses no-slip along unovertopped barriers. For the differential equations (1), no-slip is an overspecification unless horizontal viscosity is included. The SLOSH equations, of course, can accommodate horizontal viscosity, but empirical computations with and without horizontal viscosity give only minor changes in the surge computations. The no-slip condition along barriers is not necessarily an overspecification with (33) because of the additional computational solutions compared to solutions of the differential equations (1). Other grid schemes implicitly assume a slip condition along a barrier, although transport itself may not be computed along barriers.

In the case of the <u>initial</u> flooding of a surge square (continuity equation), or the <u>initial</u> flow across a transport point (momentum equation), two levels in time are used--present and future--as,

$$h^{k+1}_{m,n} = h^k_{m,n} - \frac{b}{2g}[D_xU^k + D_yV^k]$$

$$U^{k+1}_{m,n} = (1+\frac{a}{2}\bar{A}_i)U^k_{m,n} - \frac{b}{2}\bar{H}^{k+1}_{m,n}[B_rD_x - B_iD_y]h^{k+1} + \frac{a}{2}A_rV^k_{m,n}$$

$$V^{k+1}_{m,n} = (1+\frac{a}{2}\bar{A}_i)V^k_{m,n} - \frac{b}{2}\bar{H}^{k+1}_{m,n}[B_rD_y + B_iD_x]h^{k+1} - \frac{a}{2}A_rU^k_{m,n} \qquad (35)$$

where special techniques are used to form H and the friction term A_i. The momentum equations are driven by gravity forces, and surface driving forces are ignored.

The equations of motion (33) or (35) are designed for two-dimensional flow; they are not designed to handle one-dimensional or channel flow. Equations (33) were designed for flow in the interior of a region where total depth, $H = (D+h)^k_{m,n}$ is positive; i.e., with wetted squares.

Equations (35) were designed for flow inundating onto dry squares. Considerable difficulty arises with inland inundation and the resulting moving fluid boundaries. It is not always possible to satisfy the three equations of motion, Eqs.(33) or (35). The momentum equations do not have adequate sophistication to reconstruct flow in thin sheets of water over corrugated terrain with vegetative and other surface features. In such cases, the continuity equation and simple storage principles take precedence over the transport momentum equations.

a. Computations with Continuity Equation at a '+' Point

When using the continuity equation of (33) or (35), the following are some of the techniques used to compute surge values at future time at a '+' point, Fig. 4.

1. At present 'k' time, if all four surrounding corners of a grid square (four transport '$_\circ$' points) have no flow, then computations are ignored at the '+' point, and no water enters or exists the square. This holds even if the square is wet; e.g., if the square is a local low point in natural terrain and surrounding squares are dry, or if water from surrounding wet squares is held back by barriers.

2. At the present time, if at least one of the four surrounding corners has flow and the square is wet, then the continuity equation of (33) is used. But if the square is dry, then the continuity equation of (35) is used. Here, we discriminate between cases of unimpeded flow into a wet square, initial inundation into a dry square, and flow into a wetted square partially bordered with barriers or stair-step rises not overtopped. We do not discriminate for the very special case of an isolated wet square at a local low point in natural terrain initially suffering inland inundation; that is, Eq. (33) is used even though Eq. (35) may be preferable for this case. Empirical tests show this special case is not significant in surge generation.

3. If computation at a '+' point results in water below the square, then the square is set dry at future time. Water is not permitted to fall beneath a dry square. In order to conserve mass, the transport at present time on the four corners are decreased by a fixed ratio so as to exhaust all water in the square and no more. Surge values at contiguous squares surrounding the four corners are computed (or recomputed) with the decreased transport values at the four corner points. Here, we rely on the continuity equation and storage principles. Usually, in this special case involving a thin sheet of water, the surface and bottom stresses are inadequate in the equations of motion, or Δt is too large between computational time steps. The momentum equations are no longer completely relied on.

Note that when two levels in time (rather than three levels) are used, appropriate techniques differing slightly from these are used.

b. Computations with Momentum Equations at a '$_\circ$' Point

In the SLOSH model, the momentum equations are applied after the continuity equation computes surges at future time for the entire basin. In some special flow cases, the momentum equations are partially modified. Computing with momentum equations is not as clear cut as with the continuity equation. Much testing is required before using the momentum equation to determine if flow is impeded by a barrier or stair-step-rise, Fig. 6. Also, flow initially inundating a square--that is, water on a square at future time but not present time--is considered.

For reference purposes, a transport point in the interior of a basin, Fig. 6, is always surrounded by four squares. These squares may all be wet, all dry, or may be a combination of wet and dry squares. As a definition, water will 'overtop' a transport point when the surface of at least one wetted square lies above the highest of the four dry squares, Fig. 6b, or if a barrier is present, above the barrier, Fig. 6d. The following are some of the techniques used to compute transport with the momentum equations of (33) or (35).

1. If all four squares are dry at future time, Fig. 6a, transport is set to zero at future time. This is done even if some or all squares are wet and overtopped at present time.

2. If all four squares are wet at both future and present time, and all overtop, Fig. 6b, then Eq. (33) is used. If the bed of the highest square (or barrier) is above -40 feet--i.e., approaching shallow depths--then the friction term, A_i, is set as the arithmetic mean of A_i on four squares, where A_i is a function of the total depth 'H' above bed level of a square. If the depth is below -40 feet, then A_i is a function of the depth 'H' Eq. (34). In shallow waters, the A_i term is the most sensitive of the bottom stress terms.

3. If all four squares are wet at future time but dry at present time, and if all squares overtop at future time, Fig. 6b, then Eq. (35) is used.

4. If some or all squares are wet at future time but none overtop, then transport is set to zero at future time. This is done even if squares are wet and overtop at present time.

5. If one, two or three (but not all four) wetted squares overtop at future time but all four squares overtop at present time, then Eq. (33) is used with driving forces set to zero.

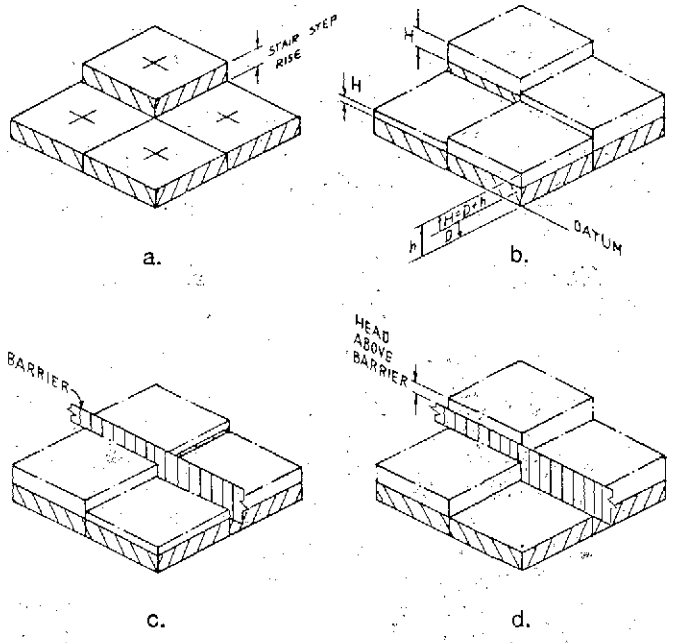

Figure 6. Idealized combinations of dry and wetted squares, with and without barriers.

6. If all four squares are wet and overtop at future time but fewer squares are wet and overtop at present time, then Eq. (33) is used with modifications. The A_i term, and Eq. (31), are altered as follows:

   a. The height of a dry square (or wet square that does not overtop) is set to barrier height, or in the absence of a barrier, set to the height of the highest square, in gradient equation (31). In this way, flow depends on the head of water above the barrier or highest square. That is, the surge gradient is measured by the head of water above the barrier or highest square, Fig. 6d.

   b. To derive the A_i friction term at the present time, a special empirical value for a dry square is used. Since the A term is stored at incremental foot levels, its value for a dry square is given by linearly extrapolating to zero depth with given values at 1 and 2 feet.

7. If one, two, or three wetted squares overtop at future time, and if one, two, or three squares overtop at present time, then Eq. (33) is still used with the above modifications at present time. Testing is not performed if the same squares overtop at both the present and future time. (There is much room here and in item 5 for improvement with complicated applications for separate squares in present and future time.)

8. If only one, two, or three wetted squares overtop at future time, but no squares overtop at present time, then Eq. (35) is used but with the modifications of item 6, applied at future time.

Again, when two, rather than three, levels in time are used, then appropriate techniques differing slightly from those above are used.

The action of wind through surface stress on a thin sheet of water is a complicated process and cannot adequately be described by the present momentum equations. To partially ameliorate the inadequacy on thin sheets of water, an arbitrary extinction coefficient is applied to the surface wind stress. The wind stress at a transport point is reduced whenever the total water depth in a square, H = D+h, is less than 1 foot. For general wet terrain with no trees or mangroves and with no barriers, Fig. 6b, the following rule is applicable:

$$\begin{aligned} &\text{extinction coefficient} = H, \quad 0 \le H \le 1 \\ &\text{extinction coefficient} = 1, \quad H > 1, \end{aligned} \tag{36}$$

and the final extinction coefficient is set as the arithmetic mean on four squares. This linear choice for the extinction coefficient with a small range of 1 foot is arbitrary. It has been tested with only a limited amount of observed inland surge data. Tests with the SLOSH model show the peak surge at interior squares of an inundated region is insensitive to Eq. (36) if the range of 1 foot is changed. The position of a moving boundary with time--say on a large and nearly horizontal plateau--can be sensitive to the range. However, with stair-step-rises and/or barriers, the boundary position and peak surges are not sensitive to the range. The extinction coefficient can delay the onset of inundation. In general, the total inundation is not sensitive.

In the SLOSH model, Eq. (36) is modified to account for barriers and stair-step-rises. In such situations the water depth, H, in each square is measured from the barrier height or highest rise. Thus, the extinction coefficient on each square is unity only when water is greater than one foot above a barrier or the highest of the four squares surrounding a momentum point. Each square is given a weight of 0.25. Thus, if only one square overtops by 0.5 feet, the coefficient is 0.125, etc.

There are localized, low-lying, terrain regions with dense vegetation such as the mangroves along the southern coasts of Florida, dense forests inside swamps, etc. In these regions, the stress across thin sheets of inundating or receding water is significantly reduced compared to open terrain. In these heavily vegetated regions, the available observational surge data are too sparse or non-existent to adequately formulate empirical standards to extinguish wind stress. For a convenient working criteria, the SLOSH model alters the extinction coefficient of Eq. (36) from a height of 1 foot to half the average height of vegetative material. The computed surges in these areas are not sensitive to the exact height, up to a factor of about 2. For dense mangroves, a height of 10 feet is presently used. The effect of this stronger extinction coefficient is to reduce the peak surge locally by about 10% compared to Eq. (36). A compensating effect is to increase slightly the surge along the coast where mangroves begin.

Land contours on most topographic charts are at 5-foot intervals above NGVD (National Geodetic Vertical Datum). Marine charts give spot depth readings to the nearest foot below MLW (Mean Low Water). Both charts give only limited information on vegetation. If it is assumed vegetation impedes flow over terrain more than over water, then some account of vegetation is desirable. Instead of altering friction coefficients over terrain, the SLOSH model merely adjusts the effective water depth, H=D+h, over terrain as follows:

$$\text{total depth} = H-1+(1-H/5)^3 \quad \text{, for } 0\leq H\leq 5 \qquad (36a)$$
$$\text{total depth} = H-1 \quad \text{, for } H\geq 5.$$

The depth reduction is applied only if all four squares surrounding a momentum point are over terrain, wet and overtopped. The break of 5 feet is arbitrary*. The revised H's are used in Eq. (34); the surface gradients (31) are not altered. The empirical depth adjustment changes friction values only slightly, except at very small depths and then only for the A_i term. Whenever terrain slopes or barrier impediments abound, the total inundation is not sensitive to Eq. (36a), nor to its range. However, the inundation process is slowed across flat terrain without barriers. In general, Eq. (36a) is most significant for small storms moving fast, least significant for large storms moving slow. This implies that the total inundation depends on the residence time of the storm across terrain.

The procedures for flow over terrain is empirical, coarse and open to objections. Model tests, with and without depth adjustments over terrain, show small changes for the total inundation in the basins studied so far. Its use qualitatively impedes initial flow over terrain, but is more cosmetic than substantial.

The present SLOSH model does produce two-grid-wave noise due to boundary effects, turning on and off mature driving forces during inundation and recession, under- and overtopping barriers, and an imprecise demarcation between "Lake" and "Ocean" winds. The two-grid wave has not been investigated satisfactorily under conditions of a variable sea surface, variable bathymetry, and moving boundaries. To partially eliminate this noise, a smoothing procedure is used at hourly intervals**. All output is smoothed in space to partially eliminate the two-grid-wave noise, Appendix C.

6. ONE-DIMENSIONAL FLOW

If terrain is irregular, the two-dimensional flow equations are sometimes inadequate during initial flooding or abatement. Figure 7 is one example. We note the bed of square "abcd" has the following special property: each of the four corners of the square has a maximum stair height, but the bed is lower than the lowest of the four maximum stair heights. Such a square is an "isolated square." If neither of two adjacent corners of a side are overtopped, then the horizontal no-slip condition prevents water from entering or exiting, that is, the water cannot flow through side "ab" according to the present grid scheme of the SLOSH model. Such an obstruction is unnatural. There are many alternative configurations of isolated squares according to relative positions of barriers and stair steps. Isolated squares occur along terrain irregularities such as depressions, barriers and corrugations on natural terrain. Fortunately, these may be few in number since most squares have at least one unobstructed corner.

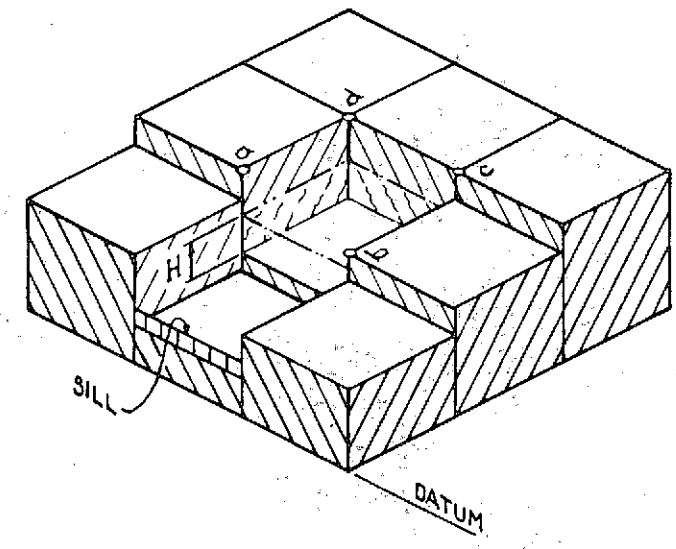

Figure 7. A wetted, isolated square, 'abcd', with only one unobstructed side for water passage. A 'sill' can be present along a side of a square.

Another example of suppressed two-dimensional flow is a "gap" or cut in a barrier, Fig. 8. The gap length can be smaller than the side of a square. An "unobstructed" side of a square is a special kind of gap. For a side to be unobstructed, a pathway must exist for water to pass through. An isolated square can have up to four unobstructed sides. A connection of several isolated squares, with an unobstructed side between two adjacent squares, can form a channel* such as a river basin.

A special situation is a "sill" rising from the bottom of an unobstructed side, Fig. 7. Water in a square must overtop a "sill" before a head can form to pass water through the unobstructed side.

The special case of flow through a narrow (subgrid size), deep channel connecting two water bodies will be discussed later.

The location and character of all isolated squares, unobstructed sides, sills, and gaps along barriers are predetermined as input basin data into the SLOSH program. Also, gap lengths and sill heights must be specified. If two-dimensional flow is suppressed, then an unobstructed side or gap is tested for activation of one-dimensional flow. Empirical tests with the

---

*Tests are underway for different formulations over forests and mangroves with a larger slip coefficient.

**Tests are underway for more selective smoothing about unovertopped corner points and barriers.

*Transitions can exist in the channel, that is, expansions or contractions. They are treated separately. Also, bank heights along rivers are under development.

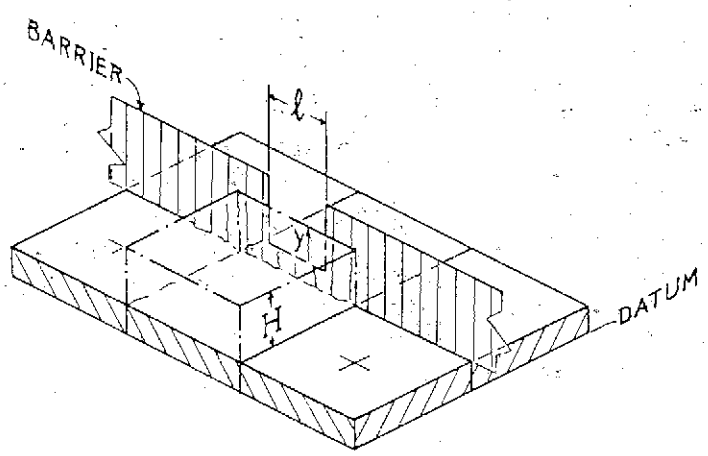

Figure 8. A 'gap' of length 'l' along a barrier. The head of water 'Y' drives water across the gap.

SLOSH model point out that peak surges are not sensitive to localized, one dimensional flow of short duration. However, low surges and the position of a moving boundary during inundation or exhaustion do have sensitivity; one example is the astronomical tide. However, a note of caution is needed here. Good results with astronomical tide computations do not necessarily imply good results for storm computations. Astronomical tide is driven by gravity alone; storm surges result mainly from meteorological driving forces.

When simulating terrain with stair-step squares, the abrupt rises on sides of squares are generally fictitious. Exceptions are shoreline bluffs, sills, ridge lines, and man made barriers. One-dimensional flow through unobstructed sides of a square is a useful mechanism to initially store or exhaust water over irregular terrain.

The one-dimensional flow equations used by the SLOSH model are a revision of the Cartesian two-dimensional flow equation, Eq. (1). If V = 0 for one-dimensional flow, then

$$\frac{\partial U}{\partial t} = -g(D+h)\left(B_r + \frac{B_i^2}{B_r}\right)\frac{\partial h}{\partial x} + f\left(A_i - A_r\frac{B_i}{B_r}\right)U + \frac{B_i}{B_r}y_T + x_T$$

$$\frac{\partial h}{\partial t} = -\frac{\partial U}{\partial x} \qquad (37)$$

If U = 0, the

$$\frac{\partial V}{\partial t} = -g(D+h)\left(B_r + \frac{B_i^2}{B_r}\right)\frac{\partial h}{\partial y} + f\left(A_i - A_r\frac{B_i}{B_r}\right)V - \frac{B_i}{B_r}x_T + y_T$$

$$\frac{\partial h}{\partial t} = -\frac{\partial V}{\partial y} \qquad (38)$$

with similar forms for the transformed equations (16). The Coriolis term is retained and bottom stress is not of the Chezy or Manning type. The above equations are not concerned with surface gradient perpendicular to the flow direction. Advective terms are ignored but surface stress and pressure gradient force are included. This contrasts significantly with classical hydraulics where storm driving forces are ignored but advective terms are included.

Two separate grid schemes are illustrated on a template in Fig. 9. The corner points '∘' have both U and V components of transport whereas the 'X' points have either U or V but not both. Both grids use the same 'h' or surge points. The first grid is labeled 'B', and the second, 'C' by Mesinger and Arakawa (1976). The C-grid makes no distinction between one- and two-dimensional flow. This property is one reason for its wide use in many models. Although the B-grid is not superior in several respects, it is the choice for the SLOSH model. It has the advantage of handling the Coriolis terms directly, of computing both components of space derivatives at a momentum point, and of computing symmetrically all spatial gradients, as well as the mean value for the total depth 'H'. One difference between the two grids is the ability to recognize slip/no-slip at boundaries and corner points.

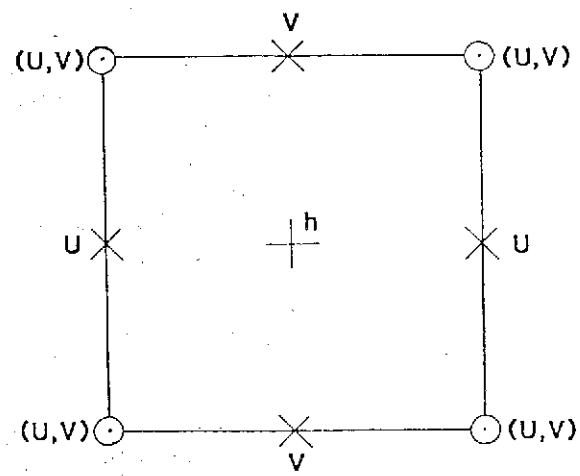

Figure 9. Two possible orientations of momentum points indicated by '∘' points and 'X' points. When one-dimensional flow is activated across unobstructed sides of a square, the 'X' momentum points are used in the equations of motion.

In the SLOSH model, stair-step rises and barriers terminate only at '∘' corner points. If a corner point is not overtopped but water exists on some or all squares surrounding the point, then flow in the vicinity is complicated. For simplicity with the B-grid, the no-slip condition is applied at all '∘' points not overtopped.

With the C-grid, stair-step rises and barriers do not terminate at 'X' points, and flow at corners is not referenced or addressed. However, slip along boundaries is implicit. The normal component of transport is set to zero at an 'X' point on a boundary, whereas, the parallel component is neither specified or computed. Boundaries or barriers are placed on the C-grid so that normal components of transport are at 'X' points.

Midway on line ab, Fig. 7, a transport component can be computed at an 'X' point. The C-grid does not concern itself with slip/no-slip at corner points 'a' and 'b'. Henceforth, when computations break down with the B grid at an unobstructed side and a head of water exists, the C-grid is then used to pass water through the side with the specialized one-dimensional flow equations, Eqs. (37) and (38).

Finite difference schemes for the C-grid are discussed by many authors (Mesinger and Arakawa, (1976); Reid and Bodine, (1968). We do not detail methods of computation except to note that three levels in time are used to conform with Eq. (33). (Two levels in time can be used for a savings in computer time and computer memory.)

It is usually assumed that transport is invariant across a side of a square with the 'C' grid. This assumption need not be a strict requirement. For example:

> If transports for both grids are combined in the continuity equation to compute the surge "h," then weights of say 1/2 are set for each grid. If the 'B' grid is inactive at corners, then the 'C' grid has an extra weight factor in the continuity equation; the weight factor of 1/2 means transport varies parabolically across an unobstructed side.

In the SLOSH model, the weight factor is ignored since the flow is too complicated to assume a specialized variation of transport across the side of a square.

We take many liberties with flow through unobstructed sides of a square. For example, if corners of unobstructed sides are overtopped during storm passage, there is little effect on the basin high waters if one-dimensional flow is ignored. The one-dimensional flow procedure is basically a cosmetic approximation for a complicated flow system of limited duration.

Again, consider line ab, Fig. 7, where the water height difference between two adjacent squares is called the "head." Before activating one-dimensional flow, there is much testing for the head of water across an unobstructed side. There are redundancies in determining the head according to combinations of dry and wet squares, overtopping the highest bed, overtopping a barrier, overtopping a sill if it exists, and overtopping level 'i', where 'i' is the lower height of the two corners 'a' and 'b'. Tests to formulate the head are as follows:

1. If both squares are dry, or none of the two wetted squares overtop the highest bed or sill, then the head does not exist. One-dimensional flow is not activated.

2. If both squares overtop 'i', then head is irrelevant and one-dimensional flow is not activated.

3. If the lowest wetted square is lower than the highest bed or sill, it is set virtually to the highest bed or sill height.

4. If the highest wetted square lies above 'i', it is set virtually to level 'i', where 'i' can be a barrier elevation.

If one-dimensional flow is activated according to these tests, then the head of water is substituted for the space gradient in the one-dimensional flow equations.

Several additional rules are followed for one-dimensional flow. If one, and only one, square overtops 'i', then both one- and two-dimensional flow are both active. There really should be a weight factor for the two flows, but this is ignored since both flows are active only for a small transitional period and water height above 'i' is small. For this special case, the storm's driving forces are not activated in the one-dimensional flow equations. (They are activated for the two-dimensional flow equations after initial rise above 'i'.)

A sheltering effect is applied to storm driving forces, similar in scope to two-dimensional flow. When actual (not virtual) water depth is less than 1 foot above the two beds, and in addition when mean water depth of the two squares lies between 'i' and 1 foot below 'i', sheltering is imposed. This method attempts to bring one-dimensional flow into agreement with two-dimensional flow at corner point 'i'.

For one-dimensional flow cases, the winds are weaker than over a large water expanse. For convenience, an arbitrary 25% reduction of stress (not wind) from "Lake" winds is used. Empirical tests show the surge insensitive to the 75% factor unless the stress direction is perpendicular to the "unobstructed" side, and only until two- dimensional flow is activated. A channel--formed from connecting squares with "unobstructed" sides--meanders, and the stress direction rarely parallels the meandering axis. If the meandering axis is not perpendicular to an unobstructed side, then the component of driving forces on the axis is rotated until perpendicular to the unobstructed side.

If the computed water level drops below the height of a square, the square is reset to be dry and the momentum in the continuity equation is altered to reflect this condition. Before initial inundation through an "unobstructed side," the momentum at an "X" point is initialized to zero. After exhaustion, it is set to zero.

As time marches on, and a storm inundates or exhausts inland terrain, the computational process switches between one- and two-dimensional flow.

Flow Thru Narrow, Deep Channels

An inland water body may be connected to another water body via a channel. If the channel is narrow, deep and long, then the most significant driving force can be the head of water between channel ends. If it is assumed the water level never touches bottom in a deep channel, then vast quantities of water can flow through the channel, even with only a small head.

Wide channels (several grid lengths in width) have significant cross currents relative to their major axis. In reality, these are inland water bodies, and the two-dimensional flow equations (1) are appropriate. If the channel width is small (grid size or less) with insignificant cross currents, then the one-dimensional flow equations, Eqs. (37) and (38), apply. The equations, however, are oversimplified and restricted, and if the channel axis is strongly meandering or at an angle to the grid network, then there are 90° changes in the flow direction at discrete intervals. These attributes may be too drastic to properly represent a deep channel. Instead, classical hydraulic techniques are used with simplifying assumptions. Several different techniques were empirically tested with the SLOSH model.

Comparisons show there were only small differences in the overall effects on surges across an inland water body. Accordingly, a simple technique is presently employed in the SLOSH model for narrow, deep channels.

A standard form for the momentum equation of channel flow (Chow, 1959), is

$$\frac{\partial u}{\partial t} + u\frac{\partial u}{\partial x} + g\frac{\partial y}{\partial x} = g(S_o - S_f) \qquad (39)$$

where y is the total water depth, u is the mean current, S_o is the bed slope and S_f is the energy slope translatable into current.

Consider a natural channel, Fig. 10, on a curving or meandering course. The length along the course is straightened as an x-axis. A cross-sectional area on the course is

$$A = \int_0^y \xi(x,\zeta)\, d\zeta \qquad (40)$$

where ζ is measured upward from the lowest level and ξ is the width at level ζ. The area varies along the course as the total depth, y.

The continuity equation is

$$\frac{\partial A}{\partial t} = -\frac{\partial (Au)}{\partial x} \qquad (41)$$

To set the continuity equation with total depth as a dependent variable, we have

$$\frac{\partial A}{\partial t} = \frac{\partial}{\partial t}\int_0^y \xi(x,\zeta)d\zeta = \xi(x,y)\frac{\partial y}{\partial t} = B\frac{\partial y}{\partial t}$$

where B is the width of the channel at the water surface, and,

$$\frac{\partial A}{\partial x} = \frac{\partial}{\partial x}\int_0^y \xi(x,\zeta)d\zeta = \int_0^y \frac{\partial \xi}{\partial x}d\zeta + \xi(x,y)\frac{\partial y}{\partial x}$$

$$= \left(\frac{\partial A}{\partial x}\right)_{y=\text{constant}} + B\frac{\partial y}{\partial x}$$

Hence, the continuity equation has the form

$$\frac{\partial y}{\partial t} + \frac{A}{B}\frac{\partial u}{\partial x} + u\frac{\partial y}{\partial x} + \frac{u}{B}\left(\frac{\partial A}{\partial x}\right)_{y=\text{constant}} = 0. \qquad (42)$$

It is a laborious task to deal with natural channels, Fig. 10, because of the complicated areal configurations. Instead, the cross sectional areas are simulated as rectangles of surface width, B, as obtained from charts. In this case,

$$\left(\frac{\partial A}{\partial x}\right)_{y=\text{constant}} = \int_0^y \frac{dB}{dx}\, d\zeta = y\frac{dB}{dx}$$

and the continuity equation becomes

$$\frac{\partial y}{\partial t} + y\frac{\partial u}{\partial x} + u\frac{\partial y}{\partial x} + \frac{uy}{B}\frac{dB}{dx} = 0. \qquad (43)$$

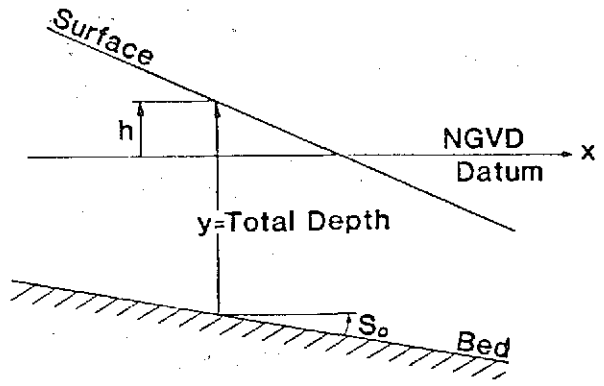

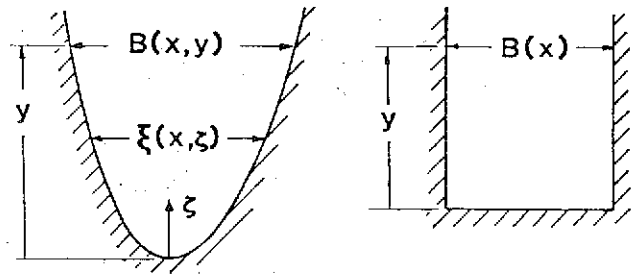

Figure 10. Cross-sections for a natural and an idealized prismatic channel. A horizontal channel can have a variable bed slope, S_o, and a variable water surface slope. The datum used in the SLOSH model is NGVD (National Geodetic Vertical Datum).

Multiplying Eq. (43) by $\sqrt{g/y}$, adding and subtracting Eq. (39) gives

$$\frac{\partial u}{\partial t} + (u\pm\sqrt{gy})\frac{\partial u}{\partial x} \pm \sqrt{\frac{g}{y}}\left[\frac{\partial y}{\partial t} + (u\pm\sqrt{gy})\frac{\partial y}{\partial x}\right] = g(S_o - S_f) \mp \frac{u}{B}\sqrt{gy}\,\frac{dB}{dx} \qquad (44)$$

Since

$$\frac{d}{dt}(u\pm 2\sqrt{gy}) = \frac{du}{dt} \pm \sqrt{\frac{g}{y}}\frac{dy}{dt},$$

Eq. (44) can be written as

$$\frac{d}{dt}\left(u \pm 2\sqrt{gy}\right) = g(S_o - S_f) \mp \frac{u}{B}\sqrt{gy}\,\frac{dB}{dx} \qquad (45)$$

along the characteristic lines defined by

$$\frac{dx}{dt} = u\pm\sqrt{gy} \qquad (46)$$

The last two equations are amenable to solution by the method of characteristics. They were solved, numerically, for channel flow, with the head between channel ends as the driving force.

Storm driving forces were not used since the meandering course of a channel negates its presence and most of the effect is to produce a slope across the channel. The bed slope S_o was permitted to vary with x, including adverse slopes; the width, B, was permitted to vary with x. Channels were deep enough so that the Froude number, $u^2/(gy)$, was always less than one.

The equations may represent physical processes within a channel, but this in itself is insufficient. What matters strongly are the end boundary conditions and the entrance and exit dynamics. These are not well known or observed under storm conditions. Because of the many imponderables, including detailed surveys of channels, a much simpler set of equations is used in the SLOSH model for channel flow, under the assumption that overall effects on a water body are not significantly different than when compared to more elaborate equations.

The channel is now represented as a rectangular prism of constant width and a bed slope of zero, Fig. 10. The flow is considered steady state. (Actually, a series of steady states for small time intervals is assumed, with the head changing slowly with time.) In this case, the momentum equation (39) becomes

$$u \frac{du}{dx} + g \frac{dy}{dx} = -gS_f \qquad (47)$$

The continuity equation is

$$y \frac{du}{dx} + u \frac{dy}{dx} = 0 \; . \qquad (48)$$

Combining the last two equations give

$$\frac{dy}{dx} = - \frac{S_f}{1 - u^2/(gy)} \qquad (49)$$

The friction slope S_f, is adopted from Manning's formulation (Chow, 1959) as

$$S_f = \frac{u|u|}{c^2 y^{4/3}}$$

where the width of the channel is much larger than the depth; c is a constant depending on the nature of the channel's bed. (c = 0.03 is used). In terms of transport q, where q = uy, is constant for steady flow, then,

$$\frac{dx}{dy} = \frac{c^2}{q^2}\left(\frac{q^2}{g} y^{1/3} - y^{10/3}\right) \qquad (50)$$

Quadrature gives

$$x - x_o = \frac{c^2}{q^2}\left(\frac{3}{4}\frac{q^2}{g} y^{4/3} - \frac{3}{13} y^{13/3}\right)\Bigg|_{y_o}^{y} \qquad (51)$$

integrating for x from x_o to x_L and for y from y_o to y_L. If we choose $y_L > y_o$, since $\frac{dy}{dx} < 0$, for subcritical flow ($u^2 < gy$), $x_L < x_o$. Now, let $x_L = x_o - L$, where L is the channel length, then the transport is

$$q^2 = \frac{\frac{3c^2}{13}\left(y_L^{13/3} - y_o^{13/3}\right)}{\frac{3}{4}\frac{c^2}{g}\left(y_L^{4/3} - y_o^{4/3}\right) + L} \qquad (52)$$

and the direction of transport is from x_L to x_o. All that is required is the channel course length and water heights at the channel ends. The heights at channel ends are derived from the two-dimensional flow equations in terms of the total depth, y, with bed depth of the channel related to a datum.

Comparison tests between Eqs. (45) and (52) show, in most cases, little difference in the overall effects inside an inland water body. There is a lag in events between the end points with Eq. (45), but this is not significant in an overall sense.

Overtopping the channel sides is not addressed; channel sides are assumed untoppable and the head between channel ends acts as the only driving force. Overland flooding is not coupled with channel flow; the channel itself is not incorporated in the terrain for two-dimensional flow.

7. BOUNDARY CONDITIONS

The placement of model boundaries and the application of appropriate boundary conditions is crucial in storm surge modeling, as it is in most modeling efforts. Model basins cover finite geographical areas; artificial boundaries must be placed across segments of a shelf and inland terrain. (The only exception is a grid covering a lake which is not connected to the sea. There, basin boundaries can be placed along the lake or at high terrain surrounding the lake.) Boundary conditions must be specified whenever water can exist along a boundary, but are not required along high terrain where surge never inundates. In storm surge modeling, the coastline acts as a moving boundary within a basin during inundation or recession of water.

Some surge models are run in a hindcast mode with a basin of small areal extent. In this mode, time-dependent, observed surge data along coasts and entrances to inland water bodies give a precise rendition to input boundary values. Such a procedure, unfortunately, is not applicable to forecasting. Boundary data are not available before the storm traverses the basin. However, one modeling alternative is to generate boundary conditions with a coarse shelf model, then to apply these boundary values to a fine-mesh limited area bay model. This procedure has some merit but there are objections with such uncoupled models. Sometimes, a coarse-mesh which encompasses a large area including the fine-mesh limited area, is used to generate boundary values. Again, there are objections, however, if the coarse mesh is too crude to properly represent events along the fine mesh boundaries.

The SLOSH model is designed for real-time forecasting. The rationale behind the model is to keep the forecaster's input to a minimum, with input variables amenable to forecast. It is not reasonable to ask a user to predict such input as surge boundary heights as a function of time. The model bypasses the need for input boundary values by placing artificial boundaries far from areas of interest. Computer storage constraints and economics, however, cannot place boundaries sufficiently distant for large, slow moving storms, passing at large distances from inland water bodies.

If boundaries are placed in deep water (> 150 feet) and far from shore compared to storm size, then superposition of hydrostatic heights (given by the storm itself) atop the quiescent or initial water levels is generally sufficient for a boundary condition. Static heights are determined by the storm as it traverses a basin. The hydrostatic condition is sufficient for small storms moving fast, but not always sufficient for

large storms moving slowly. The residence time of a large, slow moving storm (such as Carla in 1961) is sufficiently long to treat the Gulf of Mexico as a storage area; much water can accumulate inside the Gulf to raise deep-water boundaries to levels significantly above hydrostatic heights. Such rare storms require a special initialization treatment, discussed in section 10.

Artificial boundaries in shallow water or low terrain pose enigmatic boundary conditions. However, empirical tests show it is sufficient to place vertical wall boundaries on low-lying terrain and to use hydrostatic heights on shallow water boundaries if the following holds:

1. The core of the storm passes through a deep water boundary, and

2. the storm then traverses the interior of the basin, and

3. the storm then exits the basin through a boundary with high terrain.

This set of circumstances occurs for many storms passing through a given basin.

If a storm traverses a boundary in shallow waters, or fails to penetrate a basin's interior, the above simple boundary conditions are inadequate. Although the false boundary surges can affect much of the basin's interior, a bay or estuary may not be corrupted if the boundaries are sufficiently distant. For small storms moving fast, the residence time of surges is of short duration. The model spins up quickly from the initial state. Hence, in the basin's interior, the placement of a vertical wall along a low terrain boundary and the hydrostatic height boundary condition in shallow water is still effective. On the other hand, if the storm is large and traveling slow, then the false boundary surges have sufficient time to penetrate into the interior of the basin and can corrupt the computations in the area of interest. In this special case, it is desirable to alter the boundary conditions in shallow water with a dynamic boundary condition.

The interior of a basin is eventually affected by exterior events which pass through a boundary. If little or no surge activity takes place at a boundary, then boundary conditions are simple. In deep water removed from coastal effects, the surface stress creates momentum but rarely any surges. The pressure drop creates hydrostatic heights; hence, the applicable boundary condition is the hydrostatic boundary condition, or the inverted barometer effect as it is called. This is a Dirichlet boundary condition of prescribed values. The hydrostatic heights are placed at surge points. (At this time, the astronomical tide is ignored on a boundary. Tides are generally small compared to surges in the Gulf of Mexico, although they may be comparable along the Atlantic coastlines.)

In shallow water, it is useful to place the boundary nearly perpendicular to the coastline with one end located in deep water and the other end at high terrain. Observations show much surge activity can exist in shallow waters, and simple, prescribed boundary values are no longer adequate for many storm situations. Many types of boundary conditions can be employed such as radiation, absorption, etc Some work well for special cases; none work satisfactorily for all cases. Compromises must be made. After empirical trials with several boundary conditions, a convenient method was adopted for the shallow water portions of a boundary. Unlike the deep water boundary, an artificial boundary is placed along momentum points of a grid, Fig. 11. The product of the surge gradient and the total depth is set equal in value to the nearest momentum point inside the basin. This is applied in shallow waters less than 75 feet in depth, within about 20 miles of the coast. The almost-Neumann, almost-fixed curvature boundary condition is not used directly to compute surges. Instead, the momentum equation (33), with the almost-Neumann boundary condition substituted, is used to compute transports on the shallow water boundary. When a storm passes through shallow water, the mixed boundary condition permits large surge variations along the shallow water boundary. If the almost-Neumann boundary condition is applied throughout the boundary into deep water, the boundary vibrates slowly with time. By limiting the shallow water boundary condition to about 20 miles from the coast (e.g., storm size), the other boundary conditions control these vibrations.

In intermediate depth waters between 75 and 150 feet, SLOSH's boundary condition equates the surface gradient to the hydrostatic gradient (given by the storm itself), Fig. 11. The almost-Neumann boundary condition is not solved directly. Instead, the momentum equation (33), with the boundary condition substituted, is used to compute transports on the intermediate depth portion of the water boundary.

A no-slip (vertical wall) boundary condition is used over terrain. The Dirichlet or physical boundary condition could be abandoned for an almost-Neumann condition after sufficient inundation.* However, the inundation depth is usually small. Empirical tests give little change in surges inside the basin with either boundary condition. For convenience, the no-flow condition is retained at this time.

The mixed boundary conditions work reasonably well** for almost all storms, providing the storm traverses a basin's interior and the basin size is much larger than storm size. The size of a basin is determined from empirical test runs with the model for a variety of hypothetical storms and alternate basin sizes. No hard and fast rules can be given for basin size, but usually about 200 miles of coastline is sufficient with the offshore grid stretched out past the continental shelf.

For the rare case of a large storm moving slowly, and the track exterior to a basin, the boundary conditions have deficiencies regardless of

---

*Tests are underway for a "leaky" boundary after sufficient inundation.

**Not as well for resurgences forming exterior to the basin region.

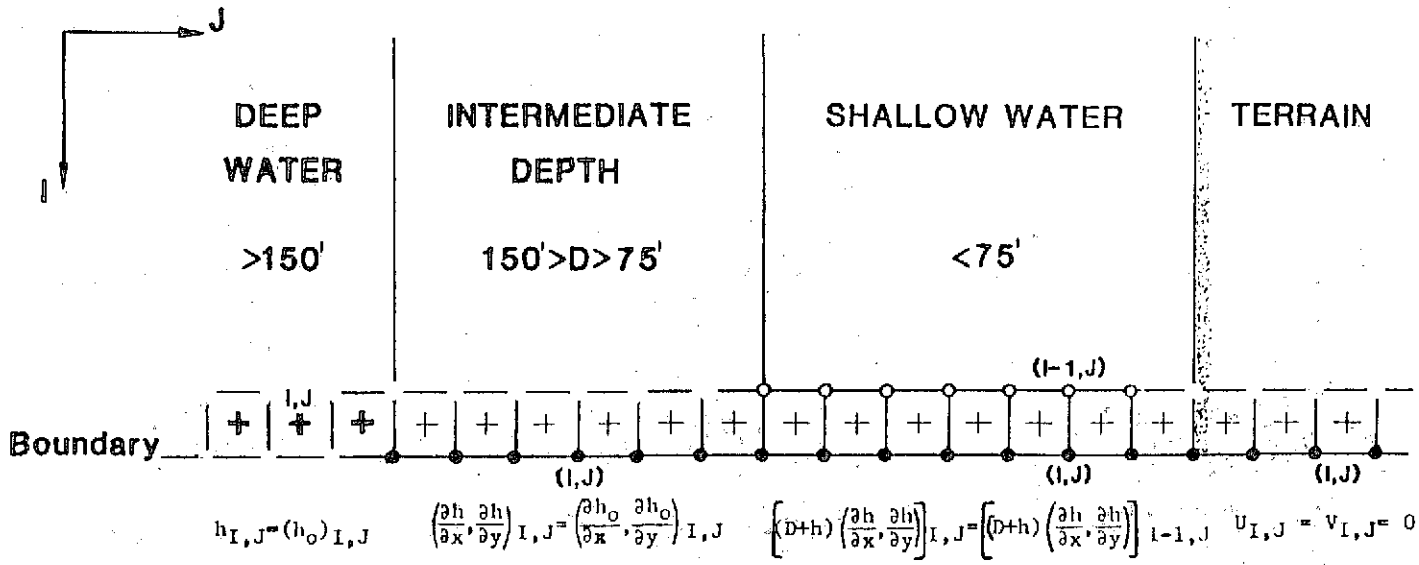

Figure 11. There are four boundary conditions presently in use with the SLOSH surge model:

1) Over terrain, the transport at momentum points is set to zero.
2) In shallow waters, the surface gradient in the equations of motion is replaced by the computed value at a contiguous, interior momentum point.
3) In intermediate depth waters, the surface gradient in the equations of motion is replaced by the storm's hydrostatic gradient.
4) In deep waters, the storm's hydrostatic height (inverted barometer effect) is set at height points of boundary squares.

the basin's size. From the initial state, the surge generates slowly, requiring a long computation in real time. Empirical tests with the mixed boundary conditions show inadequacies during the rising surge. However, the peak surges on inland water bodies are computed reasonably well. The implication is not to run the model with such storms if an accurate histogram of surges is desired. An alternative is to re-design basins to cover a sufficiently large area to contain all conceivable storm paths affecting a bay's interior.

8. DATUMS

Imposed on the quiescent, initial sea level are periodic astronomical tides and storm surges, Fig. 12. For commonality, all elevations of terrain, bathymetry, barriers, and surface water heights must refer to the same datum. Much confusion exists about datums, due perhaps to a simplistic view of Mean Sea Level (MSL). MSL is not the in-situ sea level at any specific time, nor is it time invariant with respect to "fixed" terrain. In the United States, three datums* are in common use:

1. MSL - A long term average of hourly tide gage readings.

2. MLW - Mean Low Water; a long term average of low-astronomical tide readings.

3. NGVD - National Geodetic Vertical Datum; established by geodetic surveys and optical levelings or transits.

The MSL and MLW vary through the years with respect to non-subsiding terrain; they are not used in the SLOSH model. For example, tide levels along the East Coast have shown a slow, but steady, rise over the last century. NGVD is used as the datum for the SLOSH model because of its temporal invariance. Also, land contours on U. S. Geological Survey topographic charts are referenced to NGVD. Hence, if inland inundation occurs, computed surges relate directly to published land contours.

To determine MSL or MLW along coastal regions, tide gages are anchored at a water depth lower than the anticipated lowest water. Whatever the depth, it is set as gage level "zero," Fig. 12. A long term average of hourly gage readings above gage-level-zero is called local MSL, relative to gage-level-zero. Similarly, local MLW is the average of all low water readings taken over a long period. Although it is possible to reference surrounding terrain heights to MSL or MLW datum (via gage-level-zero and its elevation to MSL or MLW), this is not done on topographic charts. Instead, geodetic surveys and optical levelings for the U.S. terrain are accommodated, in a best fit manner, to the datum NGVD. The NGVD datum was fixed in 1929, once and for all, by tying together geodetic level lines to agree with local MSL at

*There are, of course, other types of datums for different purposes; e.g., MHW (Mean High Water) under bridges.

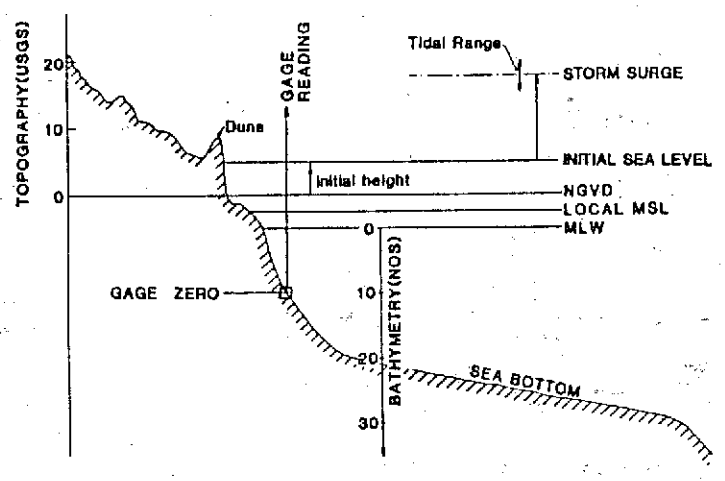

Figure 12. The initial sea level (without storm surge or astronomical tide) relative to various datums. NGVD is the basis for inland terrain contours and elevations on topographic maps. All vertical data, relative to another datum, must be translated to conform to NGVD.

26 gages along the U.S. and Canadian coasts. Since 1929, however, local MSL has drifted from NGVD. The difference is small in most cases.

If local subsidence occurs in a region, the land contours change with respect to fixed NGVD. To adjust subsided land contours to NGVD, a re-leveling or survey of the area is tied-in to near-by, non-subsided regions. Similar bathymetric changes are made. The most significant example of subsidence is in the Galveston, Texas area. In some parts of the area, land has subsided more than 5 feet since the 1929 leveling.

Since MSL and NGVD do not necessarily coincide, a tie-in of gage-level-zero and its elevation to MSL with respect to NGVD serves to determine any difference between datums. A table of differences for particular epochs can be obtained from the National Ocean Service (NOS) for the gages it maintains.

For navigational purposes, NOS bathymetric charts are referenced to MLW, Fig. 12. Hence, the difference between NGVD and MLW must be added to NOS bathymetric values. Differences vary across a chart but correspond roughly to local MLW differences at coastal gages.

The recorder of a tide gage can be set to any datum, be it gage-level-zero, MLW, MSL, or NGVD. To correspond with inland inundation and the SLOSH output, it is imperative to translate gage readings to NGVD. Gages are owned and maintained by government agencies and private industry; datums are not consistent. There is no single repository to query for datum clarification of gage observations. Instead, a case by case study is usually required to assure commonality in datums.

Tide gage repeaters in coastal NWS offices frequently give readings with respect to MSL. However, a few are referenced to MLW.

9. INITIALIZATION IN TIME AND SPACE

A computational SLOSH model run for surges begins well before the nearest approach time of a storm to a basin's origin. (We select a reference point within the basin, such as the entrance to a bay, as the basin's origin.) In principle, initialization could begin at the birth of a storm. For economic reasons, however, the period from initialization to nearest approach should be as short as possible. Too long is wasteful of computer resources; too short a period is insufficient for the sea to react to storm driving forces. What is desired is an optimal initialization time for computations to spin-up quickly to significant surge values, reproducing surges recorded on a real-time hydrograph. Also, the computed envelope of highest surges in an area of interest should not be sensitive to initialization time. In general, initialization time depends on the storm's size, the distance from the basin's origin to the storm's nearest approach, and the storm's forward speed along its track.

Some preliminary testing was done to optimize the initialization time. Based on these limited tests, the SLOSH model adopts the following scheme with a given storm, storm track, and basin origin:

1. From the time of nearest approach, the storm is moved backwards a distance six times the radius of maximum winds or six times the distance from basin origin to nearest approach whichever is larger. The preliminary initialized track position then gives the time of initialization.

2. If the storm is moving fast, the initialization time from (1) may be short. A minimum time of 18 hours before nearest approach of the storm is imposed by SLOSH.

3. If the storm is slow moving, the initialization time may be too long. Sixty hours before nearest approach of the storm is the maximum allowed by SLOSH.

After storm arrival at nearest approach, the storm continues along its track for another 12 hours. Although the peak surge generally will be computed, the additional 12 hours is inadequate for some storm situations if the receding stage for water inside a bay is required. Thus, the shortest, real-time run is 30 hours, the longest is 72 hours. The time duration is for a particular segment of a storm's track, before and after storm arrival at nearest approach. The user must ascertain or forecast this particular 72-h track segment, but need not be concerned with the remainder of the track.

This method of initialization is a useful approximation of sufficient generality to handle almost all conceivable cases. However, it may not be optimal for all storms and can be wasteful of computer resources. The SLOSH model requires longer real-time runs than simple shelf models because SLOSH treats water flow, flooding and receding water well inland from the coastline.

The SLOSH model initializes the water level within a basin in space with observed, quiescent, coastal sea levels before a storm reaches nearest approach. For most storm situations, initialization takes place 18 hours before nearest approach, with the storm well out to sea and exterior to the basin. The still waters along coasts do not have significant elevation changes until a few hours before storm arrival. Hence, the average gage readings approximately two days before storm arrival, can be used for the initial water height.

An exception to the above initialization occurs in the Gulf of Mexico for large storms moving slowly. The initialization time may then be 60 hours before nearest approach. The long duration of the storm can add significant amounts of water to the Gulf and to the basin's interior. In effect, the Gulf acts like a large storage basin. After the storm's passage, the stored water remains in the Gulf for some period of time. Tide gage readings at initialization may be several feet above normal, even in the absence of any storm winds along the coast. Initial water height throughout the basin is treated as the observed elevation along the coast the inside bays at the time of storm initialization. If the program is sent to the computer, say, 24 hours before nearest approach, then the initial, still-water height of the basin is obtained from previous tide gage readings. The user supplies the observed sea level 48 hours before nearest approach to conform with most storm situations. There may be a problem if initialization is 60 hours before nearest approach. However, in most cases, the rising stage between 60 to 48 hours before nearest approach is small.

In addition to the initial, quiescent water level, static height elevations due to the storm's pressure drop at the initial time are added to the initial water height for oceanic areas, but not for inland water bodies. The initial static height elevations are almost non-existent for small storms and only a very small fraction of a foot about the coast for large storms moving slowly. In almost all cases, the static heights can be ignored if the storm is initialized outside a basin's interior.

10. VERIFICATION

Verification experiments with the SLOSH program were performed in the same manner as real-time operational runs. The model is applied the same way for all storms and in all basins. Initialization time is a function of storm size, speed along storm track, and distance of bay to nearest approach of the storm. These storm parameters are input for a storm wind model to generate driving forces. No input boundary values with time are required. Initial, quiescent water heights are determined from tide gages 48 hours before the storm affects the basin. Calibrated coefficients for the model are set universally; they are invariant for any storm, basin or local conditions. Although the method appears objective, this is not completely true since storm character and basin configuration are not predetermined by an unbiased arbiter. Some juggling or refinement of input and basin data almost always occurs before finalizing a verification run.

"Ad-hoc" historical storm parameters were first assembled from various sources. Such data is almost always too coarse, usually with parameters prescribed invariant with time and with a heavily smoothed storm track. In many cases, a "best-fit" smoothed track can differ substantially from a "best-fit" landfall point. When deemed necessary, further analysis and subjective decisions amended the storm's track and parameters, especially surrounding storm landfall time.

During the basin development stages of SLOSH, preliminary experimental runs with past hurricanes are compared to all available observed surge data. The basin data are checked in areas of disagreement and amended if necessary. The amended data were not designed to force agreement with computed and observed surges but rather to affect fuller cognizance of basin geometry. As an example, if within a basin the computed surges appeared reasonable in one region but not another, then vertical barriers and basin geometry between the regions are closely scrutinized. In some cases, there are irregularities and missing values in bathymetric/topographic charts, inaccurate or misinterpreted barrier heights, or even improperly entered input data. Sometimes visual surveys suggested revision of barrier heights on charts; e.g., a solid, vertical, concrete barrier between lanes on a highway, well above crown height. In some cases, man-made barriers may not even be present on the latest available charts. Sometimes, subgrid sized configurations such as cuts between barrier islands are introduced to better describe flow in certain areas.

The numerous jumps in terrain elevations destroy bottom continuity. As a result, many subjective decisions such as the amount of smoothing imposed are made while composing input basin data in completed form. In most cases, these decisions have only a cosmetic effect on the computed surge. However, major changes in the flooding patterns can occur whenever water levels are at or near the top of barriers.

The following verification experiments were run with basin data that approximates the basin conditions at the time of the hurricane. Basin data are continually updated whenever new information becomes available. An example is subsidence in the Galveston Bay area where bottom configuration continuously changes with time. Hence, present basin data for operational runs may differ from that used for verification runs, especially for historical storms far back in time.

Detailed basin data (bathymetry/topography, barriers and their positions on a grid, etc.) are not illustrated in this report. They can be made available to interested users on request.

a. Surges Over Lake Okeechobee, Florida, Using a Cartesian Grid

It is informative to initially test the SLOSH model with a simple basin, unaffected by events in surrounding water bodies. If the model output does not compare favorably with surge observation, then performance is questionable with more complicated basins. An enclosed, inland lake would be ideal. In this special case, boundary conditions with respect to time along termini of the model's grid system need not be supplied.

There are no datum inconsistencies from tie-ins to neighboring regions, and there are no astronomical tides.

Lake Okeechobee in Florida is an excellent candidate basin. It is shallow with maximum water depths about 14 feet, and an average depth less than 10 feet. The surface height varies seasonably, but is between 14-17 feet above NGVD during the hurricane season. The surface area is similar in size to the core area of most tropical storms. There is no connection to the Atlantic Ocean or Gulf of Mexico, except for shallow canals and waterways which have small flow rates, insufficient to appreciably change the lake level during storm passage. These special conditions relax the necessity for a large area basin. In this case a simple, Cartesian, fine-mesh grid can be used for computations.

Figure 13 illustrates the levee system bounding the lake as it existed in 1974. The operational SLOSH program for Lake Okeechobee uses the latest available information on the levee system, (National Weather Service, 1978). However, a test case for the SLOSH model is the 1949 storm when a different levee system, of lesser extent, existed.

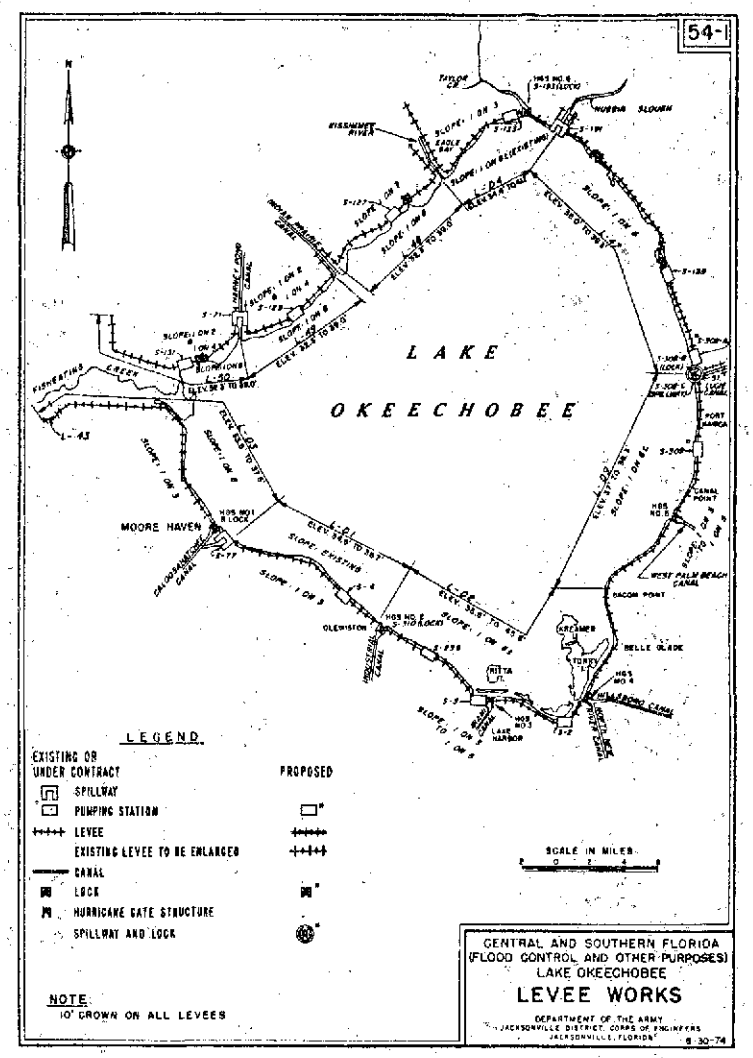

Figure 13. The present levee system (1974) surrounding Lake Okeechobee, Florida. Courtesy, U.S. Army Corps of Engineers, Jacksonville, District, Florida.

The levee system in 1949 excluded the northwestern boundary of the lake where a low road (highway 78) crested a few feet above terrain. The northern end of the levee turned to the northwest and the other end to the west. The low road running along the northwestern boundary was set 18-22 feet above NGVD, or 2-4 feet higher than local terrain. Portions of the levee system on the east side of the lake were a high road. The levee crests were set (arbitrarily) to 32 feet above NGVD, even though the crests at the Southern boundary of the Lake were higher. The levees were not overtopped during the 1949 storm, although the low road on the northwestern boundary of the Lake was overtopped.

A stair-step depiction of the levee system on the Cartesian grid and straight line boundaries for the basin are illustrated by Fig. 14. The instrumented positions on the Lake are shown as LS and HGS Stations. Figure 14 is drawn on transparent material and used as an overlay to fit over numerical output from a line printer. The basin is covered by a 32x38 grid with one-mile squares.

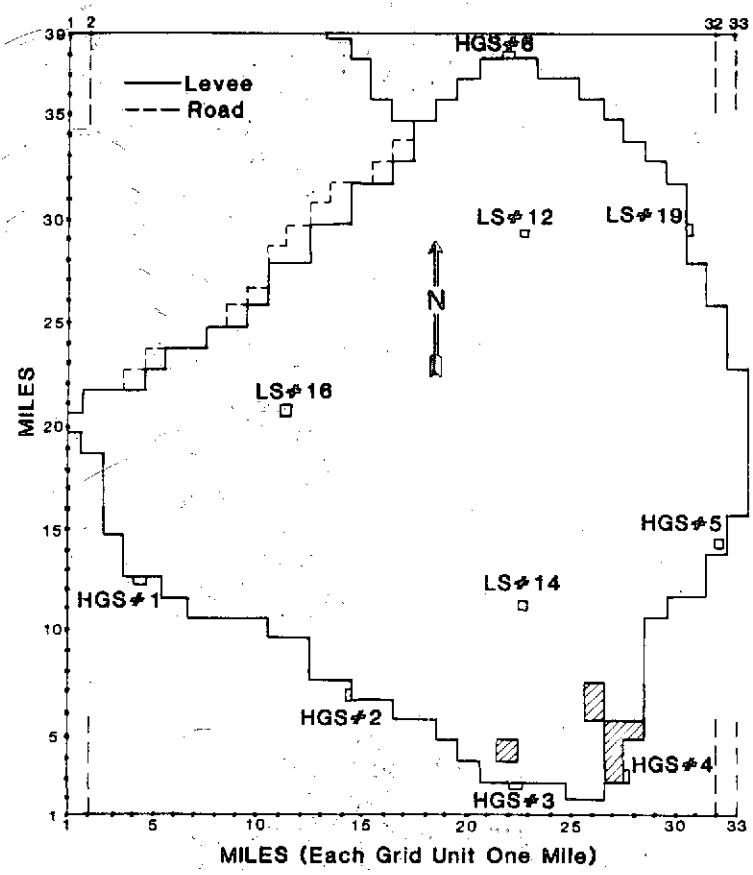

Figure 14. A simple overlay for Lake Okeechobee, Florida, outlining the lake in stair-step fashion. When laid atop a printed surge output, surge contours can be drawn for visual effect, such as Figs. 15 and 16. Lake Station (LS) and Hurricane Gage Station (HGS) are instrumented locations on the lake.

The grid lines bounding the model basin are modeled as vertical walls of infinite height; overtopping of the walls is not permitted. If fluid strikes a synthetic wall, it will stagnate or reflect back into the basin's interior. For a fully operational model, it would be desirable to place the walls sufficiently distant for any conceivable inland inundation. The model basin, however, is severely restricted in design with only

a limited area enclosing the Lake It is a special case, sufficiently complete to test for overtopping of levee systems in particular for the 1949 storm. Flooding across the low road of the incomplete 1949 levee can be computed for only a limited distance inland. If overtopping of levees occurs, then the model may no longer perform properly because of reflections from nearby false boundaries enclosing the basin. This restriction can be removed by expanding the model's coverage.

The Cartesian grid lines intersect to form one-mile squares. Depth values of the lake, at the center of squares, were visually extracted from NOS chart 855-SC. Terrain heights, on grid squares were extracted from available topographic charts. Alternate portrayals of stair steps, or different orientations of the grid system, result in some differences of the computed surge near boundaries, provided the boundaries are not overtopped. If boundaries are overtopped, with massive inundation inland, then the original boundary is submerged and the local area becomes an interior region of a basin. Despite the presence of stair-steps boundaries, there still may exist a useful comparison with observed surges along real, unovertopped boundaries.

A time step of 75 seconds was required for the explicit finite difference scheme of the SLOSH model; this was determined by empirical tests with extreme storms overtopping levees. (With a two-level in time finite difference scheme, a 150 second time step is required.)

The islands at the southern end of the lake are about 16 feet above NGVD and surrounded by low levees or barriers two to four feet higher. It is doubtful that the barriers will hold during storm conditions, but so assumed in the model. The simulation of such islands on mile squares is a crude approximation.

Hurricane of August 26-27, 1949

Lake Okeechobee was fully instrumented for meteorological and surge observations during 1948. In August 1949, a storm passed the northeast portion of the Lake. No major storm, up to 1989, has since passed over the Lake. To date, no other water body has such a dense array of observed meteorological and surge data during a hurricane's passage.

Before storm arrival, the surface height of the lake was just below 14 feet NGVD. After storm passage, the level rose to just above 14 feet. The small difference may be ascribed to rain and runoff. A convenient value of 14 feet was used to represent the initial, quiescent surface in the model. No account was made of mass changes due to rain, runoff, or admittance through gates.

A 24-h verification run was made with model "Lake" winds for the 1949 storm. Tests with shorter, 18-h runs did not alter the computed surges during storm traverse across the lake when surges were highest. However, for slow-moving storms, longer runs may be necessary. A 24-hour run proved adequate for the 1949 storm over Lake Okeechobee.

A computed, hand-contoured, surface envelope of minimum surges without regard to time is displayed in Fig. 15. A sizable portion of the lake

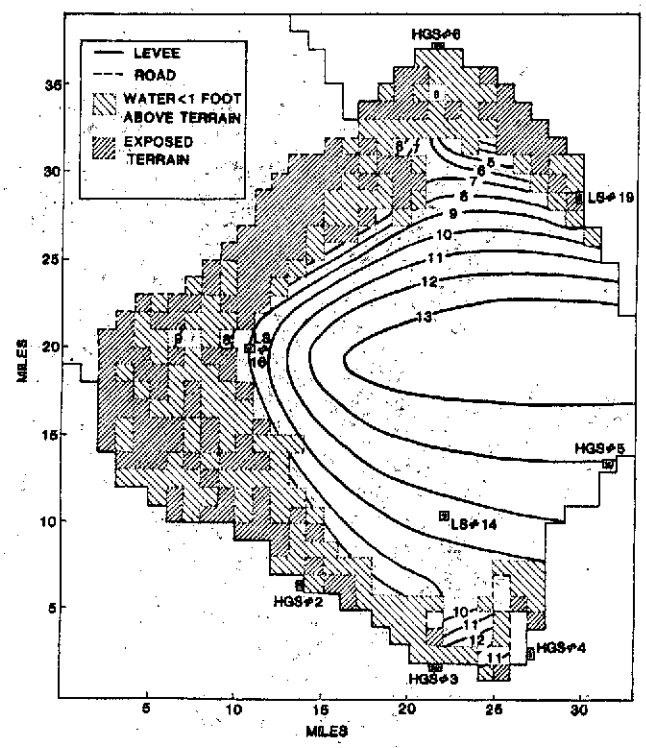

Figure 15. A surface envelope of lowest waters, independent of time of occurrence, computed by the SLOSH model for the 1949 storm. The contours were hand-drawn on the overlay of Fig. 14 which was placed atop line printer output.

is exposed, but not simultaneously in time. The model has the ability to simulate a receding boundary. There are no observations to compare with the minimum envelope, except for noting which gages touched bottom. Notice how water stagnates in localized depressions.

A similar surface envelope of maximum water heights without regard to time is displayed in Fig. 16. Only a small region to the northwest of the lake is inundated after overtopping a low road. None of the levees surrounding the lake are overtopped but all of the islands on the southern end of the lake are overtopped and flooded. There are no observations of inland surges to compare with model computations for inland inundation.

There are eight gages with observed data on the lake. Six of the gages are along lake boundaries. The character of the computed surges agrees with observations, Fig. 16. There are some amplitude differences, especially on some tail ends of the surge profiles. This suggests an incomplete portrayal of winds by the storm model, before and after storm passage, which could be due to:

1. A complicated distortion of pressure isobars during storm motion over land. The storm model uses a simple, crude correction for pressure distortion overland. This correction may not be adequate.

2. Large changes or jump discontinuities of the storm's central pressure at landfall on the east coast of Florida, before and after storm passage across the lake, and later dynamic changes. The input pressure parameter used had a smooth monotonic character, Fig. 3; it may not be representative

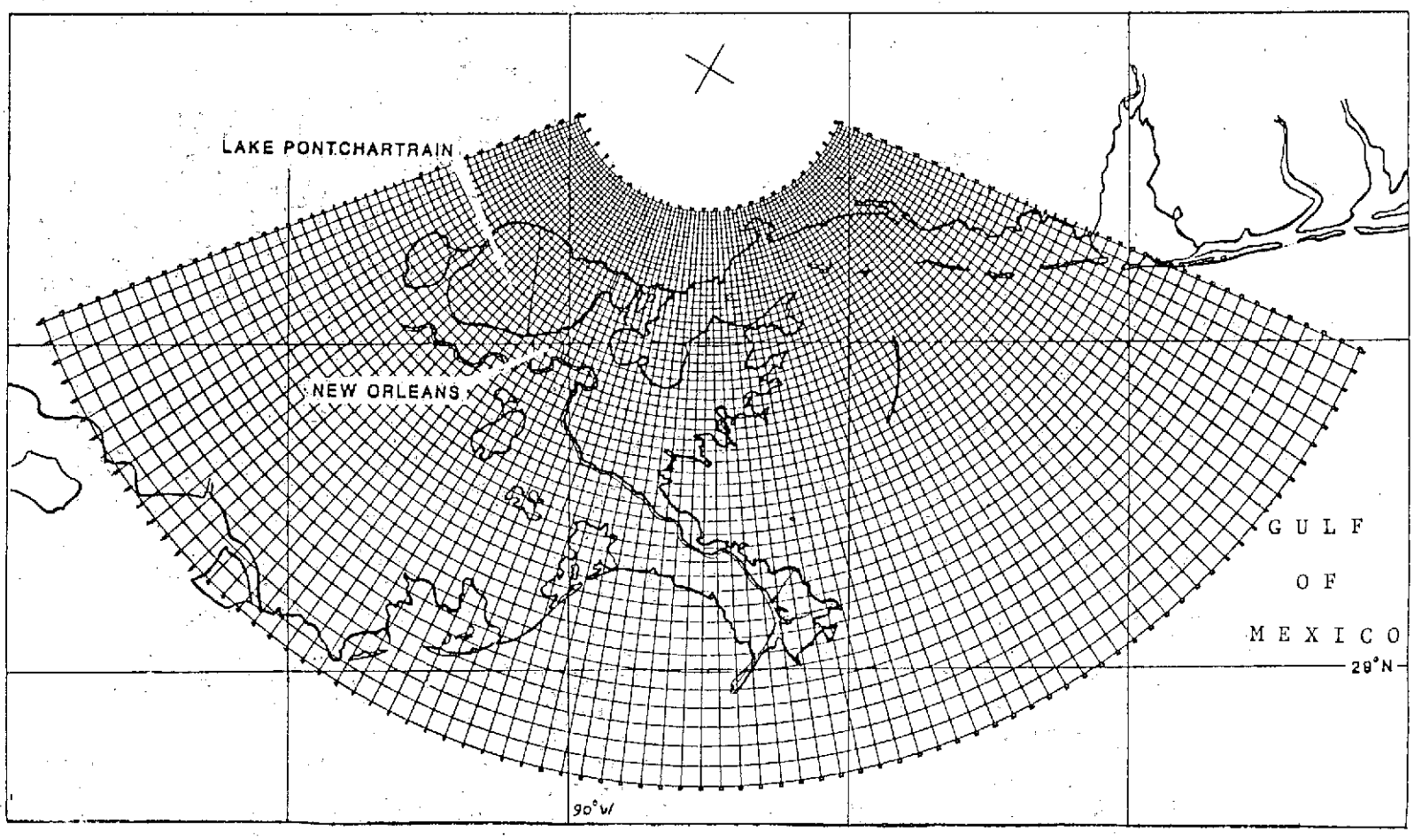

Figure 17. A plane, polar coordinate system (projected on a Mercator chart), tangent to the earth at New Orleans, Louisiana. The grid encompasses Lake Pontchartrain, Louisiana.

of the storm when it was positioned away from the lake.

3. Complicated variations of storm size as it traversed land. The storm parameters were varied continuously with time. Such a simplistic variation is questionable.

These subtle, onshore hurricane dynamics are less important to a shelf model when storms landfall on a long, unbroken coastline. To a shallow inland lake, they can be significant. A lake has limited area, does not "see" the entire storm at any instant of time, and reacts quickly to suddenly changing force fields.

A storm surge model cannot be judged on the results from one storm in one simple basin. However, the SLOSH model is a major extension of the SPLASH model which was tested for coastal surges for many storm situations in many different shelf basins. The surface drag coefficient and the bottom stress coefficients used in SLOSH are the same as those used in SPLASH. No local calibration or tuning was performed to force agreement with observed surges on the lake.

The SLOSH storm and surge models appear to be useful for forecasting surges if the storm's core passes a basin. However, surges generated on a small body of water by the tail ends or periphery of a storm may not be adequately described by the model.

b. Surges Over Lake Pontchartrain, Louisiana, Using a Polar Grid

The geographical placement of a polar grid, representing the surface of a basin region and transformed onto a map projection, is illustrated by Fig. 17. The grid expands/contracts continuously along rays emanating from the origin of the grid. The areal extent of the grid, positioning of its origin or pole on the earth, grid expansion rate, etc., are decided subjectively by the modeler with due attention to regions of interest, geographical constraints and population centers. The map is a Mercator projection with straight latitude and longitude lines. The grid layout is eminently suited to modeling storm surges, but is inadequate to display computed surge values with an ordinary line printer. Specialized transformations of the earth's surface onto a plane are adapted to simplify numerical computations, to position the grid on a particular map projection, and to simplify output for a line printer.

The ellipsoidal earth is first transformed conformally onto a sphere and then projected conformally onto a plane. Spherical coordinates are not used in surge computations. The plane, containing a polar coordinate system, is tangent to the sphere at a selected point--New Orleans on Fig. 17. The tangent point is not the origin of the polar grid, but is arbitrarily chosen to give least basin distortion at the region of greatest interest.

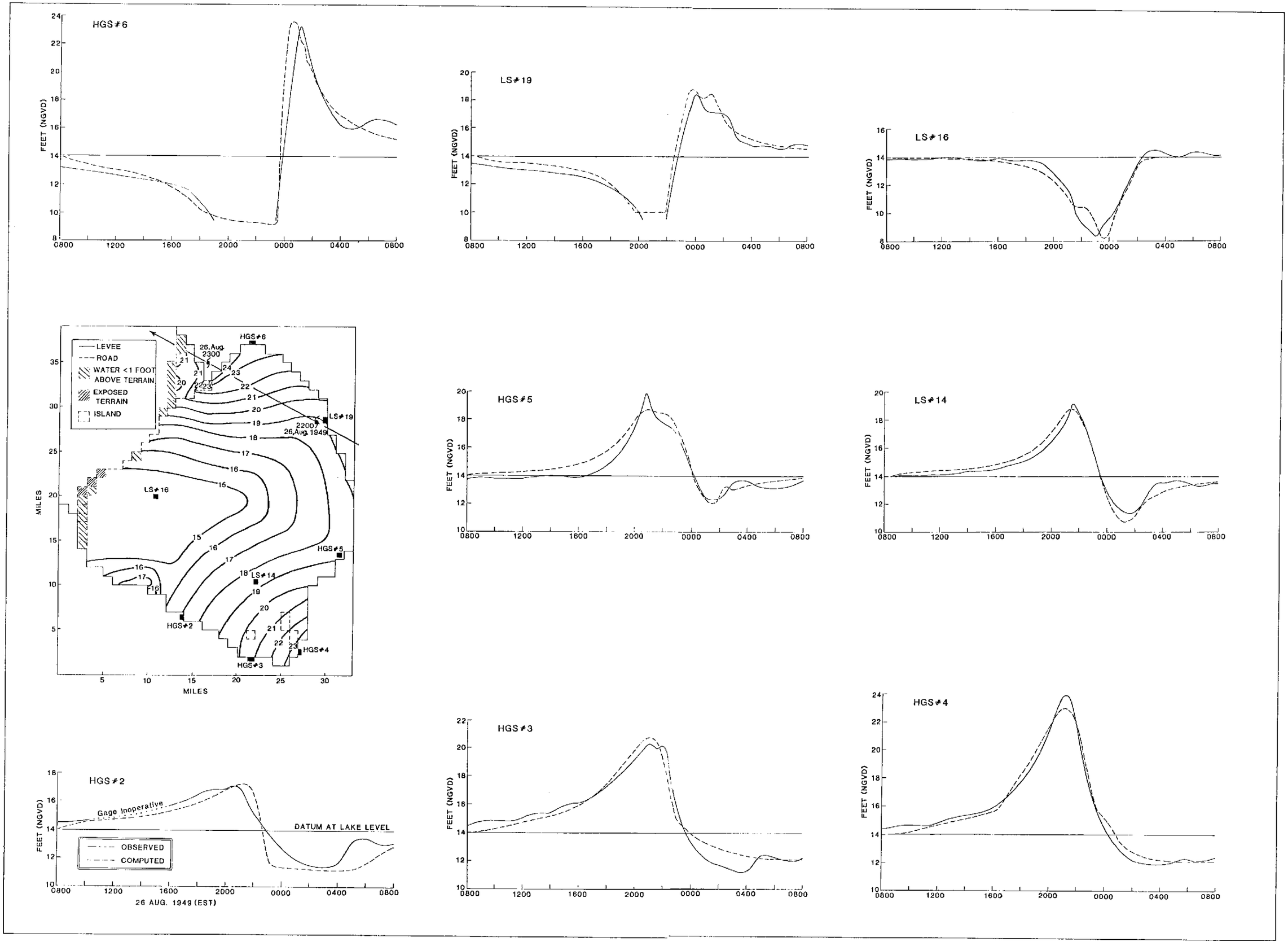

Figure 16. Observed and computed surge hydrographs at eight locations on Lake Okeechobee, Florida, for the 1949 hurricane. A surface envelope of highest waters, regardless of the time of occurrence, is shown in the left center insert. The contours were hand drawn with the overlay of Fig. 14 placed over printer output.

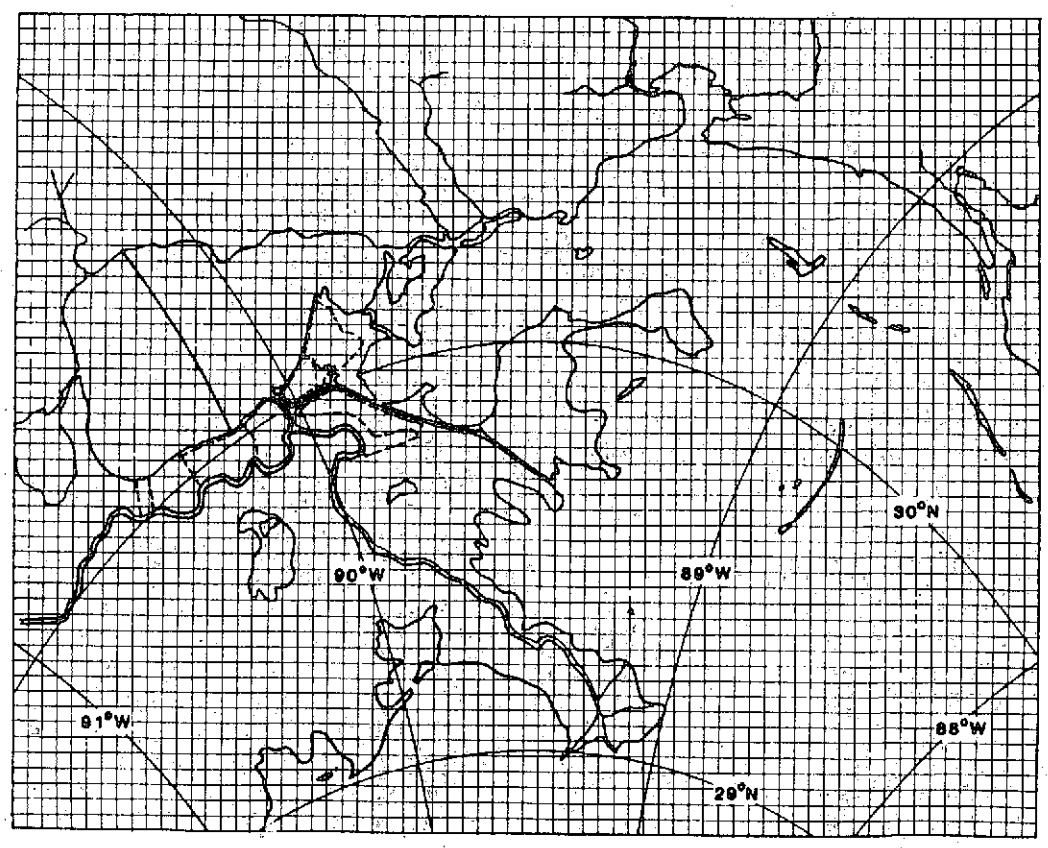

Figure 18. A transformation of the polar gird, Fig. 17, onto an image plane. The transformed grid lines intersect as squares; hence, equally spaced surge values can be printed with a line printer. The projected latitude and longitude lines are distorted accordingly on the image plane.

To process input data from surface map features, the plane must be transformed back onto any given map projection, with latitude and longitude lines coinciding, say, on the Mercator map of Fig. 17. The grid lines, of course, are distorted accordingly. The grid intersections always fall on the same geographical points, no matter the map projection or scale size. After transformations are defined, an X-Y plotter is used to accurately place the transformed grid lines onto particular bathymetric and topographic charts. Literally, the grid is positioned across hundreds of maps, differing in projection and scale, to discretize surface map features for input basin data.

To output computed surges on a line printer, it is useful to transform the initial polar grid onto an image plane with equal grid spacing. The image grid has equally spaced lines, straight and parallel, forming a square grid. Naturally, the latitude and longitude lines and all surface features projected on the image plane become distorted, Fig. 18. The surface map features can be drawn with an X-Y plotter from a database, or else hand-drawn from published charts.

Figure 19 is an example of a printed surge output on the image plane. Such output can be an envelope of maximum computed surges or a snapshot display of surges at a given time. Computed surge values are printed at the center of grid squares. The special symbols, '.' and 'WET', mean dry land and water depth less than one foot above terrain, respectively. For later geographical alignment, discretized symbols are printed to isolate geographical features. Coastlines appear as '+' symbols. Cities are located with '*' symbol and are alphabetically spelled out. Latitude and longitude lines are indicated by 'T' and 'G', respectively. All the symbols and their discrete placement on printed outputs are preset as basin data. Their print positions are determined by transforming Fig. 17 to Fig. 18. The storm track across a basin is designated by '$' symbols, with ( ) symbols at hourly positions.

It is difficult for the eye to appreciate map features with discretized symbols. To aid orientation, a special transparent overlay, similar to Fig. 20, is prepared for each basin. The overlay displays map features, hand drawn in various colors; e.g., coastlines, topographic contours, barrier impediments, channels, latitude and longitude lines, etc. Elevation contours over land and barriers are also displayed. The overlay, placed atop the printed output, is aligned along latitude and longitude lines, and other discretized symbols. The overlay not only serves to orientate the user, but also ascertains inland flooding on the computed surge output. The difference between printed surge heights and contour elevations on the overlay is the total depth of water above terrain.

The above procedures were followed for all verification runs when using a polar grid with the SLOSH model.

The basin for Lake Pontchartrain was originally encompassed with a Cartesian grid of 4-mile spacing (Crawford, 1979). Even with such a coarse grid, the computed surge values verified reasonably well over the lake with four historical storms. The grid, however, is much too coarse for many features of the basin and also

across small water bodies such as St. Louis Bay, Mississippi. The coarse-grid model did compute an overall, useful, surge prediction for a weak storm, Hurricane Bob, 1979, with the model running in a real-time, operational forecast mode.

The model for Lake Pontchartrain has now been updated with a polar grid Fig. 17. The grid spacing is one to two miles across the Lake and about one mile across St. Louis Bay. It expands to slightly over 4 miles in the Gulf waters.

Three deep-water passes, connecting lakes in the model, are simulated with the following physical specifications:

	Mean Depth Below NGVD	Mean Width	Length
Rigolets	30 ft	3000 ft	8.5 mi
Chef Menteur	30 ft	1000 ft	7.5 mi
Pass Manchac	20 ft	500 ft	6.0 mi.

Levee systems and their elevations surrounding New Orleans, the Mississippi River, and the Bonnet Carre Floodway, were assembled from data supplied by the Corps of Engineers, New Orleans District. Other basin features and elevations, were extracted from NOS bathymetric and storm-evacuation charts and USGS topographic maps.

Relative to NGVD, the gages inside Lake Pontchartrain consistently read higher than NOS gages along coastlines. This presents a dilemma for initialization since a difference would pour water out of the Lake at the beginning of a computational run. Assuming inadequate leveling along the Lake, the following fix-up procedure is adopted for use during computations and to recorrect computed surge values for output:

First, the entire lake is virtually depressed by 1.0 feet, and tapered to a zero depression just past the three channels. The Lake's bed and surface elevation is depressed relative to NGVD but the total depth of water above the Lake's bed is not altered. Second, the computed stored surge values for output are reconditioned by removing the virtual depression. This procedure has no significant effect on surge computations; it only translates heights to reflect the discrepancy in tide gage readings. The reverse correctionn is applied when computations are completed. In this way, the initial, quiescent water surfaces are nearly level throughout the basin and the finalized form of the computed surge output corresponds with present leveling of tide gages and observed high water marks.

Some low terrain within New Orleans is below zero datum and is surrounded by levees. The model initially sets the low terrain dry, even though the surfaces of surrounding water bodies are higher than terrain height. The surrounding levees prevent flooding into the low terrain, unless overtopped by a surge.

The grid is too coarse to resolve Biloxi Bay, Mississippi. When applicable, however, one-dimensional flow equations are activated to simulate surges through this bay.

The Mississippi River is ignored, except for the levees along each of its sides. These levees act as barriers to overland flow. It is possible for a surge wave to travel up the River between the two-sided levee system, from the Mississippi Delta to Baton Rouge, Louisiana. Such flow is presently ignored in surge computations.

The Mississippi River Gulf Outlet Canal and the Intracoastal Waterway are ignored. These channels are important for long term effects, but empirical experiments with the SLOSH model show only minor effects during the transient surge generated by a tropical storm.

Hurricane Betsy, 1965

The most devastating storm affecting southeastern Louisiana in recent times was Hurricane Betsy, 1965. The storm track paralleled the Mississippi Delta on the west side, Fig. 21. Betsy's track and storm parameters were supplied by the Office of Hydrology of the National Weather Service. Maximum winds of the storm passed through the vicinity of the city of New Orleans. As the storm made landfall, the parameters were modified with time according to land station observations. These modifications are necessarily coarse, even subjective, because of the skimpy data base. Because of the storm's large size, the track, landfall point, and storm size need not be precise. Tests with small changes in landfall point, storm size, and track, all within meteorological accuracy, gave only small changes in the computed surge. The meteorology was not changed to give an optimal comparison of observed and computed surges.

The Parishes of Citrus and New Orleans East were flooded in real life, as well as the northeastern part of New Orleans.

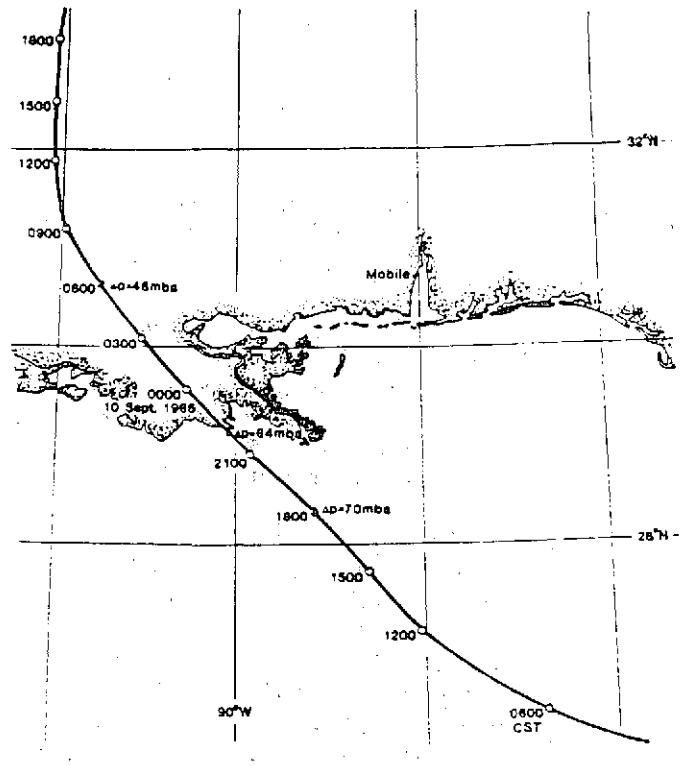

Figure 21. Meteorological input parameters for Hurricane Betsy, 1965.

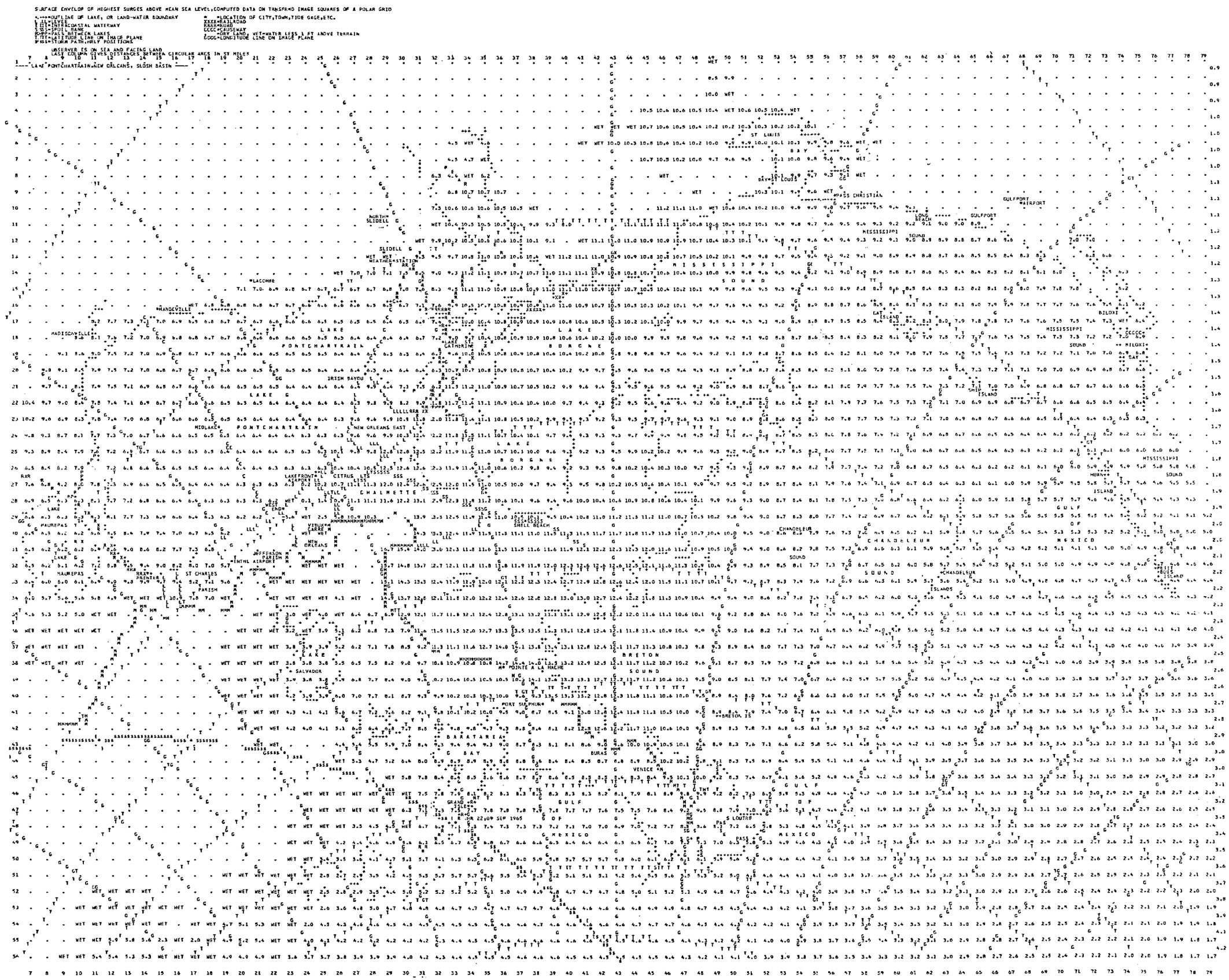

Figure 19. An example of printed surge output from a computer line printer. The surge values are located at the center of the image squares shown in Fig. 17. The hurricane's track is represented by the series of '$'-signs in the figure.

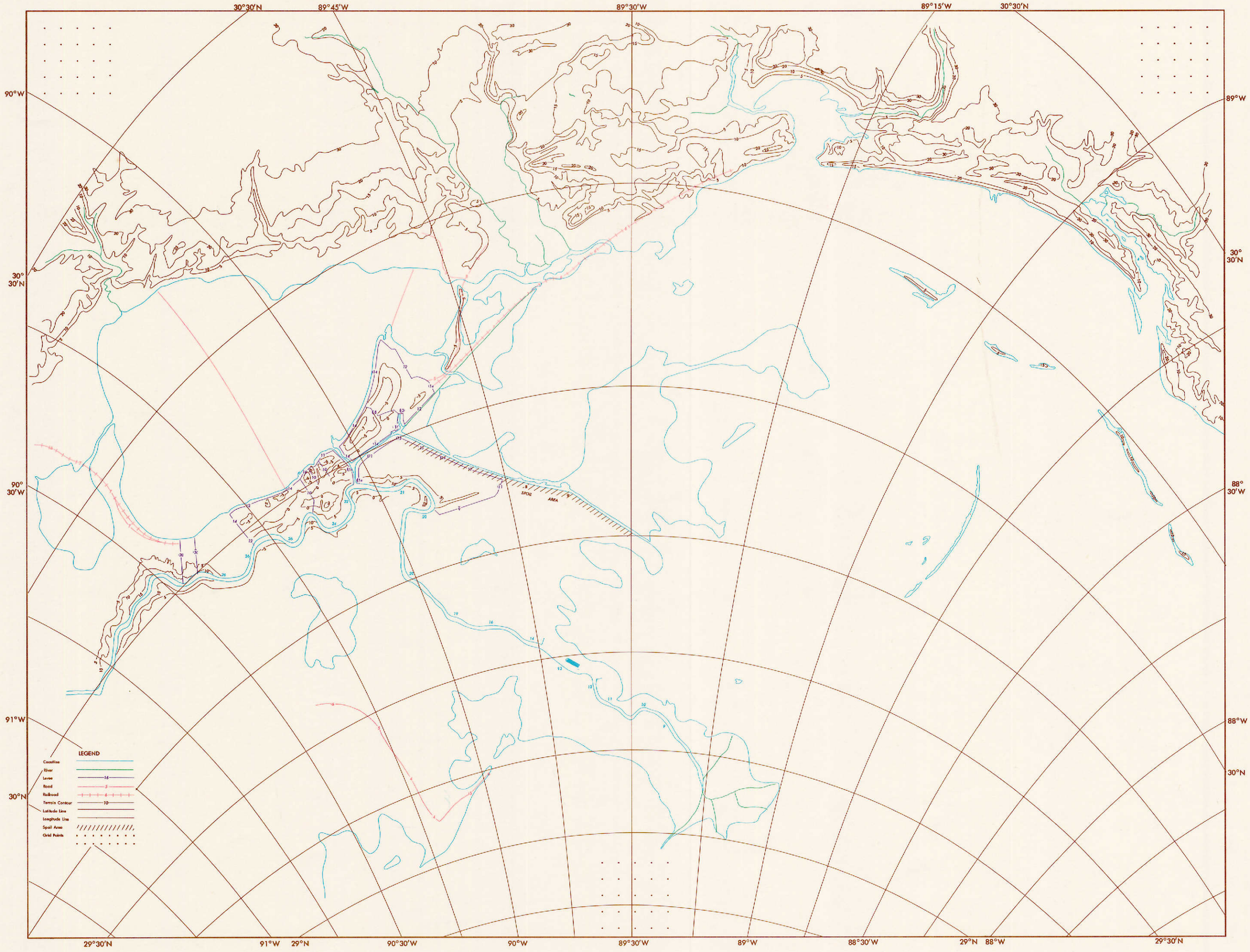

Figure 20. An overlay to locate geographical features on an image plane, transformed from the polar grid as in Fig. 18. The coast, terrain contours, levees, roads, railroads, and spoil banks are positioned appropriately on this image plane. Barrier heights are also specified. The overlay is designed to be placed over printer output such as Fig. 19. The user can then ascertain the limits and degree of inland inundation.

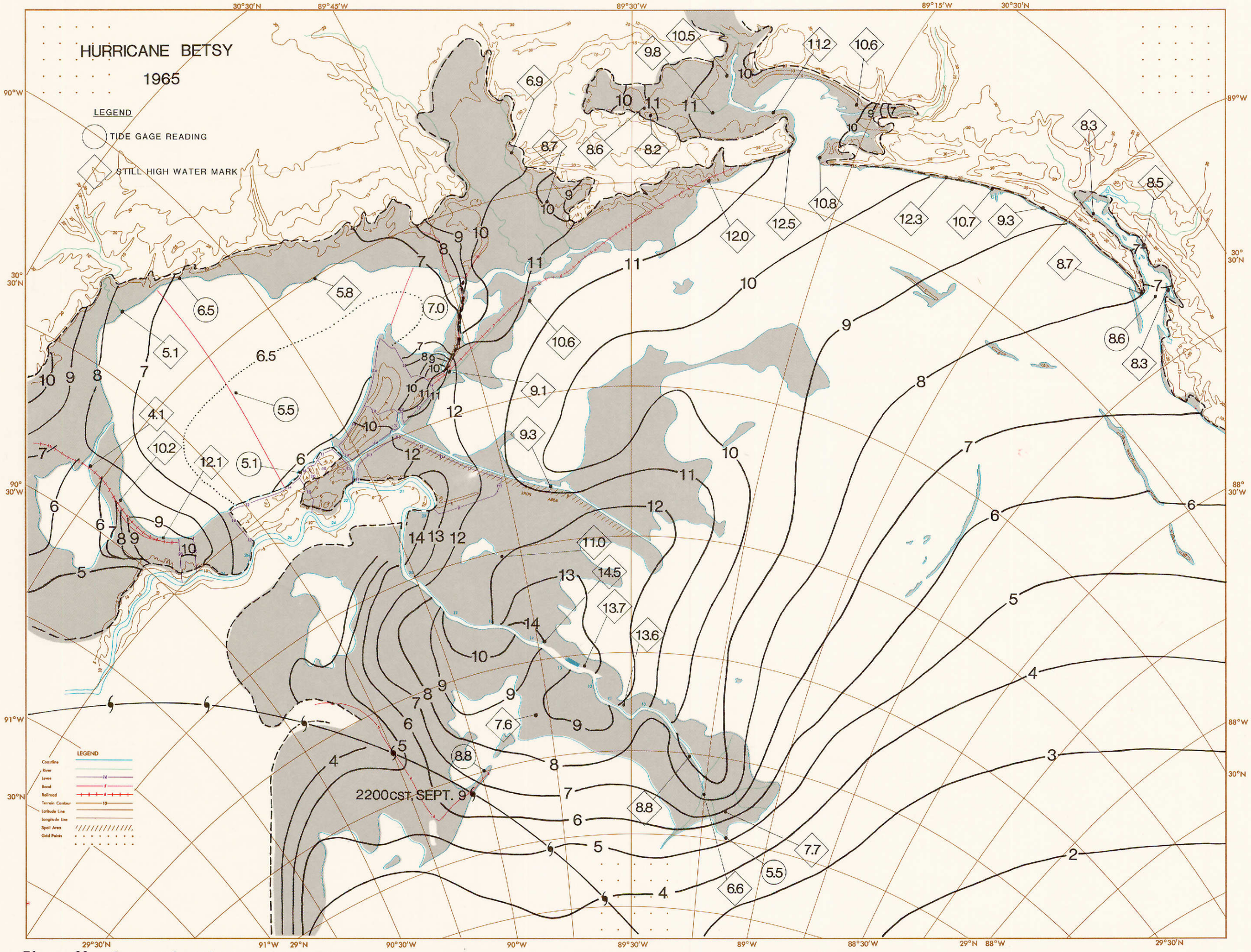

Figure 22. Contoured surface envelope of highest computed surges for Hurricane Betsy, 1965 and the extent of inundation. The contours are hand drawn from Fig. 19 with the overlay, Fig. 20, placed over it. The contours begin and terminate when the surge height reaches the local terrain height. The Shaded area indicates inundation over land. Observed surge heights are also shown for comparision to computed values. Tide and river gage maximum surges are shown within circles; high water mark heights are shown within diamonds.

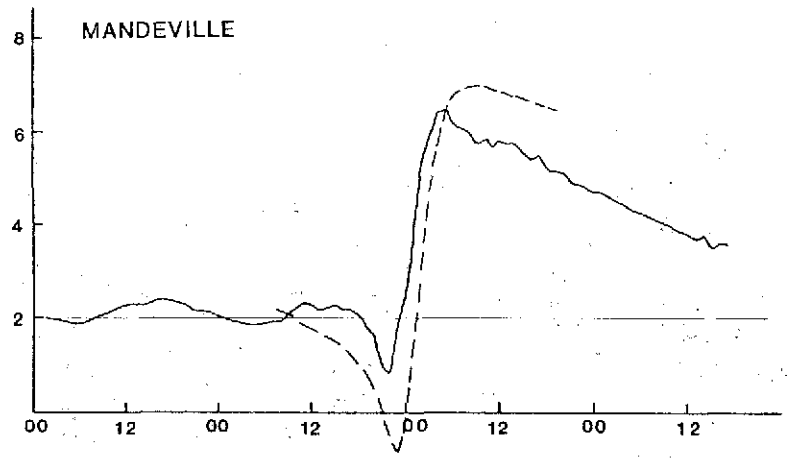

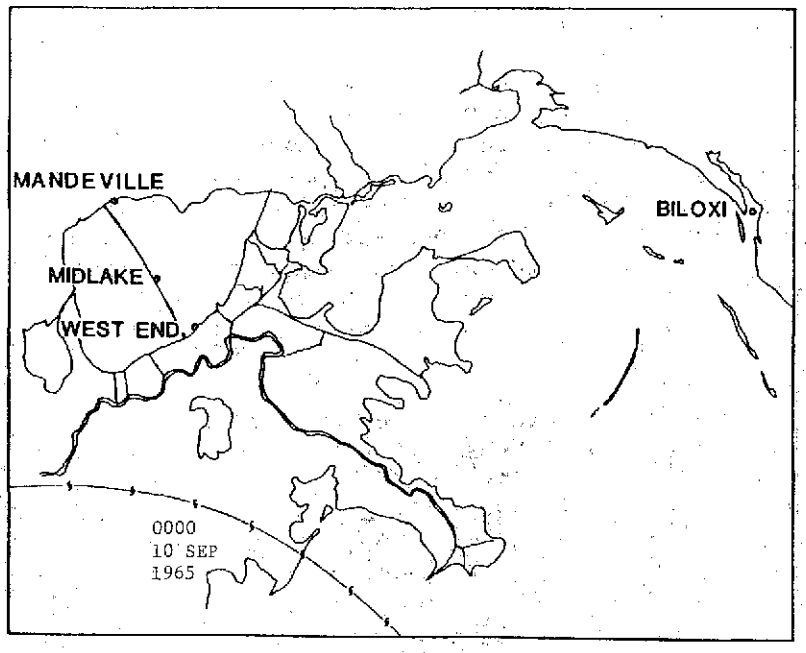

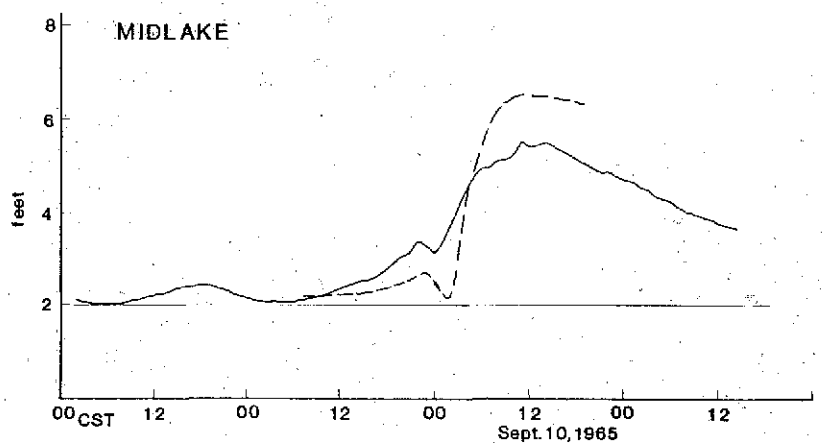

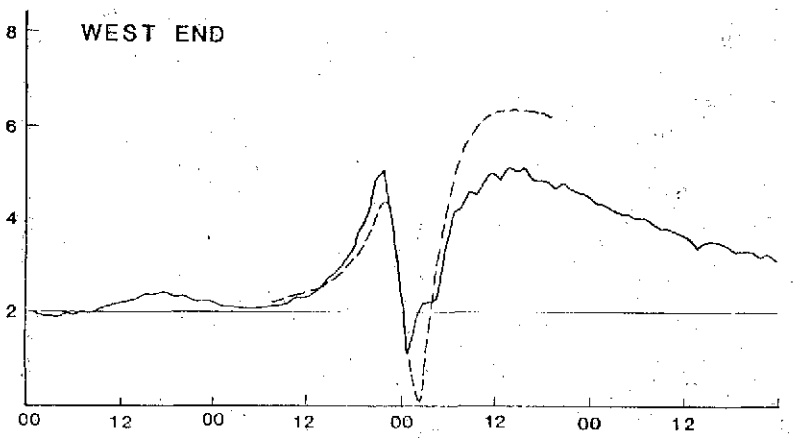

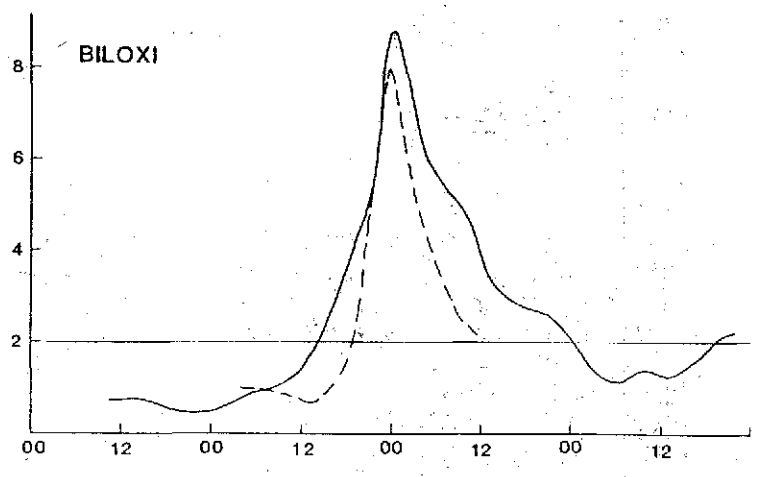

Figure 23. Comparison of observed and computed surge values at four gages for Hurricane Betsy, 1965. Gage locations are shown in the upper right corner of the figure. Observed surges are shown as solid lines; dashed lines are used for the computed surge hydrographs.

Figure 22 displays computed surge contours for the envelope of highest surges. The contours were hand-drawn on an overlay, based on printed output from the SLOSH model, Figs. 19 and 20. The inundated terrain is outlined. Measured high-water marks and maximum gage readings are shown on the envelope for verification. Although results are far from perfect, they do, in general, correspond to observations for the few surge observations over terrain. Landward from the sea the surge drops in some cases and rises in other cases.

The levee elevations for New Orleans in 1965 were supplied by the Corps of Engineers, New Orleans District. For real-time forecasting, present day elevation are used. For such hindcasting runs, historical elevations were used. Empirical computations with present levee elevations imply the Parishes of New Orleans, Citrus and New Orleans East would not be overtopped by Hurricane Betsy assuming, of course, the levees do not break.

Figure 23 compares computed and observed* time-history surges from gage readings (Corps of Engineers, 1965). Notice the initial values in and near Lake Pontchartrain are higher than the Biloxi, Mississippi gage. The computed curves agree qualitatively with the observed, but with amplitude differences. Introduction of rain as a source in the continuity equation and river flow into Lakes Pontchartrain and Borgne does not change the curves significantly. Astronomical tide does have a small effect, especially for flow through passes, but was not included in the model at this time.

Gage observations show a surge wave traveling up the Mississippi River between the two-sided levee system. These are not displayed since this river flow is not within the present province of the surge model.

Hurricane Camille, 1969

Camille was one of the most powerful hurricanes landfalling on the United States. It produced a measured, record surge of over 24 ft on the Mississippi coast. During and after landfall, the storm parameters are not known with sufficient precision to fully verify any surge model. The storm parameters, used as input into the SLOSH model, are illustrated on Fig. 24. The choice of parametric values after landfall is subjective but guided by limited, available data. The track of the storm during landfall was erratic. There was a double eye structure before landfall which coalesced after landfall. The storm was exceptionally small just before, during and immediately after landfall. During the SLOSH model runs, the central pressure held more or less constant over the Gulf of Mexico, but drastically filled immediately after landfall. A track for lowest pressure may have been to the west of St. Louis Bay, Mississippi, but observed radar observations place the hurricane's landfall to the east of the bay.

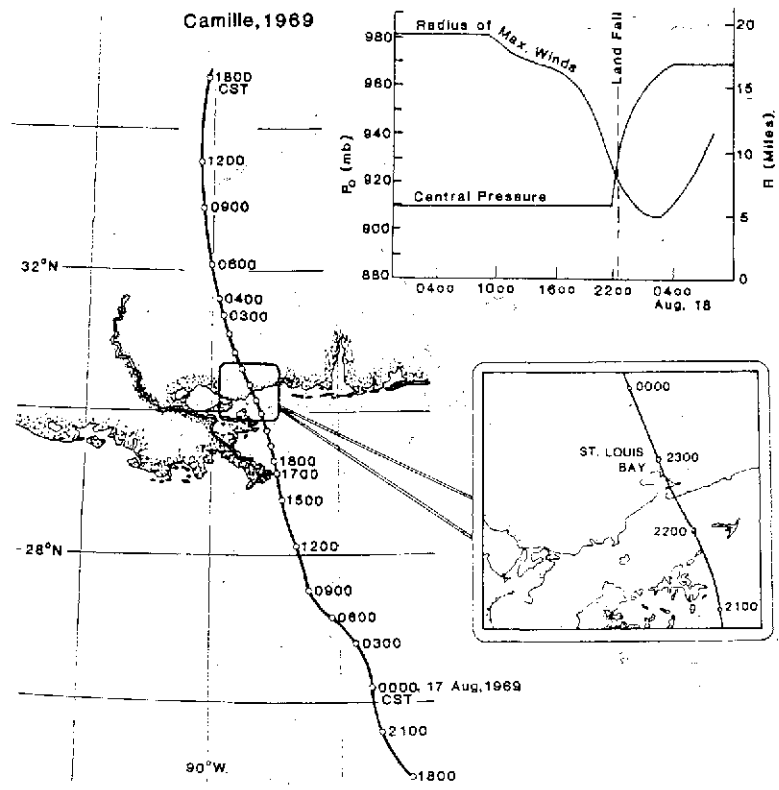

Figure 24. Meteorological input for Hurricane Camille, 1969. The pressure drops and storm sizes are approximated from Fig. 24.

We do not know precisely the rate of filling for central pressure after landfall. Nor do we know the storm's size or track at landfall. Such imprecision presents a major handicap with small sized storms, since small errors in track, storm size and central pressure lead to significant errors in surge generation, especially inside bays. Our choice of storm parameters for Camille was not predicated on a good comparison between computed and observed surges. Instead, we ran the SLOSH program, as users would do, with imprecise meteorological data. Such runs help to alert users of surge models not to expect precise surge comparisons with oversimplified, imprecise meteorological input data. We could, of course, have chosen an alternate set of parameters--well within meteorological accuracy--to give a better comparison of computed and observed surges for Camille.

We chose storm size as a function of time, laying between the double wind maxima of Camille that are shown in Ho et al. (1975). We have experimented with "double eyed" storm parameters yielding two wind maxima. From these formulations we obtained better results. However, it is doubtful that such storm parameters could be forecast with realism. For Camille, we changed the central pressure drastically with time after landfall following Schwerdt, et. al, 1979. Landfall was assumed to the east of St. Louis Bay, Mississippi, based on radar fixes. The computed surge inside the bay is highly sensitive to both landfall point and storm size.

Figure 25 compares the computed surge envelope of highest waters to surge observations for Camille (Corps of Engineers, 1970). Compared to observations, the computed surges to the right of landfall are generally high; to the left, generally low. A shift in storm track to the west would

*The published West End gage observations were corrected by the Corps of Engineers, New Orleans District; personal correspondence.

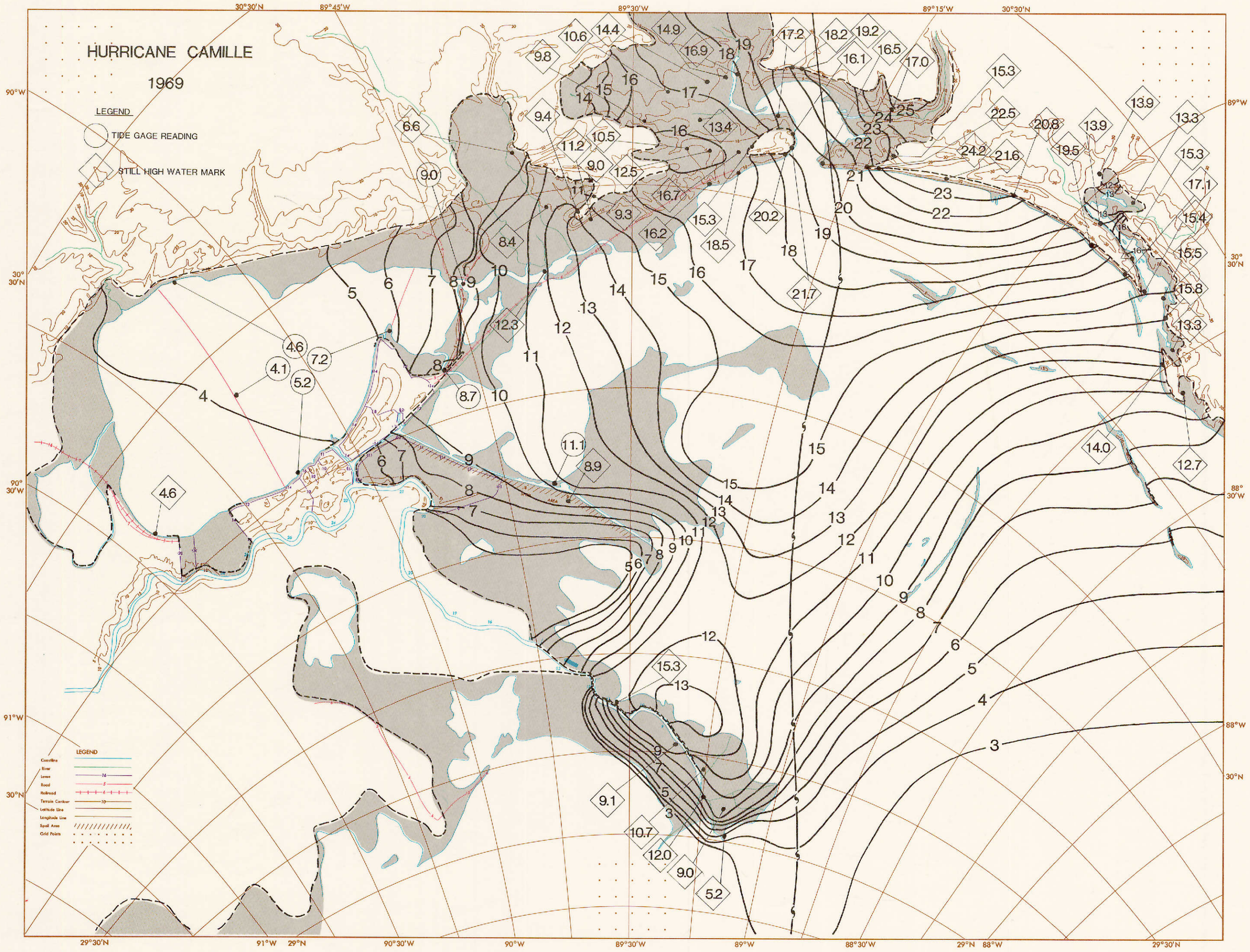

Figure 25. Computed and observed surge heights for Hurricane Camille, 1969, in the Lake Pontchartrain SLOSH basin, similar to Fig. 22.

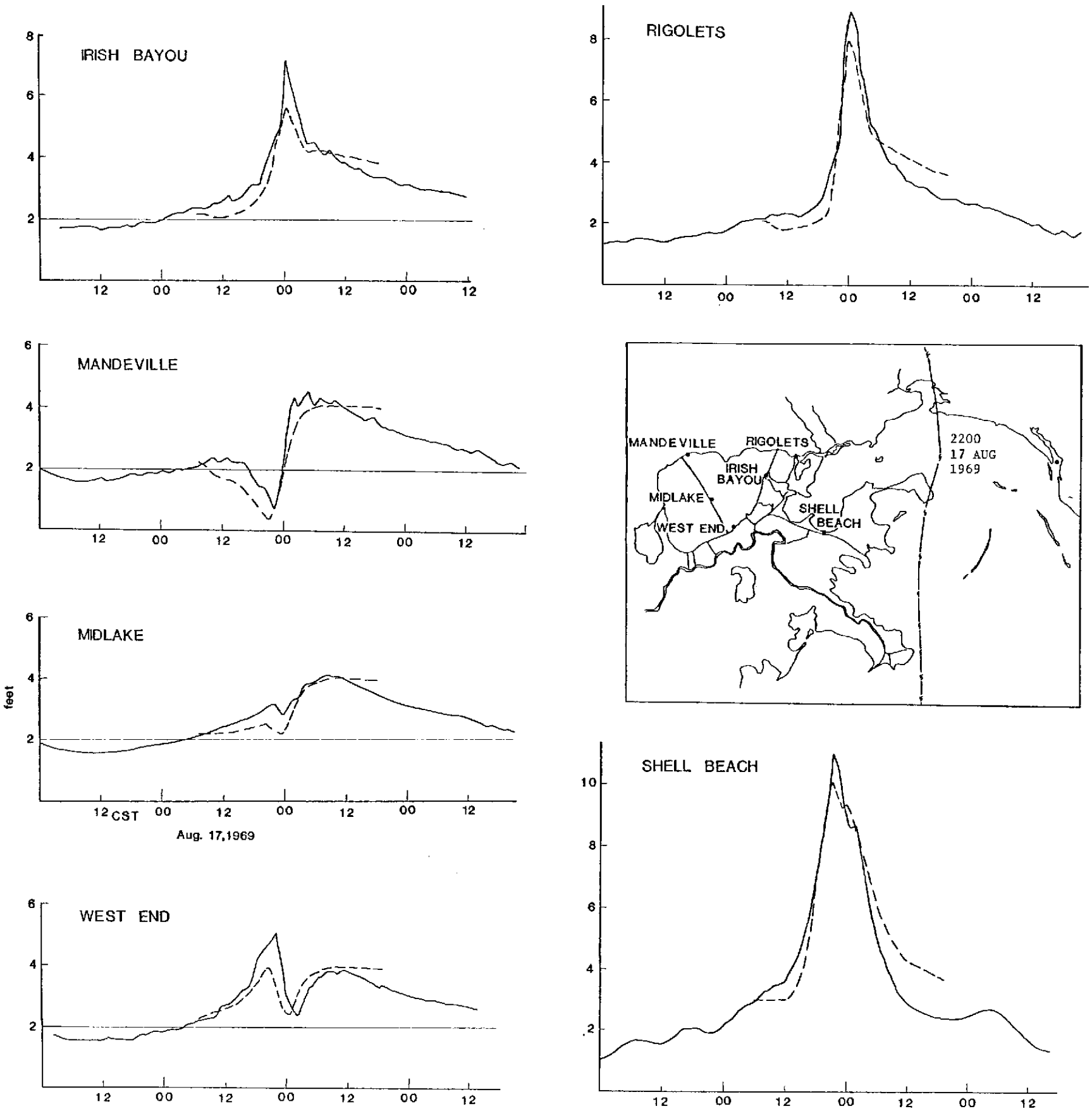

Figure 26. Comparison of observed and computed surge values at six gages for Hurricane Camille, 1969. Gage locations are shown in the center right insert of the figure. Observed surges are shown as solid lines; dashed lines are used for the computed surge hydrographs.

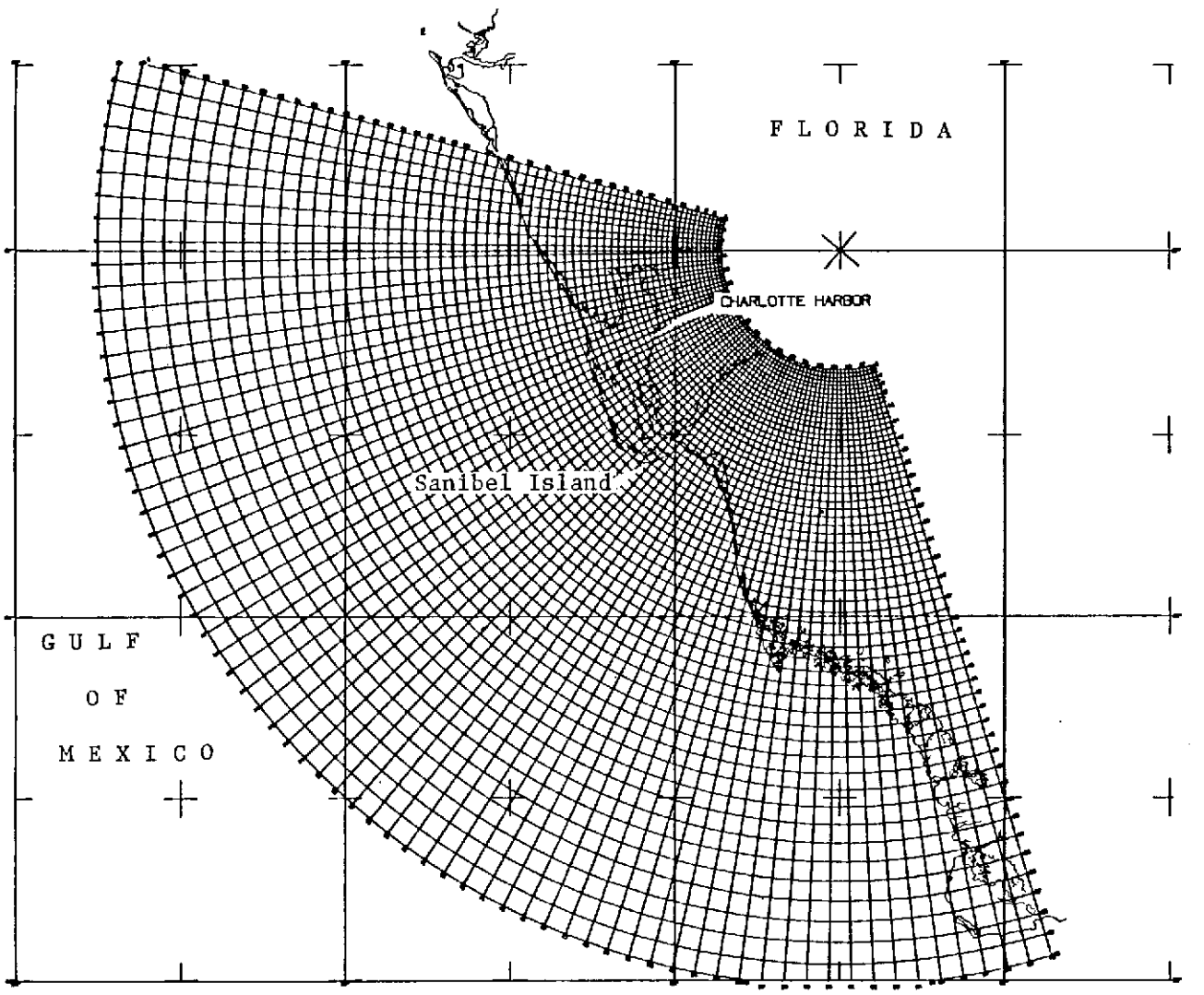

Figure 27. A plane, polar coordinate system (shown in a Mercator projection), tangent to the earth at the eastern tip of Sanibel Island, Florida. The grid encompasses Charlotte Harbor, Florida.

give a better comparison. Similarly, changes in storm size and pressure, and the imposition of a storm model with a double-eye structure or two maxima winds would improve these comparisons. Over and across St. Louis Bay, Mississippi, the computed surges appear overly large. This may result from a fault of the inundation procedures in the SLOSH model or the storm model with small sized storms, from imprecise meteorological input parameters or even from inadequate surge measurements. Throughout the basin, the surge compares well qualitatively with observations. Also, the gradient of observed surges across the basin is qualitatively correct. Only across St. Louis Bay are the amplitudes exceptionally inaccurate. It is worth noting how neighboring surge observations can differ. Such vagaries are a guide for the confidence to be placed on isolated observations.

Figure 26 compares hydrographs of computed surges with gage observations. There is good agreement in a qualitative sense but the amplitudes are off. The amplitudes could be forced into better agreement by altering storm parameters and storm track--well within meteorological accuracy. We make no such adjudication.

Surges over Charlotte Harbor, Florida, Using a Polar Grid

Figure 27 illustrates the geographical placement of the SLOSH polar grid for the Charlotte Harbor, Florida basin. The plane of the grid is tangent to the earth at the eastern tip of Sanibel Island. The grid spacing is 1.5 miles at the tangent point, decreasing to 0.7 miles in the direction of the polar origin and expanding to 4.2 miles in the Gulf.

For convenience, the polar grid is transformed to an image plane with equal grid spacing for printer output. A colored, transparent overlay, Fig. 28, displays various map features for this basin, including inland terrain contours. The overlay is used to orient the user and ascertain the extent of inland flooding.

A definitive comparison of inland inundation along the southwest Florida coast with SLOSH forecast values is difficult. Southwestern Florida's terrain is chaotic and difficult to represent by SLOSH basin data. Much of the coastal area is covered by dense mangroves. The effects of mangroves are incorporated into the SLOSH model by decreasing the stress linearly from the base to the top of mangroves. In addition to having problems with the physical description of the area, documented surge observations are sparse.

Hurricane Donna, 1960

Hurricane Donna, 1960, was a powerful, vacillating storm affecting the southwest Florida coast. It affected the coast and inland terrain south of

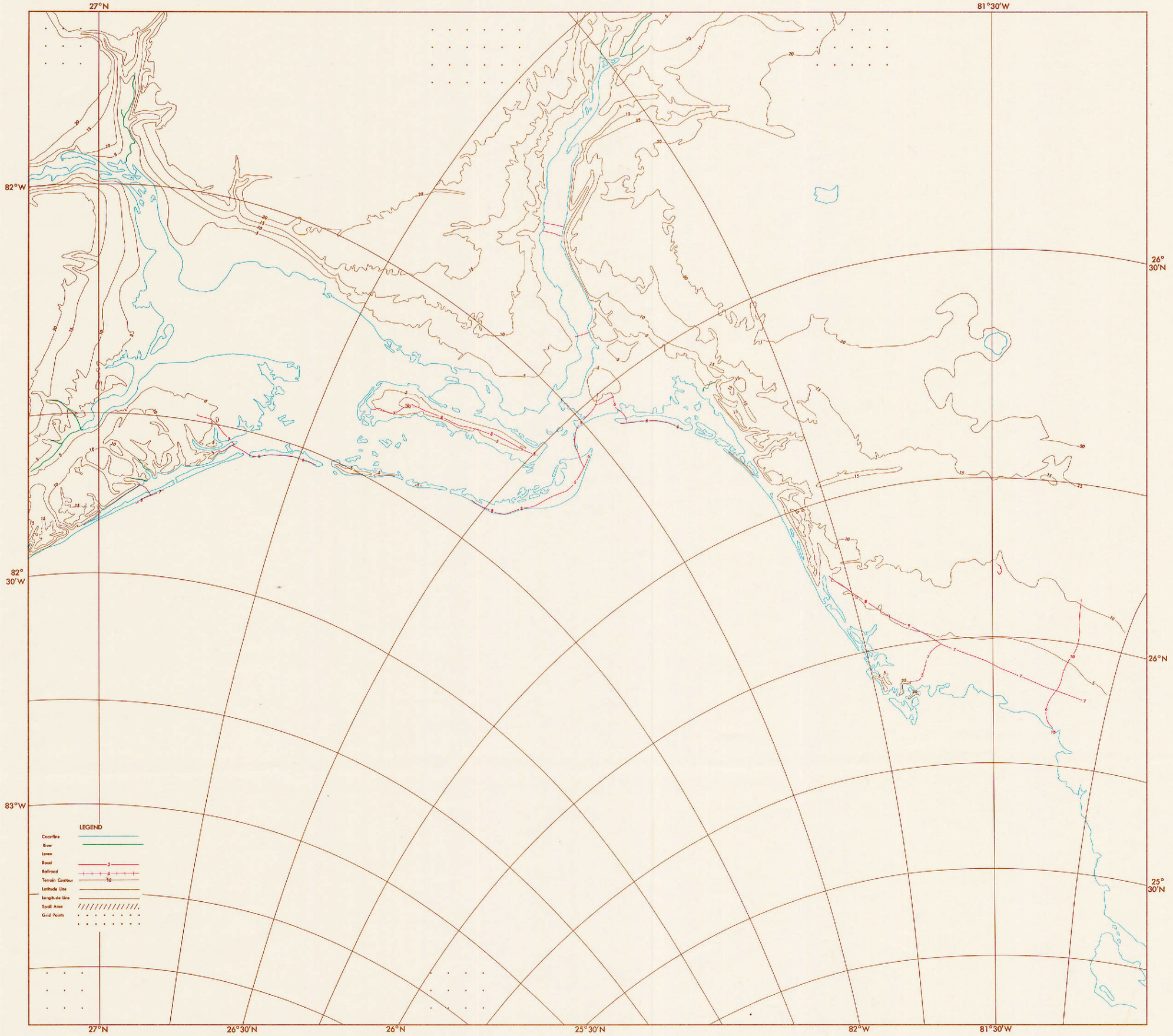

Figure 28. An overlay for the Charlotte Harbor, Florida, SLOSH basin, similar to Fig. 20.

Charlotte Harbor, but not much of the harbor itself.

Figure 29 shows Donna's track (Conover, 1961), along with storm parameters determined by Ho (personal communication). The storm track is a "best-fit" from revised radar fixes. The storm parameters were fleshed out in idealized, continuous form from isolated meteorological observations. The radius of maximum winds was arbitrarily estimated to be 5 miles larger than the optical eye radius. There may well have been significant oscillations of storm motion superimposed on this "best-fit" track. Also, more rapid changes in storm parameters than those illustrated in Fig. 29 may have occurred due to land effects.

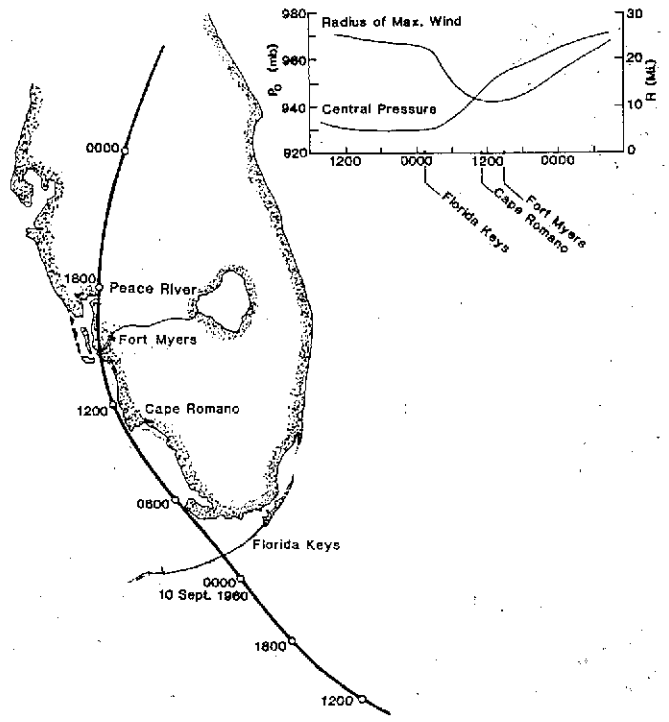

Figure 29. Meteorological input parameters for Hurricane Donna, 1960.

The track was close to, and paralleled, the southwest Florida coast. Storm size varied from small to moderate. Such a situation is demanding of any surge model since small changes in track and storm size give significant changes in surge computations as well as the position of surges. However, such a situation enables a modeler to bias track and storm parameters for an ideal verification. We ran the SLOSH program with the "best-fit" track and storm parameters, in the blind, as users would do with imprecise meteorology, rather than trying to optimize the verification agreement.

Fig. 30 is the surge envelope of highest computed surges for the storm of Fig. 29. The surge contours were drawn on an overlay, laid atop SLOSH surge output. Some high-water marks and one gage reading are shown on the envelope for verification. The verification corresponds in general to observations. Landward from the Gulf, the surge drops in some areas and rises in others. Notice how some neighboring water marks differ. This again is an indication of confidence for isolated observations.

The maximum surge contour of 15 feet*, east of Cape Romano near 26°N, is sensitive to track and storm size. A small track oscillation about the Cape, a change in storm size, or both can drastically change and reposition the computed surge. East of the Cape, the few inland high-water marks are about 2-3 feet lower than the computed values. We can not say definitively whether the computations are too high because of inadequate mangrove treatment, imprecise track and storm parameters, inadequate inundation procedures or the quality of observations. The 6.2 ft measurement east of Cape Romano is about one inch above a concrete apron. Such high water marks are of questionable accuracy and probably do not represent the surge as would a tide gage.

From Cape Romano to 26°20'N, the computed surges are slightly lower than observations. Again, the cause for this disagreement is not known.

The isolated 3.6 foot high-water mark, near the entrance to the Peace River is unexplained by the SLOSH computations.

d. Surges for Galveston Bay, Texas, Using a Polar Grid

Figure 31 shows the placement of the SLOSH polar grid for Galveston Bay, Texas. The plane of the grid is tangent to the earth at the entrance to the bay. The grid spacing is 1.5 miles at the tangent point and decreases to 0.7 miles at the the grid squares nearest the pole point. The grid expands to 3.4 miles in the Gulf of Mexico.

For printer output purposes, the polar grid is transformed onto an image plane with equal grid spacing. A colored transparent overlay, Fig. 32, displays various map features including inland terrain contours. The overlay orientates the user and aids him in delinlating inland flooding when used with SLOSH computer output.

Two deep water passes connecting water bodies are simulated with the following physical specifications:

	mean depth below NGVD	mean width	length
Galveston Channel	30 ft	1250 ft	4.5 mi
Sabine Pass	25 ft	2400 ft	7.5 mi.

Levee systems and their elevations shown in Fig. 32, surrounding Texas City, Texas and Freeport, Texas were assembled from data supplied by the Corps of Engineers, Galveston District. Other basin features and elevations were extracted from NOS marine and storm evacuation charts and from USGS topographic charts.

The terrain northwest of Galveston Bay has been subsiding through the years, and topographic

*The National Hurricane Center later considered inland meteorological data and revised the track of Fig. 27 to lie 3 miles east of Cape Romano with a smaller radius of maximum winds. Computing with the revised track, the maximum surge contour was 12 feet with corresponding changes nearby. Elsewhere, the computed surges were not affected.

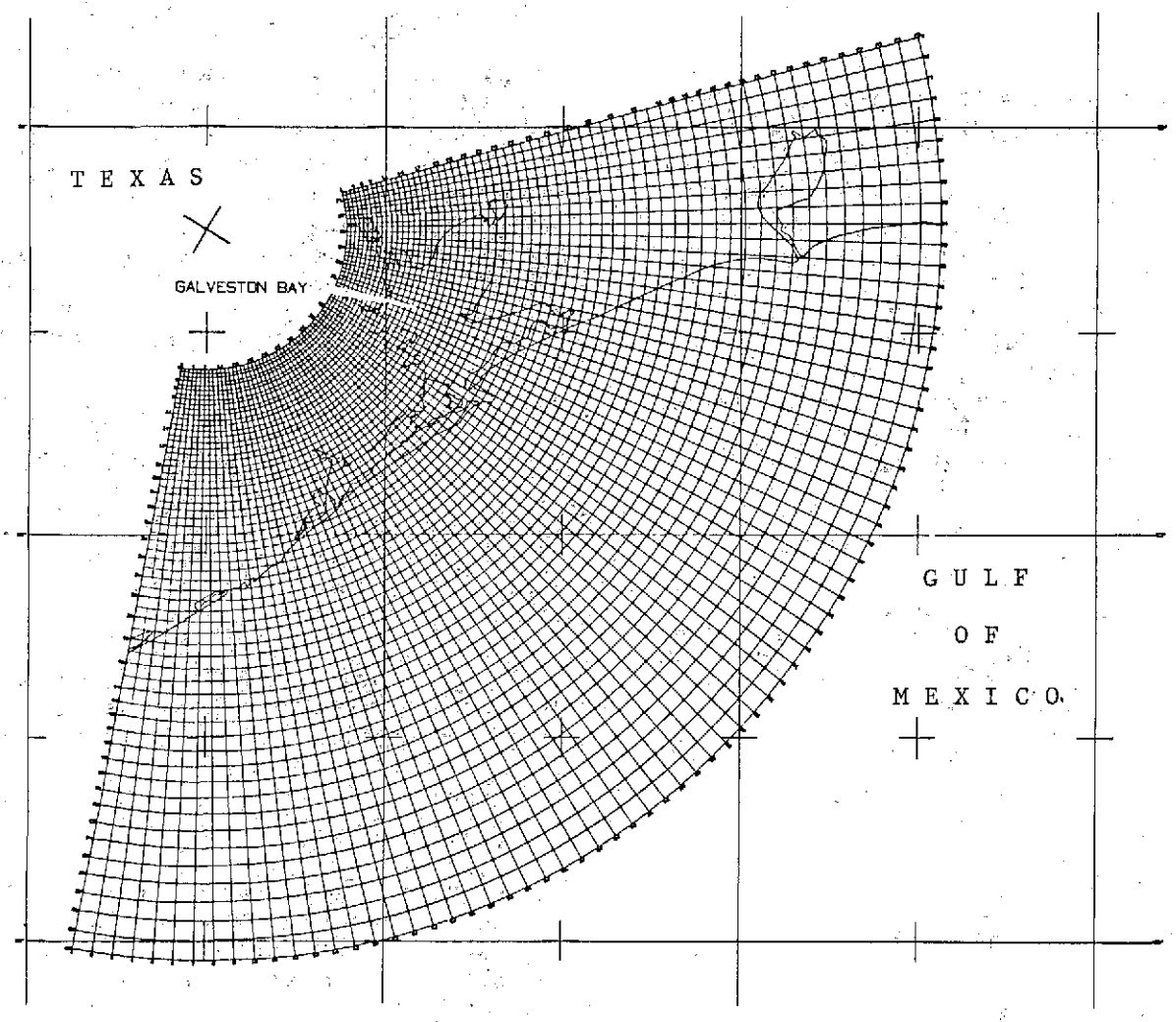

Figure 31. A plane, polar coordinate system for Galveston Bay, Texas depicted on a Mercator chart. The grid is tangent to the earth at the entrance of Galveston, Bay, Texas.

maps, if not corrected by recent surveys, may be seriously in error. For verification runs, the SLOSH terrain elevations and surge observations correspond to the survey nearest to the time of the hurricane. For future operational forecasting, the latest terrain elevations, adjusted for the 1973 survey, are used. Elevations between 1959-1973 have subsided as much as 6 feet northwest of the bay. Topographic maps, adjusted for the 1973 survey, exist for only portions of terrain surrounding the bay. Bathymetry for the bay has not been sounded to correspond to the 1973 survey. Ad-hoc adjustments were made for the operational basin, relative to nearby, measured land subsidence.

Although Freeport and Sabine Lake, Texas are included in the Galveston Bay basin, they are positioned too close to computational boundaries, Fig. 31. Computed results are suspect in such areas. If the storm landfalls in the vicinity of either basin boundary, nearby computed surges are suspect.

The 1949 Hurricane

The 1949 storm made landfall to the west of Galveston Bay near Freeport, Texas. The input track and meteorological parameters are based on Graham and Hudson (1960) surrounding landfall. The remainder of the input track was fleshed out to 72 hours of total track from a gross track analysis (Neumann et al., 1978).

The storm parameters were held constant up to landfall time. After landfall, the storm was subjectively allowed to weaken slightly and decrease in storm size. Small changes in landfall point, storm size, or both, change the computed amplitude and reposition the highest surges inside the bay.

Hand-drawn contours of the highest computed surge for the 1949 storm are displayed in Fig. 33. The inundated terrain is outlined. For verification, measured high-water marks and maximum gage readings* are located on this display. Verification for the computed envelope corresponds qualitatively to observations. Landward from the sea, the computed surge drops in some areas, rises in other areas. Better results, of course, could be obtained by altering the track, storm size, and central pressure of the storm, all within analysis error or accuracy with the available meteorological data. No attempt was made to optimize the storm character within meteorological accuracy for better results. Instead, the program was run in the the same mode as users would do, using imprecise meteorological data.

Hurricane Carla, 1961

Carla was an exceptional storm. It was powerful, large, slow moving and meandering. For several days before and up to landfall, it generated surges along the entire Texas coast and as far

*Personal correspondence, Corps of Engineers, Galveston District.

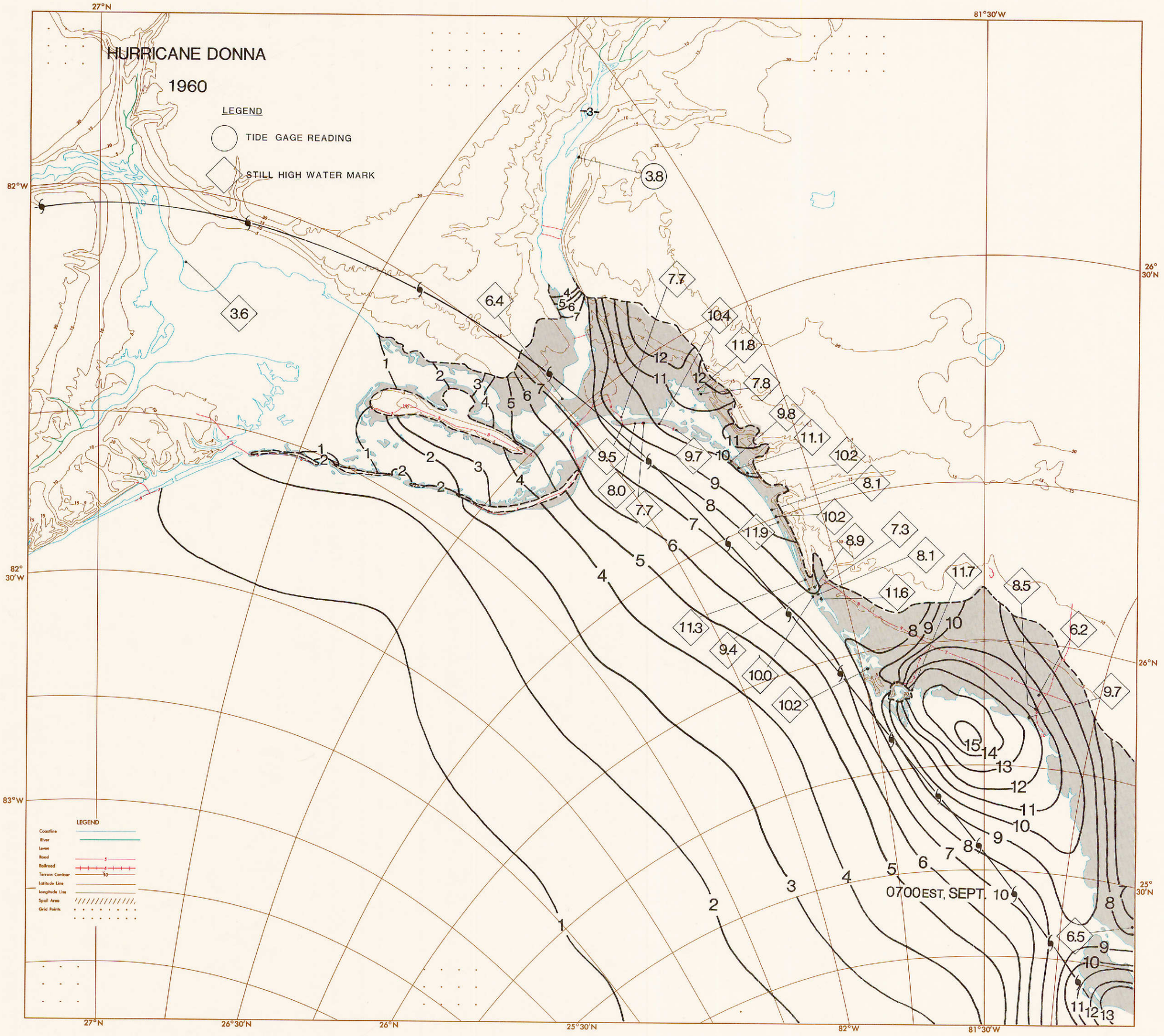

Figure 30. Computed and observed surge heights for Hurricane Donna, 1960, in the Charlotte Harbor SLOSH basin, similar to Fig. 22.

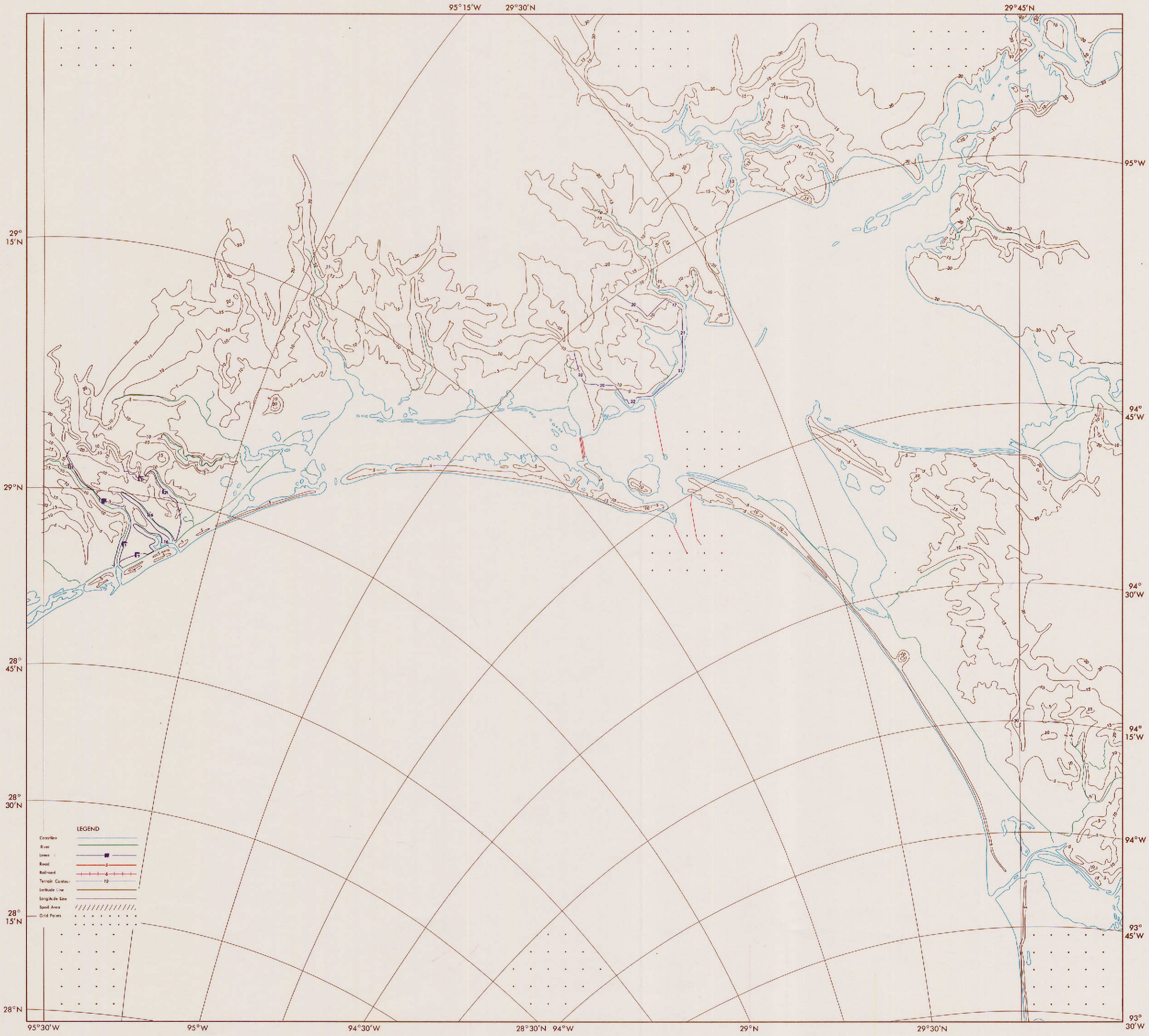

Figure 32. An overlay for the Galveston Bay, Texas, SLOSH basin, similar to Fig. 22.

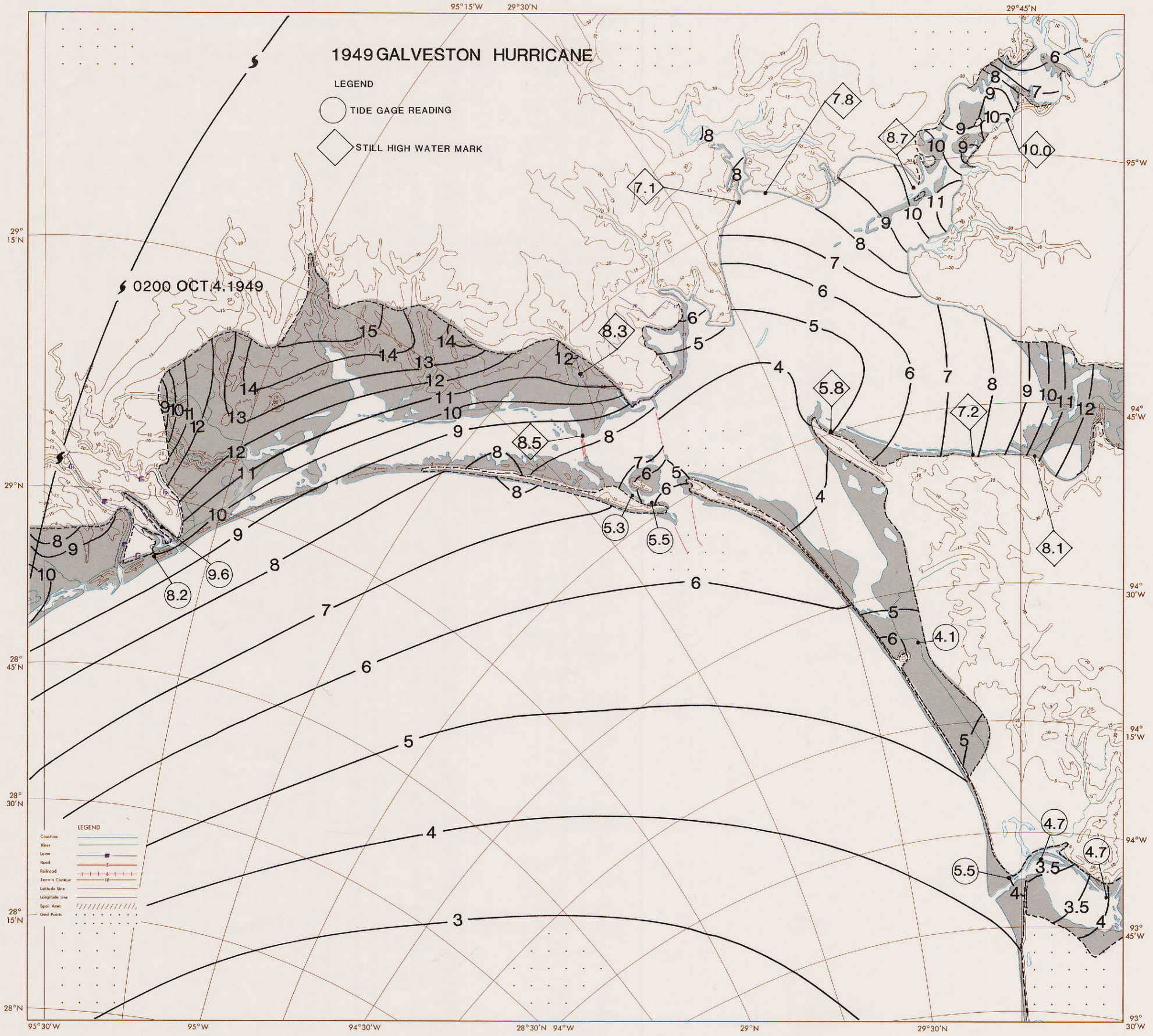

Figure 33. Computed and observed surge heights for the hurricane of 1949 in the Galveston Bay SLOSH basin, similar to Fig. 22.

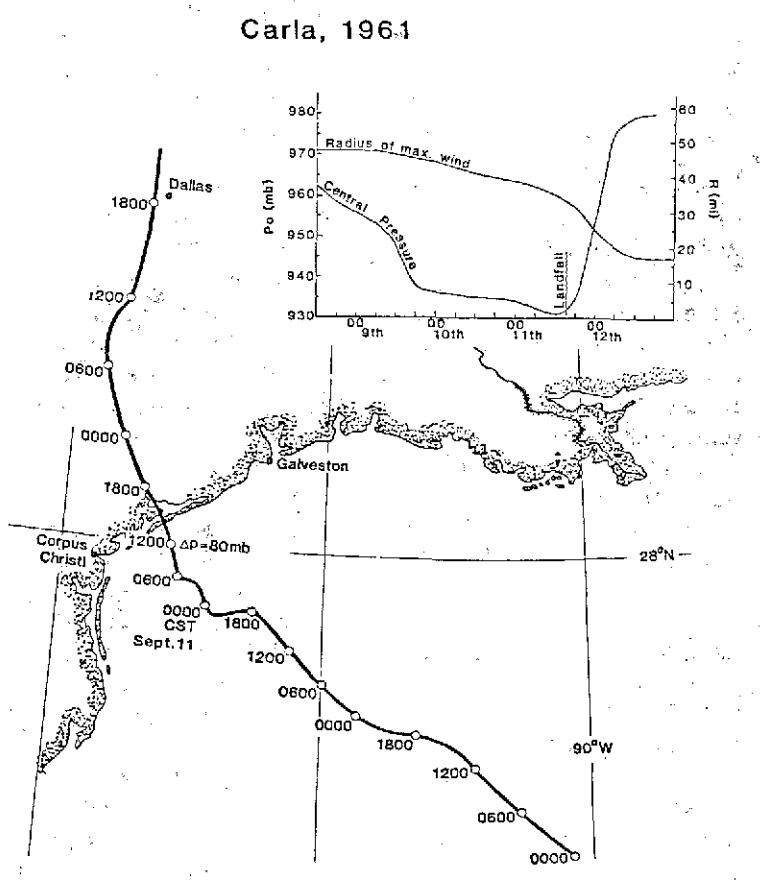

Figure 34. Meteorological input parameters for Hurricane Carla, 1961.

east as the Florida panhandle. No other landfalling storm has affected such a long coastline for such a long period of time.

Carla's track and storm parameters have been analyzed (Ho and Miller, 1982). This work is a special analysis to ascertain an input track, forward storm speed, and input meteorological data varying with time, Fig. 34. The storm moved erratically over the Gulf with an average speed of less than 10 mph. At times, Carla remained nearly stationary. The pressure drop of the storm changed substantially after landfall. The storm size changed substantially before, during, and after landfall. The input track and storm parameters are subjectively smoothed versions of noisy and spatially distributed data. An attempt was made to fit the data for a best landfall position as well as a best-fit track.

The storm did not traverse the interior of the model basin. Instead, it made landfall about 120 miles southwest of the entrance to Galveston Bay. Such a track will not normally generate large surges inside most bays. However, the strength, size, and character of Carla, as well as surge response inside the western Gulf, are unusual exceptions.

The driving forces across the bay are at the periphery of the storm, well away from the storm's core. The storm model was not designed for use in such conditions and may be inadequate there. No storm model is likely to generate adequate driving forces at the periphery of a tropical storm. Background synoptic, driving forces from other meteorological systems overwhelm the wind model results in these areas. At the basin's open boundary nearest to the storm track, the driving forces are stronger than in other regions of the model basin. This is precisely where boundary computations may be inadequate. For verification we did not use 'after-the-event' analyzed wind fields. Hurricane Carla presents an extreme test for any surge model.

Inside the bay, the observed, moderate strength winds varied only slightly in space excluding the near shore regions. Temporal changes were slow preceeding landfall. For such changes, the surges inside the bay are sensitive not only to coastal surges generated at the bay's entrance but also to the gradually varying storm driving forces across the bay. Almost the entire bay was gradually and continuously elevated until landfall, then receded gradually after landfall. For Carla, a long real- time run before landfall is required to generate this significant volume of water inside the bay.

The observed water elevations along the northwest Gulf Coast remained significantly above the monthly mean water level even though the observed winds were weak for several days prior to landfall. Gage readings during other historical storms show the same surge phenomena at Galveston Bay and along the surrounding coast.

Several days before and after the hurricane, water levels were approximately equal to the monthly mean water level. For several days before landfall, water levels slowly rose to levels significantly above the monthly mean. After the storm's passage, water levels slowly receeded to approximately the monthly mean level. Within this tapering period, the water levels were quasi-steady state for long durations. This was especially true along the northwest coast of the Gulf and the corresponding inland water bodies. Generally, the differences above the monthly mean during the tapering periods are not large, but for a large, Carla-type storm, they can exceed 2 feet.

This phenomena can be ascribed to the semi-circular shape of the western Gulf; e.g., the buildup of a quasi-steady, standing wave and water storage when a storm lies in the middle of the Gulf. With a limited area basin having no input boundary values and the surge program run for only a limited time duration, the model cannot readily spin-up to a proper initial state if the monthly mean water level is used as input data.

The SLOSH program automatically initialized the Carla storm 60 hours before landfall. However, a user of the SLOSH model does not know the initialization time when he submits the program. He always inputs observed tide gage values (less astronomical tide) 48 hours before landfall. Usually, the forecaster submits the program 24 hours or less before landfall, and knows the actual track and storm parameters up to submission time. From 48-60 hours before landfall, all tide gages in Galveston Bay and surrounding coasts were reading over 3 feet above NGVD with astronomical tide removed. The change in gage readings during this 12 hour period was small. The monthly mean water elevation about Galveston Bay was 1 to 1.5 feet. To correspond to user's methodology, we chose a 3 foot initial water height above NGVD for input across the entire model basin. The entire basin was assumed to be 3 feet above NGVD at

initialization time; no data are available to verify this assumption.

Despite the many possible objections to Carla's SLOSH simulation within the Galveston Bay basin, the SLOSH model computes some useful surge values, Fig. 35 and 36. The computed surges are all low for September 12. This may be due in part to an inadequacy of the storm wind model. The wind model treats the storm as a series of steady state conditions with time. Just before and after landfall (1400 CST, 11 Sept), the storm's core continually decreased in intensity and size with time. The model storm assumes changes occur simultaneously throughout the entire storm. It is doubtful if changes at the storm's core are reflected immediately at the storm's periphery. The storm's landfall point is outside the model basin; Galveston Bay is located on the periphery of the storm.

The observed surge records (72 hours) have residual oscillations due to astronomical tide. However, the dual peaks during September 11 may be due to the storm's stalling motions in the Gulf of Mexico. Astronomical tide is not set in the model. For NOS gages, the predicted astronomical tide, with a range of about one foot, was subtracted from the gage readings. For other gages, the astronomical tide remains in the record.

Gage records on rivers or along intracoastal waterways offer special opportunities for verification. Rivers are portrayed coarsely in the SLOSH model at this time, without details about the width of the river's channel or its depth. This is true also for waterways. In particular, at Hi-Island, the waterway is treated as dry terrain until the arrival of inland inundation from the sea. Here, the computed surge results from inland inundation, not waterway flow.

The Brazoria and Texas City gages are located on a river and canal, both extending inside an area bounded on both sides by a levee system. The gages are located at the head of the river and canal. Since inundation did not overtop the two-sided levees of the river and canal, the computed surges at the entrance to the river and canal are compared with the observed surge at the head of the river and canal. Surge levels may be higher at the heads than at the entrances. The entrance to Brazoria is located on the river basin on dry terrain, just in front of the encompassing levee system of Freeport, Texas.

Inside the Houston ship channel, the computed surge at Baytown is too low*. The peak surge occurred after storm landfall, when the periphery of the storm model may be inadequate. Also, the gage may reflect an imprecise datum due to the strongly subsiding terrain in the region. The high water marks, Fig. 35, in this region may be contaminated by this same lack of a reference datum.

e. Overall SLOSH Accuracy

Observed storm surge heights were compared in Fig. 37 to SLOSH computed values for historical storms in nine different basins. A total of 570 surge observations were included in this figure. These observations were taken throughout areas affected by the surge--around inland water bodies and over flooded inland terrain. Weak storms with insignificant surge potential were not considered so as not to compromise verification of the significant surges.

Before a SLOSH simulation with a historical storm is performed, the storm's track is determined as precisely as possible. Published "best fit" tracks are frequently insufficiently accurate to pinpoint a hurricane's track and landfall position. Even though a meticulous study of available meteorological data will often leave ambiguities in the actual storm position, this best analyzed track is used. In addition to the storm's track, an estimate is made, as precisely as the data allow, for the hurricane's radius of maximum wind and central pressure as functions of time.

Only hurricanes with adequate observational data describing the storm's meteorological parameters and the resulting storm surges are used for verification purposes. Tide gage observations are inherently more accurate than are high water marks. High water marks are best when they are taken within a building which acts as a tide gage's stilling well. The building then damps out wave action. Unfortunately, most structures will over or underdamp the water level. Often a dense cluster of high water marks within a few residential blocks vary by more than +/-20%. Note also that the tide gage data in Fig. 36 is limited to lower observed values. Tide gages frequently top out or fail during a major surge event. Only high water marks remain to describe the upper values. Verification using tide gage data only will generally not capture the significant, higher surges.

Verification with high water marks along the Atlantic seaboard is complicated due to the large tidal amplitude. Generally, the time of highest surge is unknown, resulting in the tides being unknown at that time. Since astronomical tides have a small range along the Gulf of Mexico and inside Pamlico Sound, storms there were chosen to avoid severe tidal contamination of verifying high water marks or surge heights. Astronomical tide was removed from the tide gage observations whenever tidal predictions were available. The level of error for computed storm surge heights

---

*A special run, allowing crests of monochromatic wind waves to overtop barriers was attempted. The height of the wind waves (surf) along barriers was assumed 50% of the coastal surges. That is, surge and crest height 1.5 the surge height with surge and trough 0.5 the surge height. Only those portions of the wind waves between barrier and crest height were allowed to overtop barriers. The conditions for wave overtopping are surge below barrier, or else surge plus trough above barrier. The periodic, pulsating, sheet flow across coastal barriers from wind wave, computed by elementary means, increased the surge envelope in the bay about 1/2 foot on the average and about 3/4 foot in the ship channel. For ordinary storms with much shorter residence time in the basin, the envelope changes were much smaller. At this stage of model development, overtopping of barriers by wind waves is not considered.

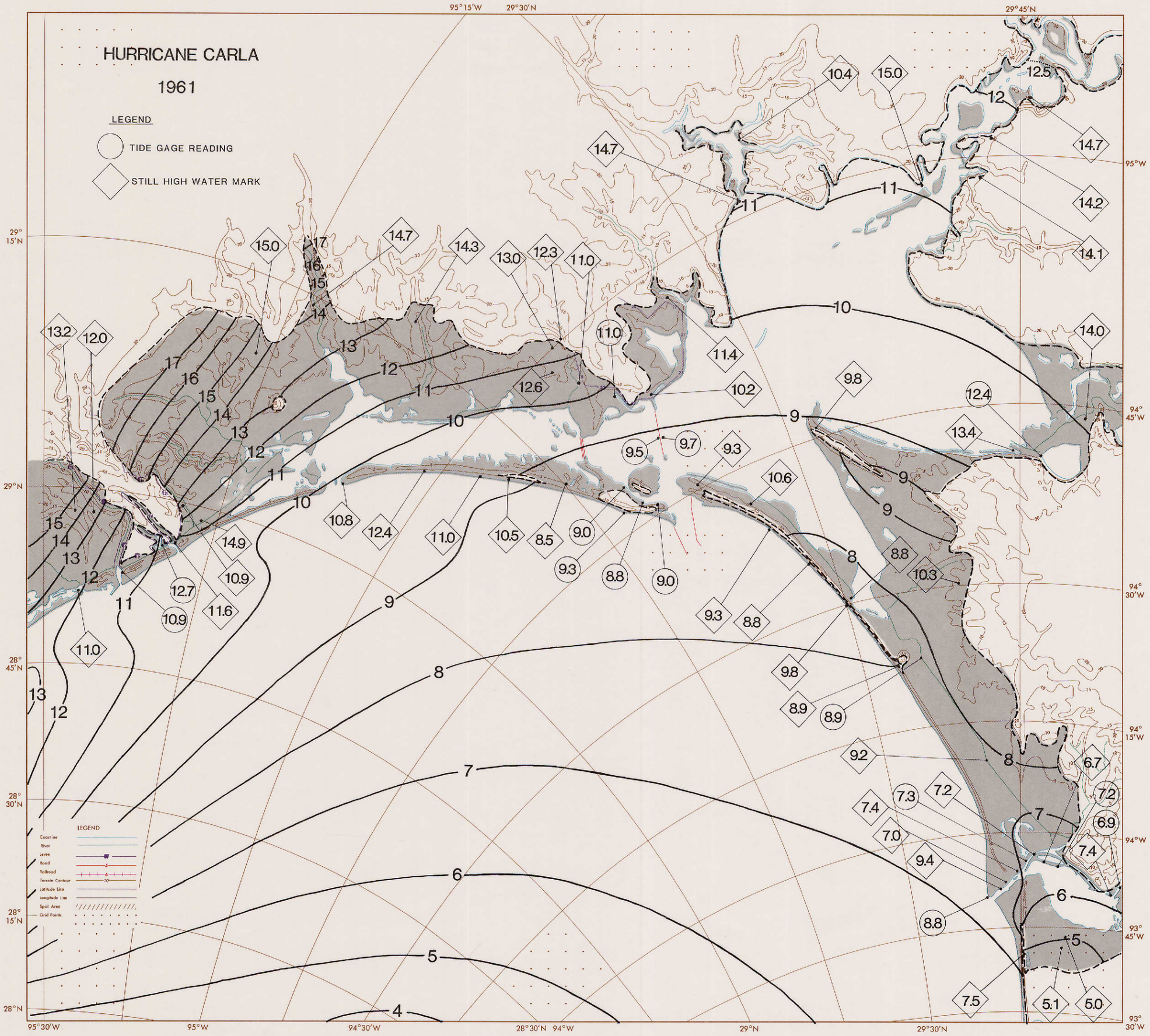

Figure 35. Computed and observed surge heights for Hurricane Carla, 1961 in the Galveston Bay SLOSH basin, similar to Fig. 22.

GALVESTON BAY BASIN

HURRICANE CARLA

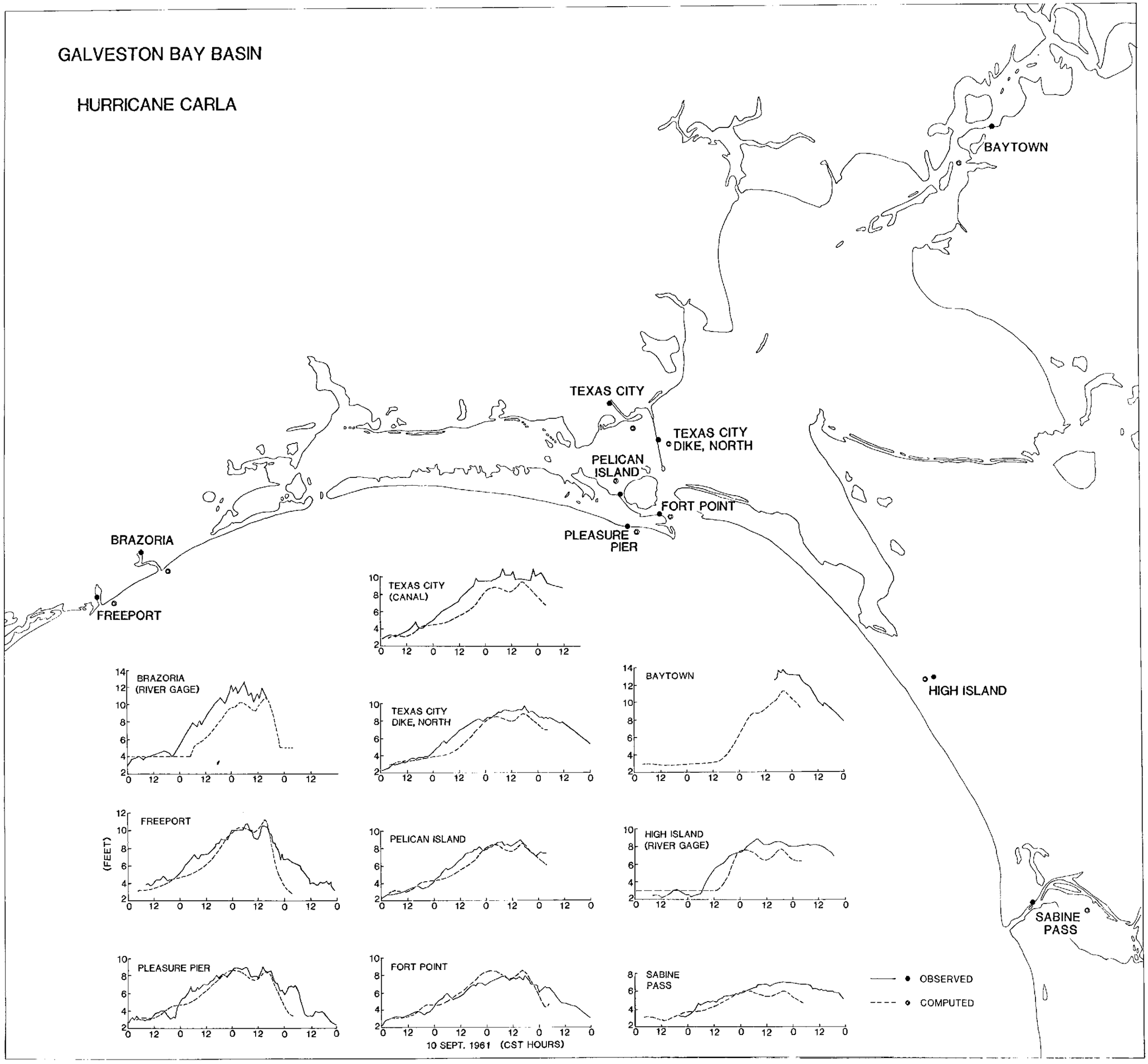

Figure 36. Comparison of observed and computed surge values for Hurricane Carla, 1961. Gage sites are located along the Texas coast. Observed surges are shown as solid lines; dashed lines are used for the computed surge hydrographs.

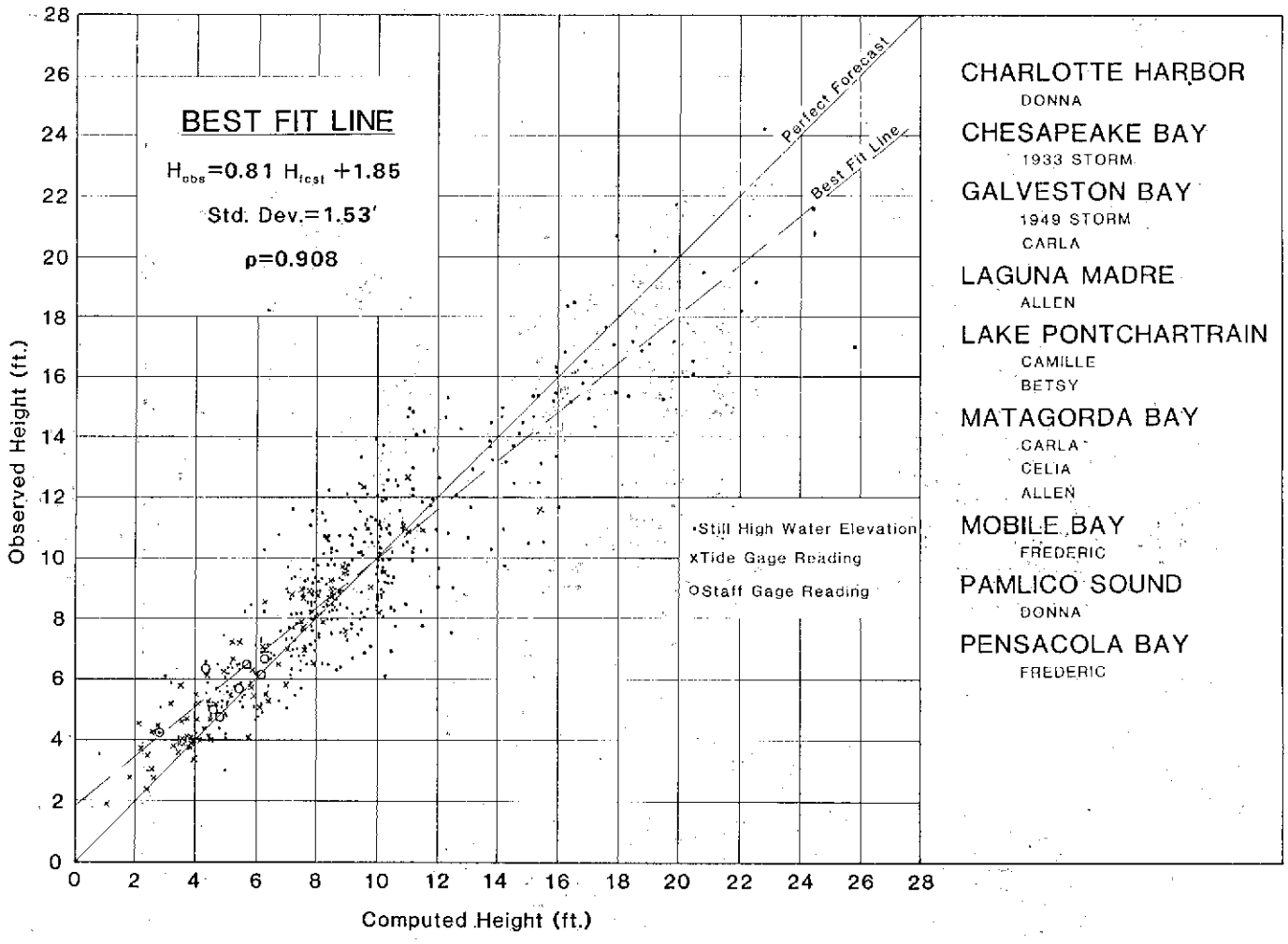

Figure 37. Observed surge heights versus surge heights forecast by the SLOSH model for nine storms in nine basins. A total of 570 tide gage, staff gage, and high water mark observations are shown with the corresponding SLOSH forecast. Generally, the model is within ± 20% for significant surge heights.

depicted by Fig. 37 is generally within ± 20% for the significant surges. A few observations fall outside that range. For "real-time" surge forecasting, these errors can increase significantly due to imprecise storm tracks and storm parameters.

All verifications in this report are for independent data, without "tuning" for particular storms in particular basins. Since "universal" specifications are used for model coefficients such as drag and bottom stress, SLOSH may be adapted to any geographical location for useful surge computations, provided adequate bathymetric and terrain data are available.

Figure 38 depicts geographically the 27 currently operational SLOSH basins, including the nine basins used in Fig. 37. The remaining 13 basins were each verified with at least one storm event against tide gage observations, with astronomical tide removed; high water marks were also used for verification if they were minimally affected by astronomical tide. The accuracy of these additional verifications were comparable to Fig. 37.

ACKNOWLEDGMENT

We are grateful and appreciative to Dr. Albion Taylor for his many suggestions, hours of conversations, and review of the manuscript. His many contributions greatly accelerated the SLOSH program. In particular, he designed the software to plot the polar grid on an X-Y plotter to fit any map projection and any scale. We also appreciate his suggested approach to smoothing which resulted in Appendix C.

Lastly, we wish to express our thanks to Amikam J. Gilad for his elegant illustrations and to Belinda F. Howard and Karen Yip for typing many versions of the manuscript.

REFERENCES

Bodine, B. R. 1971: Storm surge on the open coast: Fundamentals and simplified prediction. Corps of Engineers Technical Memorandum No. 35, U.S. Army Coastal Engineering Research Center, U.S. Department of Defense, 65 pp.

Chow, V. T., 1959: Open Channel Hydralics. McGraw-Hill Book Co. Inc., 680 pp.

Conover, L. F., 1961: Evaluation of the eye fixes obtained by radar for hurricane Donna, September 1960. National Hurricane Research Project Report No. 50, U.S. Department of Commerce, 85-100.

Corps of Engineers, 1950: Project CW-167, Waves and wind tides in inland waters, Lake Okeechobee, Florida. Project Bulletin No. 2, U.S. Army Office of the District Engineer, Jacksonville, Florida, U.S. Department of Defense, 109 pp.

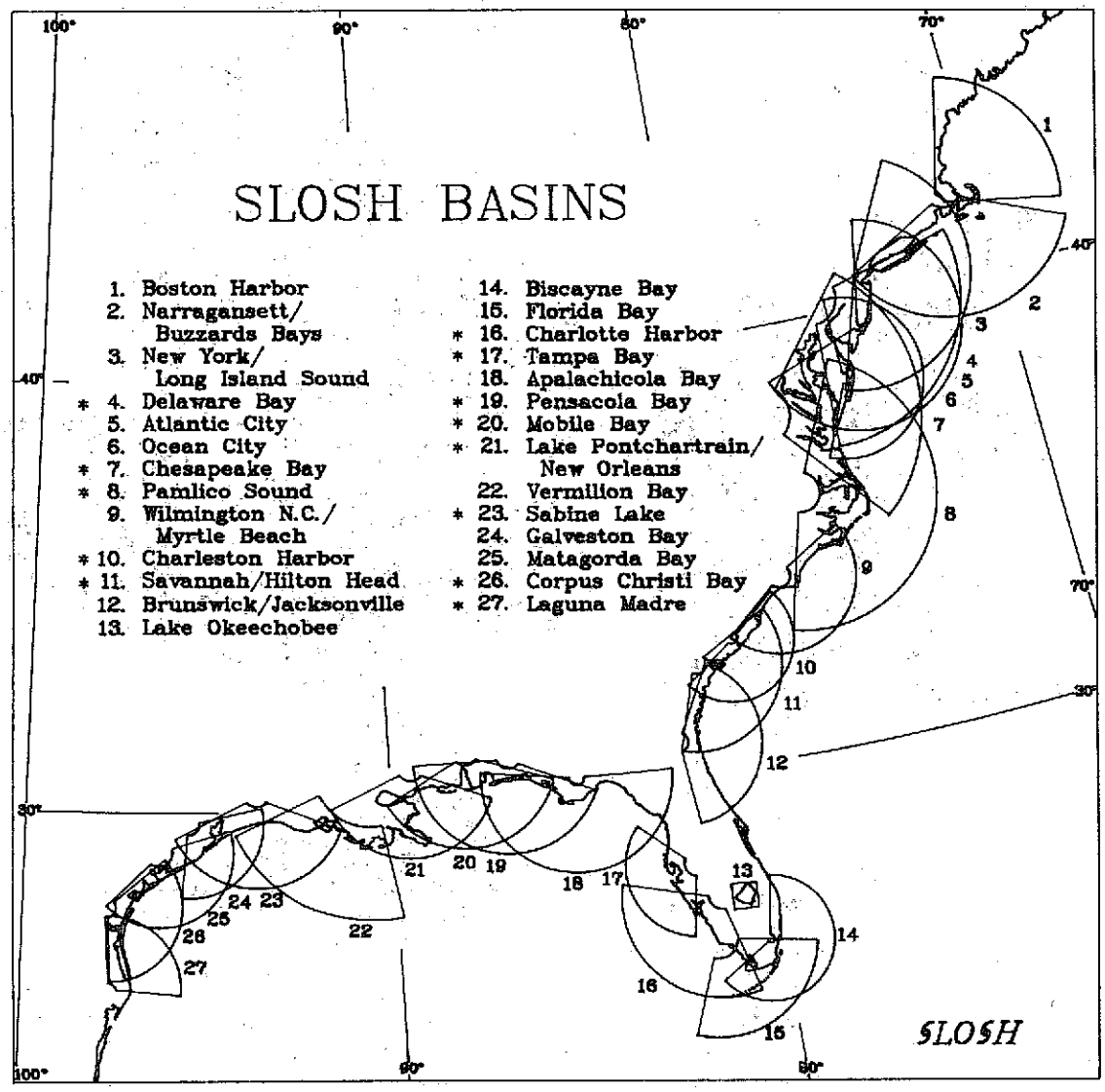

Figure 38. SLOSH basins along the Gulf of Mexico and Atlantic coastlines of the U.S.

_____, 1961: Report on Hurricane Carla in the U.S. Army Engineer District, Galveston. U.S. Army, U.S. Department of Defense, 29 pp.

_____, 1965: Report on Hurricane Betsy 8-11 September 1965 in the U.S. Army Engineer District, New Orleans. U.S. Army, U.S. Department of Defense, 48 pp.

_____, 1970: Report on Hurricane Camille 14-22 August 1969. U.S. Army, U.S. Department of Defense, 220 pp.

Crawford, Kenneth C., 1979: Hurricane surge potentials over Southeast Louisiana as revealed by a storm-surge forecast model: A preliminary study. Bulletin of American Meteorological Society, Vol. 60, No. 5, 422-429.

Graham, H. E. and G. N. Hudson, 1960: Surface winds near the center of hurricanes (and other cyclones). National Hurricane Research Project Report No. 39, U.S. Department of Commerce, 200 pp.

Ho, F. P. and J. F. Miller, 1982: Pertinent meteorological and hurricane tide data for Hurricane Carla. NOAA Technical Report NWS 32, National Oceanic and Atmospheric Administration, U.S. Department of Commerce, 111 pp.

Ho, F. P., R. W. Schwerdt, and H. V. Goodyear, 1975: Some climatological characteristics of hurricanes and tropical storms, Gulf and East Coasts of the U.S. NOAA Technical Report NWS 15, National Oceanic and Atmospheric Administration, U.S. Department of Commerce, 87 pp.

Jelesnianski, C. P., 1967: Numerical computation of storms surges with bottom stress. Mon. Wea. Rev., 95, 740-756.

_____, 1972: SPLASH (Special program to list amplitudes of surges from hurricanes): I. Landfall storms. NOAA Technical Memorandum NWS TDL-46, National Oceanic and Atmospheric Administration, U.S. Department of Commerce, 33 pp.

_____, and A. D. Taylor, 1973: A preliminary view of storm surges before and after storm modifications. NOAA Technical Memorandum ERL WMPO-3, National Oceanic and Atmospheric Administration, U.S. Department of Commerce, 33 pp.

Mesinger, F., and A. Arakawa, 1976: Numerical methods used in atmospheric models, Global Atmospheric Research Programme, WMO-ICSU Joint Organizing Committee, GARP Publication Series, No. 17, 64 pp.

Myers, V. A., and W. Malkin, 1961: Some properties of hurricane wind fields as deduced from trajectories. National Hurricane Research Project Report No. 49, National Oceanic and Atmospheric Administration, U.S. Department of Commerce, 43 pp.

National Weather Service, 1978: Tropical storm surge forecast for Lake Okeechobee, Florida. NWS Technical Procedures Bulletin No. 242, National Oceanic and Atmospheric Administration, U.S. Department of Commerce, 10 pp.

Neumann, C. J., G. W. Cry, E. L. Caso, and B. R. Jarvinen, 1985: Tropical cyclones of the North Atlantic Ocean, 1871-1980 (with storm track maps updated through 1984). U.S. Government Printing Office, Washington, D.C., 174 pp.

Platzman, G. W., 1963: The dynamical prediction of wind tides on Lake Erie. Meteorological Monographs, Amer. Meteor. Soc., 4, 44 pp.

Reid, R. O., and B. R. Bodin, 1968: Numerical model for storms surges in Galveston Bay. Journal of the Waterways and Harbors Division, ASCE, 94, WW1, Proc. Paper 5805, 33-57.

Schwerdt, R. W., F. P. Ho, and R. R. Watkins, 1979: Meteorological criteria for standard project hurricane and probable maximum hurricane winds, Gulf and East Coasts of U.S. NOAA Technical Report NWS 23, National Oceanic and Atmospheric Administration, U.S. Department of Commerce, 275 pp.

Wanstrath, J. J., R. E. Whitaker, R. O. Reid, and A. C. Vastano, 1976: Storm surge simulation in transformed coordinates, Vol. 1, Theory and application. Corps of Engineers Technical Report No. 76-3, U.S. Army Coastal Engineering Research Center, U.S. Department of Defense, 166 pp.

Weather Bureau, 1951: Analysis of winds over Lake Okeechobee during tropical storms of August 26-27, 1949. Hydrometeorological Report No. 26, U.S. Department of Commerce, 80 pp.

Welander, P., 1961: Numerical prediction of storm surges, Advances in Geophysics, Vol. 8, Academic Press, 315-379.

Witaker, R. E., R. O. Reid, and A. C. Vastano, 1975: An analysis of drag coefficient at hurricane windspeeds from a numerical simulation of dynamical water level changes in Lake Okeechobee, Florida. Corps of Engineers Technical Report No. 56, U.S. Army Coastal Engineering Research Center, U.S. Department of Defense, 103 pp.

APPENDIX A

Equations of Motion

The SPLASH equations of motion in linear form Platzman (1963) and Jelesnianski (1967) are revised for the finite-amplitude effect when depths are small. This occurs for inland inundation, especially as it begins and ends. Figure A1 illustrates the total depth (D+h), where h is the height of the surface above the reference datum, D is the depth measured from the bottom surface to datum, and z' is a vertical height variable, positive above the datum. This variable is primed in anticipation of later re-scaling. The left side of the figure is for an ocean or sea; the right side shows the variables over land.

The complex form of the momentum equation with the hydrostatic approximation, but with no advective terms and no horizontal viscosity, can be written following Welander (1961) as

$$\frac{\partial w}{\partial t'} = q - ifw + \nu\frac{\partial^2 w}{\partial z'^2} \qquad (A1)$$

where

$$w = u + iv \ , \ q = -g\left[\frac{\partial(h-h_0)}{\partial x} + i\frac{\partial(h-h_0)}{\partial y}\right]$$

u,v = horizontal components of current
h_o = hydrostatic height from surface pressure field
ν = eddy viscosity coefficient (assumed to be constant)
f = Coriolis parameter
g = gravity
t' = time (primed in anticipation of later re-scaling)
z' = vertical coordinate

Equation (A1) is not in transport form. To eliminate the presence of h when integrating from a basin's bottom to the surface, the following transformation is used

$$z = \frac{D + z'}{D + h}, \quad t = t' \ ; \ z = z(z',t';x,y)$$

$$dz = \frac{dz'}{D + h} - \frac{D + z'}{(D + h)^2}\frac{\partial h}{\partial t'}dt' \ , \ dt' = dt \qquad (A2)$$

or

$$dz' = (D + h)dz - z\frac{\partial h}{\partial t}dt \ , \ dt' = dt \qquad (A3)$$

also,

$$\frac{\partial}{\partial t'} = \frac{\partial z}{\partial t'}\frac{\partial}{\partial z} + \frac{\partial t}{\partial t'}\frac{\partial}{\partial t} = -\frac{z}{D+h}\frac{\partial h}{\partial t'}\frac{\partial}{\partial z} + \frac{\partial}{\partial t}$$

$$\frac{\partial}{\partial z'} = \frac{\partial z}{\partial z'}\frac{\partial}{\partial z} + \frac{\partial t}{\partial z'}\frac{\partial}{\partial t} = \frac{1}{D+h}\frac{\partial}{\partial z} \qquad (A4)$$

but

$$\frac{\partial h}{\partial t'} = \frac{\partial z}{\partial t'}\frac{\partial h}{\partial z} + \frac{\partial t}{\partial t'}\frac{\partial h}{\partial t} = \frac{\partial h}{\partial t} \ , \qquad (A5)$$

because h is independent of z and z'.

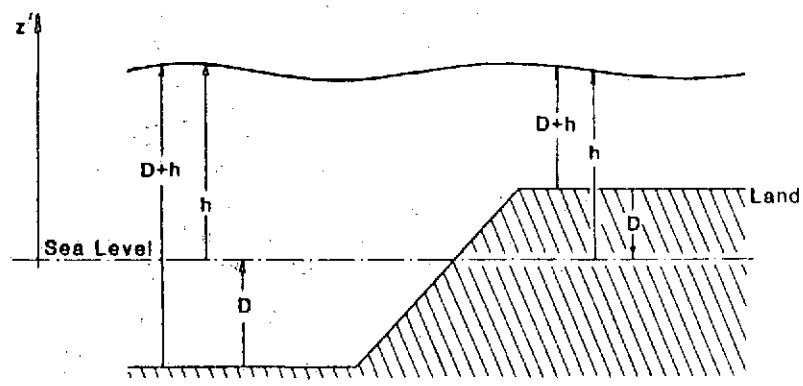

Figure A1. Water levels above terrain and sea bottom relative to a datum.

Applying (A4) and (A5) on (A1) gives

$$\frac{\partial w}{\partial t} - \frac{z}{D+h}\frac{\partial h}{\partial t}\frac{\partial w}{\partial z} = q - ifw + \frac{\nu}{(D+h)^2}\frac{\partial^2 w}{\partial z^2} \qquad (A6)$$

The second term on the left hand side is assumed to be of the same order as the advective terms and hence is ignored, Equation (A6) can then be written as

$$\frac{\partial^2 w}{\partial z^2} - \sigma^2 w = -\eta_\nu^{-1} q, \qquad (A7)$$

$$\sigma^2 = \eta_\nu^{-1}\left(if + \frac{\partial}{\partial t}\right), \ \eta_\nu = \frac{\nu}{(D+h)^2}$$

for $0<z<1$. The operator σ^2 operates on w, and specifically does not operate on z and η_ν. The separate term in σ^2, in general, do not commute. Since the hydrostatic assumption is used, vertical velocity can be neglected and the terms then do commute. Henceforth, it will be understood that σ^2 will not operate on z or η_ν. Following (Platzman, 1963), (A7) is formally solved as

$$w = (\sinh z\sigma)A + (\cosh z\sigma)B + (\eta_\nu\sigma^2)^{-1}q \qquad (A8)$$

To solve for A and B, the following boundary conditions from Jelesnianski (1967) are assumed

$$\nu\frac{\partial w}{\partial z'}\Big|_{z'=-D} = sw\Big|_{z'=-D} \ , \qquad (A9)$$

$$\nu\frac{\partial w}{\partial z'}\Big|_{z'=h} = R$$

or

$$\frac{\nu}{D+h}\frac{\partial w}{\partial z}\Big|_{z=0} = sw\Big|_{z=0} \ , \quad \frac{\nu}{D+h}\frac{\partial w}{\partial z}\Big|_{z=1} = R$$

where

s = slip coefficient,

$R = x_\tau + iy_\tau$, x_τ, y_τ surface stress components

Taking the derivative of (A8) w/r to z, and noting

$\partial\eta_\nu/\partial z = 0$, then

$$\sigma^{-1}\frac{\partial w}{\partial z} = (\cosh z\sigma)A + (\sinh z\sigma)B \qquad (A10)$$

at $z = 0$, using (A9)

$$\sigma A = s[\eta_\nu(D+h)]^{-1}w\Big|_{z=0} \qquad (A11)$$

at $z = 1$, using (A9)

$$\sigma B = \frac{1}{\eta_\nu(D+h)}[(\operatorname{csch}\sigma)R - s(\coth\sigma)w\Big|_{z=0}] \qquad (A12)$$

then from (A8)

$$(D+h)\sigma^2 w = \frac{1}{\eta_\nu}[s\sigma(\sinh z\sigma)w\Big|_{z=0} + \sigma(\cosh z\sigma)\{(\operatorname{csch}\sigma)R - s(\coth\sigma)w\Big|_{z=0}\} + Q] \qquad (A13)$$

where $Q = (D+h)q$. It is assumed σ does not operate on $(D+h)$.

Let

$$M = \int_{-D}^{h} w\,dz' = (D+h)\int_0^1 w\,dz \qquad (A14)$$

From (A7)

$$(D+h)\left[\int_0^1 \frac{\partial^2 w}{\partial z^2}\,dz - \sigma^2\int_0^1 w\,dz\right] = -\eta_\nu^{-1}(D+h)q\int_0^1 dz \qquad (A15)$$

or

$$\eta_\nu(D+h)\frac{\partial w}{\partial z}\Big|_0^1 - \eta_\nu\sigma^2 M = -Q \qquad (A16)$$

and from (A9)

$$\eta_\nu\sigma^2 M = Q + R - sw\Big|_{z=0} \qquad (A17)$$

Solving (A13) for $w\,|_{z=0}$, substituting into (A17), and separating the σ operator from Q, gives

$$\eta_\nu[\sigma^2 + G(\sigma)]M = Q + [1 + H(\sigma)]R \qquad (A18)$$

where

$$G(\sigma) = \frac{\sigma^2}{[\nu\sigma^2/s(D+h)] + \sigma\coth\sigma - 1}$$
$$H(\sigma) = \frac{1 - \sigma\operatorname{csch}\sigma}{[\nu\sigma^2/s(D+h)] + \sigma\coth\sigma - 1} \qquad (A19)$$

This is the same form given by Jelesnianski (1967) except that the total depth (D+h) replaces D. If the operator (A19) is expanded formally as a Taylor's series about $\sigma_0^2 = if(D+h)^2/\nu$, then

$$G(\sigma) \simeq G_0(\sigma_0) + \frac{(D+h)^2}{\nu}G_1(\sigma_0)\frac{\partial}{\partial t}$$
$$H(\sigma) \simeq H_0(\sigma_0) + \frac{(D+h)^2}{\nu}H_1(\sigma_0)\frac{\partial}{\partial t} \qquad (A20)$$

is a simple approximation for (A19). Plugging (A20) into (A18) gives

$$\frac{\partial M}{\partial t} = -ifAM + BQ + (C + \frac{J}{if}\frac{\partial}{\partial t})R \qquad (A21)$$

where

$$A = \frac{1 + \sigma_0^{-2}G_0}{1 + G_1}\,,\quad B = \frac{1}{1 + G_1}\,,$$
$$C = \frac{1 + H_0}{1 + G_1}\,,\quad J = \frac{\sigma_0^{\,2}H_1}{1 + G_1} \qquad (A22)$$

By dropping the J term, (Jelesnianski, 1967), the real and imaginary parts of (A22) yield the momentum equations

$$\frac{\partial U}{\partial t} = -g(D+h)\left[B_r\frac{\partial(h-h_o)}{\partial x} - B_i\frac{\partial(h-h_o)}{\partial y}\right] + f(A_rV + A_iU) + C_rx_\tau - C_iy_\tau$$
$$\frac{\partial V}{\partial t} = -g(D+h)\left[B_r\frac{\partial(h-h_o)}{\partial y} + B_i\frac{\partial(h-h_o)}{\partial x}\right] - f(A_rU - A_iV) + C_ry_\tau + C_ix_\tau \qquad (A23)$$

where

M = U + iV = complex form of transport

These are the same momentum equations developed by Platzman (1963) and modified by a slip coefficient (Jelesnianski, 1967), except that the total depth (D+h) replaces D, and the six coefficients $A_r,\ldots,C_i$ are functions of the total depth (D+h).

If (A23) were linearized over land and (D+h) replaced by D, the equations are no longer hyperbolic. However, over the ocean areas, D is always positive and the equations remain hyperbolic.

APPENDIX B

Advective and Coriolis Terms

Storm surge is not sensitive to advective terms in the equations of motion, except in localized areas with strong flow gradients. Usually, such localized areas are fixed in space because of geographical constraints. At localized points of a basin, specialized computations can then be used, such as classical hydraulic techniques, for highly non-linear flow. Accordingly, the advective terms in the storm surge equations of motion are generally ignored. A question then is the importance of the Coriolis terms.

From dimensional analysis, the advective and Coriolis terms can be compared. This involves the Rossby number, $R = U/(L\Omega)$, where U is a typical speed such as flow current, L is a typical length, and Ω is the angular velocity of the earth's rotation. Sometimes the length is taken as the depth of the sea. Then, if R is small (deep water) the Coriolis terms dominate. Because shelf models are generally deep, this is one basis for keeping the Coriolis terms and discarding the advective terms. For bay models where depths may be shallow, the Coriolis terms are sometimes discarded and the advective terms may or may not be discarded.

Sometimes, it is more appropriate to consider horizontal length scales in the Rossby number because the advective terms involve horizontal interaction. These would be wave length in the open sea, bay diameter, caustic distance of trapped waves, etc. For deep water in the open sea the wave length is $L = \sqrt{gD}\,T$, where D is depth and T period. A typical velocity for a shallow water wave of amplitude A is $U = gAT/L$. The Rossby number is then

$$R = \frac{gAT}{L^2\Omega} = \frac{A}{DT\Omega} \tag{B1}$$

If non-linearities are weak, then the period "T" of the wave will be relatively unchanged from one region to another. Comparing R in deep and shallow water is not a simple procedure because the amplitude, A, increases, or shoals, in shallow water. Advective terms may then have some importance in shallow coastal waters where A increases and D decreases.

Suppose the diameter of a circular bay, L_B, is smaller than the wavelength. Then

$$R = \frac{gAT}{L_B^2\Omega} = \frac{A}{DT\Omega}\,\frac{DgT^2}{L_B^2} \tag{B2}$$

where $D/L_B < L_B/(gT^2)$. Thus, Rossby numbers may be high in bays not merely because of shallow depths and shoaling, but also because it may not be wide enough to contain a natural wave length for the period dealt with. For odd shaped basins the Rossby number varies from one part of the basin to another. The amplitude in a bay is with respect to a datum that is changing with time due to storage of water from the sea. If inland inundation takes place, then L_B can be large and the Coriolis terms will dominate.

Rossby numbers give a broad overview of the importance of the advective and Coriolis terms. They are not a substitute for empirical testing of models, with and without the advective and Coriolis terms. Because of large transient variations of A and L_B and spatial changes in D, the Coriolis terms are retained in the SLOSH model, throughout deep and shallow waters of an input basin.

APPENDIX C

Smoothing

The SLOSH model deals with moving, irregular land boundaries and sub-grid features such as barriers, narrow passes, and channels. Two-grid-interval noise frequently results and appears in the computed surge field near such complications. Such noise is non-physical. It is desirable to remove or suppress it whenever it grows significantly in magnitude.

Conventional smoothing procedures are useful at interior grid cells of a domain (i.e., at least one grid point away from a boundary) with some form of cyclical boundary condition for completion. The domain in our application has complex, non-cyclical, time-dependent, boundary conditions. Hence, smoothing must be extended up to the boundary to conserve mass, an essential property near coastal boundaries where high surges occur.

In our basins, simple and constant geometry relating the domain for smoothing does not exist. Each grid cell must be examined against surrounding grid cell conditions. After smoothing, the water should not move across barriers which have not yet been submerged by flooding. We also want to avoid smoothing over thin sheets of water across corrugated terrain. The smoothing discussed here applies only to two dimensional flow.

For the smoothing procedure, we introduce the following notation. Let $h_{i,j}$ be the water level of a cell before smoothing, $\bar{h}_{i,j}$ after smoothing, and (i,j) the center cell surrounded by neighbor cells, Fig. C1.

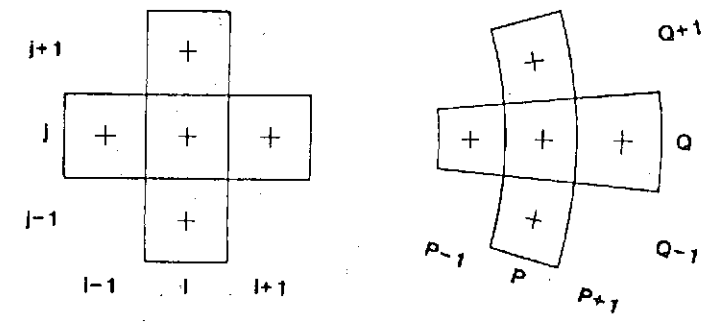

Figure C1. Center cell and neighbor cells for Catesian and polar grid systems.

A smoothing formula in mass flux form for a Cartesian grid of constant cell area is,

$$\bar{h}_{i,j} = h_{i,j} + \sum_{k=1}^{4} F_k \tag{C1}$$

where

$$F_k = -\,\delta_k\alpha_k(h_{i,j} - h_k)$$

h_k is one of the neighboring cells, $h_{i\pm1,j\pm1}$.

Here F_k represents the mass flux across side k. If no flux is allowed (such as through a barrier), then F_k is switched off by setting $\delta_k = 0$, otherwise $\delta_k = 1$. α_k is an assigned weight. If we consider the case of interior grid cells, unimpeded by any barriers, then $\delta_k = 1$ for all four sides. By choosing $\alpha_k = 1/8$, then (C1) is reduced to

$$\bar{h}_{i,j} = \tfrac{1}{2}h_{i,j} + \tfrac{1}{8}(h_{i+1,j} + h_{i-1,j} + h_{i,j+1} + h_{i,j-1}) \tag{C2}$$

or in operator form,

$$\bar{h}_{i,j} = \frac{1}{8}\begin{vmatrix} 0 & 1 & 0 \\ 1 & 4 & 1 \\ 0 & 1 & 0 \end{vmatrix} h_{i,j} \qquad (C3)$$

a conventional five point smoother for Cartesian grids. Sometimes, however, we wish to set $F_k = 0$ in (C1). This occurs when

1. a barrier exists between contiguous cells. That is, a barrier is higher than either $h_{i,j}$ or h_k,
2. when cell h_k has water less than 1 foot over terrain,

or 3. one dimensional flow is active between $h_{i,j}$ and h_k.

In these situations no mass is allowed to pass in to the center cell or out from adjacent cells. For Cartesian grids, (C1) can be re-written in a more direct form for computer use as,

$$\bar{h}_{i,j} = \frac{1}{2}h_{i,j} + \frac{1}{8}\sum_{k=1}^{4}[\delta_k h_k + (1-\delta_k)h_{i,j}] \ . \qquad (C4)$$

The result is to increase the center cell weight by 1/8 whenever $\delta_k = 0$, in equivalence with (C1). In such cases, smoothing at (i,j) does not depend on the ignored h_k cell.

For the polar grid, Fig. C1, smoothing is not as clear cut and some analysis is required. Empirical tests show that the following simplified approach, while incomplete, serves our purposes for the SLOSH model.

Consider the polar (P,Q)* cell through a side of the cell according to the height difference between adjoining cells. The following two properties are to be satisfied:

1. a constant field must be smoothed to the same constant.
2. mass moved into a cell by a height difference moves out of an adjoining cell so as to conserve mass.

From the first property, (C1) can be written as,

$$\bar{h}_{P,Q} = h_{P,Q} + \alpha^{+}_{P,Q}(h_{P,Q+1}-h_{P,Q}) + \alpha^{-}_{P,Q}(h_{P,Q-1}-h_{P,Q}) \qquad (C5)$$

$$+ \beta^{+}_{P,Q}(h_{P+1,Q}-h_{P,Q}) + \beta^{-}_{P,Q}(h_{P-1,Q}-h_{P,Q})$$

where α^{+}, α^{-}, β^{+}, β^{-} are assigned weights.

The mass in a cell (relative to datum) is $\text{Area}_{P,Q} \cdot h_{P,Q}$, but area is proportional to the square of the radius, or $\text{Area}_{P,Q} = R_0^2 e^{2P\Delta\theta}$, see Eq. (19) of the main text. To satisfy the second property, consider the mass change in cell (P,Q) relative to adjoining cell (P+1,Q) with height difference $(h_{P+1,Q}-h_{P,Q})$,

$$\Delta M = \beta^{+}_{P,Q} R_0^2 e^{2P\Delta\theta}(h_{P+1,Q} - h_{P,Q})$$

Now advance P to P+1, for the center cell located at (P+1,Q), and the adjoining cell at (P,Q), for mass transfer

$$\Delta M = \beta^{-}_{P+1,Q} R_0^2 e^{2(P+1)\Delta\theta}(h_{P,Q} - h_{P+1,Q})$$

Accordingly the mass transfers, across a circular side which joins two adjacent rays, cancel when

$$\beta^{+}_{P,Q} e^{-\Delta\theta} = \beta^{-}_{P+1,Q} e^{\Delta\theta}$$

Similarly, across a ray side between two adjacent circles, yields the mass transfer as

$$\alpha^{+}_{P,Q} = \alpha^{-}_{P+1,Q}$$

If the above forms are to be independent of position (P,Q), then

$$\alpha^{+}_{P,Q} = \alpha^{-}_{P,Q} = \alpha \ , \ \beta^{+}_{P,Q} = \beta e^{\Delta\theta} \ , \ \beta^{-}_{P,Q} = \beta e^{-\Delta\theta}$$

for some α and β .

We can rearrange (C5) in operator form as

$$\bar{h}_{P,Q} = \begin{vmatrix} 0 & \beta e^{-\Delta\theta} & 0 \\ \alpha & 1-2\alpha-2\beta\cosh\Delta\theta & \alpha \\ 0 & \beta e^{+\Delta\theta} & 0 \end{vmatrix} \mathbf{h}_{P,Q} \qquad (C6)$$

This form conserves mass and mass flux from height-difference and retains the zero-gradient/zero-flux property. If $\alpha = \beta = 1/8$, and $\Delta\theta = 0$ (or $R_o \to \infty$), then form (C3) results. The choice of α and β, however, is restricted because it is possible to end up with an "unsmoothing" operator which conserves mass. The operator (C6) is a necessary and sufficient condition for mass conservation and the zero-gradient/zero-flux property, but it is not sufficient to damp short wave oscillations. For insight, further analysis according to behavior of particular conditions is appealed to.

A 'worst case' field requiring smoothing could be,

```
..... -1 +1 -1 +1 -1 +1 .....
..... +1 -1 +1 -1 +1 -1 .....
..... -1 +1 -1 +1 -1 +1 .....
```

and one requires the smoothed field to be zero. When this field is plugged into (C5), then,

$$\bar{h}_{P,Q} = 1 - 4\alpha - 4\beta\cosh\Delta\theta = 0 \ ,$$

or

$$\beta = \frac{1 - 4\alpha}{4\cosh\Delta\theta}$$

---

*(P,Q) is the non-dimensional coordinate system in an image plane after transformed of the (R,θ) polar system.

giving β in terms of α and reducing the degrees of freedom. A symmetric choice, giving equal effect to α and β (e.g $\Delta\theta \to 0$), is

$$\alpha = \frac{1}{8}\ ,\quad \beta = \frac{1}{4\ \cosh\Delta\theta}\ ,$$

then (C6) becomes

$$\bar{h}_{P,Q} = \frac{1}{8}\begin{vmatrix} 0 & \frac{e^{-\Delta\theta}}{\cosh\Delta\theta} & 0 \\ 1 & 4 & 1 \\ 0 & \frac{e^{\Delta\theta}}{\cosh\Delta\theta} & 0 \end{vmatrix} h_{P,Q}\ , \qquad (C7)$$

which becomes (C3) when $\Delta\theta \to 0$.

Suppose one or more of the four neighboring cells surrounding a center cell is to be ignored. Writing (C7) in a form similar to (C4), a more direct form for computer application, can be,

$$\bar{h}_{P,Q} = \frac{1}{2}h_{P,Q} + \frac{1}{8}\sum_{k=1}^{4}\ [\delta_k h_k + (1-\delta_k)h_{P,Q} + G_k\{\delta_k h_k + (1-\delta_k)h_{P,Q}\}] \qquad (C8)$$

where $h_k = h_{P\pm1,Q\pm1}$,

$$G_k = \begin{cases} 0 & \text{, for cells } (P,Q\pm1), \text{ where a side between center and adjoining cells is on a ray,} \\ \dfrac{e^{\pm\Delta\theta}}{\cosh\Delta\theta} - 1 & \text{, for cells } (P\pm1,Q), \text{ where a side between center and adjoining cells is on a circle.} \end{cases}$$

For (C1) and its complementary forms (C4) and (C8), with some $F_k = 0$ inside a field's domain (e.g., boundary cells), it can be shown the total mass is conserved. That is $\Sigma(\text{area})_{P,Q}\bar{h}_{P,Q} = \Sigma(\text{area})_{P,Q}h_{P,Q}$, for the entire field (note: for Cartesian grids, $\text{area}_{P,Q}$ = constant); this follows since during summation, F_k is encountered twice with opposite signs, or else no mass flux between cells when $\delta_k = 0$.

APPENDIX D

Stability of the Polar Grid's Difference Scheme

There are a wealth of stability studies on explicit finite difference schemes for Cartesian grids, Mesinger and Arakawa, (1976) for example. We did not attempt a deep analysis for stability on curvilinear grids, such as the polar grid scheme. Instead, we take liberties for a simplified version guided by empirical results with computer runs.

Conforming to standard approaches, consider the equations of motion in polar coordinates (Eq. (16) of the main text), without driving forces and without bottom stress. The finite difference notation of (33), then becomes

$$U^{k+1}_{m',n'} = U^{k-1}_{m',n'} - b\bar{H}^{k}_{m',n'}\,D_P h^k + aV^k_{m',n'}$$

$$V^{k+1}_{m',n'} = V^{k-1}_{m',n'} - b\bar{H}^{k}_{m',n'}\,D_Q h^k - aU^k_{m',n'} \qquad (D1)$$

$$h^{k+1}_{m,n} = h^{k-1}_{m,n} - \frac{b}{gr^2}\,(D_P U^k + D_Q V^k)$$

where

$$\bar{H}^{k}_{m,n} = \frac{1}{4}[(D+h)^k_{m,n} + (D+h)^k_{m-1,n} + (D+h)^k_{m,n-1} + (D+h)^k_{m-1,n-1}]. \qquad (D2)$$

$a = 2\Delta tf$, $b = g\Delta t/\Delta s$, $P = \ln(r/R_o) = m\Delta\theta$, $Q = \theta = n\Delta\theta$, $t = k\Delta t$

and (m,n) refers to a height point while (m',n') refers to a momentum point, see Fig. 4 of the main text. The (m',n') notation varies from the main text but is convenient for analysis by setting m' = m-1/2, n' = n-1/2.

We cannot directly use the conventional Fourier method for a stability analysis because of the Jacobian, $1/r^2$, and the non-linearity of the (D2) term. However, assuming (D2) known (the depths $D_{m,n}$ are preassigned and the height or surge $h^k_{m,n}$ takes on some upper max value) and r fixed locally at a grid point, then a local stability criteria can be ascertained when (D2) and r are fixed. Thus, the Fourier method can be used for an approximate localized stability criteria. In our scheme, r grows monotonically with increasing subscript m. If (D2) is constant, the stability criteria does not change along a circle. Because (D2) varies radically in space, then each grid point must be explored. After determining Δt, through the localized stability criteria at each grid point, one chooses the smallest Δt as the time step for the entire grid. The particular grid point with smallest Δt will not necessarily occur in deep water and can occur anywhere in the grid system depending on depth, D, the maximum surge height $h^k_{m,n}$ and r.

Using a standard approach, consider wave forms in two-dimensional space with wave numbers (α,β), then,

$$h^o_{m,n} = \underline{h}e^{i(\alpha m+\beta n)\Delta\theta},\quad (U,V)^o_{m',n'} = (\underline{u},\underline{v})e^{i(\alpha m'+\beta n')\Delta\theta}, \qquad (D3)$$

where $\underline{h},\underline{u},\underline{v}$ are not space dependent. Now let be dependent only on t and

$$h^{k\Delta t} = \lambda^k h^o,\qquad (U,V)^{k\Delta t} = \lambda^k (U,V)^o \qquad (D4)$$

so that

$$(U,V,h)^{(k+1)\Delta t} = \lambda(U,V,h)^{k\Delta t} = \lambda^2(U,V,h)^{(k-1)\Delta t} \qquad (D5)$$

To avoid exponential growth, i.e., stability, $|\lambda| \leq 1$ ($|\ |$ means the modulus if λ is complex).

The various derivatives in (D1) can now be written as

$$D_P U^k = U^k_{m'+1,n'+1} - U^k_{m',n'+1} + U^k_{m'+1,n'} - U^k_{m',n'}$$

$$= \underline{u}\, e^{i(\alpha m+\beta n)\Delta\theta}\ 4i \sin\tfrac{1}{2}\alpha\Delta\theta \cos\tfrac{1}{2}\beta\Delta\theta$$

$$D_Q V^k = \underline{v}\, e^{i(\alpha m+\beta n)\Delta\theta}\ 4i \cos\tfrac{1}{2}\alpha\Delta\theta \sin\tfrac{1}{2}\beta\Delta\theta \qquad \text{(D6)}$$

$$D_P h^k = h^k_{m,n} - h^k_{m-1,n} + h^k_{m,n-1} - h^k_{m-1,n-1}$$

$$= \underline{h}\, e^{i(\alpha m'+\beta n')\Delta\theta}\ 4i \sin\tfrac{1}{2}\alpha\Delta\theta \cos\tfrac{1}{2}\beta\Delta\theta$$

$$D_Q h^k = \underline{h}\, e^{i(\alpha m'+\beta n')\Delta\theta}\ 4i \cos\tfrac{1}{2}\alpha\Delta\theta \sin\tfrac{1}{2}\beta\Delta\theta$$

Substituting (D5), (D6) into (D1) gives the following matrix form,

$$\begin{pmatrix} \lambda-\lambda^{-1} & -a & ib\bar{H}\nu' \\ a & \lambda-\lambda^{-1} & ib\bar{H}\nu'' \\ i\frac{b}{gr^2}\nu' & i\frac{b}{gr^2}\nu'' & \lambda-\lambda^{-1} \end{pmatrix} \begin{pmatrix} U^k_{m',n'} \\ V^k_{m',n'} \\ h^k_{m,n} \end{pmatrix} = 0 \qquad \text{(D7)}$$

where $\nu' = 4 \sin\tfrac{1}{2}\alpha\Delta\theta \cos\tfrac{1}{2}\beta\Delta\theta, \nu'' = 4 \cos\tfrac{1}{2}\alpha\Delta\theta \sin\tfrac{1}{2}\beta\Delta\theta$ and $\bar{H}$ is shorthand for $\bar{H}^k_{m',n'}$. To allow a non-zero solution, the determinant of the matrix must be zero, or,

$$[(\lambda-\lambda^{-1})^2 + \frac{b^2\bar{H}}{gr^2}(\nu'^2+\nu''^2) + a^2](\lambda-\lambda^{-1}) = 0 \qquad \text{(D8)}$$

or, $\lambda^2 = 1$ (trivial case), and

$$\lambda^4-(2-S)\lambda^2+1 = 0 ,$$

$$\text{where } S = \frac{b^2\bar{H}}{gr^2}(\nu'^2+\nu''^2) + a^2 \qquad \text{(D9)}$$

The stability requirement, $|\lambda| \leq 1$, is satisfied when (D9) has complex roots, that is, when $(2-S)^2 - 4 \leq 0$, or $S \leq 4$. Hence,

$$\frac{g(\Delta t)^2\bar{H}\ (\nu'^2+\nu''^2)}{r^2(\Delta\theta)^2} + a^2 \leq 4$$

or,

$$\Delta t \leq \frac{2r\Delta\theta}{\sqrt{g\bar{H}\ (\nu'^2+\nu''^2) + 4f^2r^2(\Delta\theta)^2}} \qquad \text{(D10)}$$

The smallest upper bound for (α,β) varying is given by the upper limit of $\nu'^2+\nu''^2$. After some algebra,

$$\nu'^2+\nu''^2 = 8[\sin^2\tfrac{1}{2}(\alpha+\beta)\Delta\theta + \sin^2\tfrac{1}{2}(\alpha-\beta)\Delta\theta] \leq 16$$

since the upper limits are reached with $(\alpha\Delta\theta,\beta) = (\pm\pi,0)$ or when $(\alpha,\beta\Delta\theta) = (0,\pm\pi)$. Consequently, we obtain the upper bound of Δt

$$\Delta t \leq \frac{r\Delta\theta}{2\sqrt{g\bar{H} + f^2r^2(\Delta\theta)^2/4}} \qquad \text{(D11)}$$

Ignoring Coriolis effects, then

$$\Delta t < \frac{r\Delta\theta}{2\sqrt{g\bar{H}}} \qquad \text{(D12)}$$

Initially, with no surge present, the upper bound varies according as $r/\sqrt{D}$ depending on the polar grid of a particular basin. In general (but not always), the grid expands from inland water bodies toward the deep sea. In most basins, the critical Δt lies initially at sea, but not necessarily at the deepest grid depth in the basin. However, when surge increases across inland water bodies as a storm approaches, the critical Δt can now occur across inland water bodies. To avoid instability during a run with a particular storm, one needs to assess the smallest possible Δt required for stability across the entire basin during the residence time of a storm. By itself, (D12) is useful when designing grids and analyzing depths in a basin during the data processing stage. Later empirical test runs with a cadre of storms will give a working estimate of the smallest Δt in each basin for a given storm. These estimates are preset by the modeler for each basin and the user need not be concerned with time steps.

For economy, it is useful to change the time step at discrete time intervals during a computer run. This tactic is easily accomplished with a finite difference scheme using two-steps in time (Eq. (35) of the main text is an example). The computations are forward in the continuity equation then backward in the momentum equations. After initialization with the largest possible Δt, the time step is altered to smaller value whenever H in a localized region approaches a maximum value for stability for a given Δt. If a two-step in time scheme is used, a stability study similar to the one above gives a stability criteria of

$$\Delta t < \frac{r\Delta\theta}{\sqrt{g\bar{H}}} \qquad \text{(D13)}$$

That is, the critical Δt is twice as great compared to (D12).

(Continued from inside front cover)

NWS 21 Interduration Precipitation Relations for Storms - Southeast States. Ralph H. Frederick, March 1979, 66 p. (PB-297192)

NWS 22 The Nested Grid Model. Norman A. Phillips, April 1979, 89 p. (PB-299046)

NWS 23 Meteorological Criteria for Standard Project Hurricane and Probable Maximum Hurricane and Probable Maximum Hurricane Windfields, Gulf and East Coasts of the United States. Richard W. Schwerdt, Francis P. Ho, and Roger R. Watkins, September 1979, 348 p. (PB-80 117997)

NWS 24 A Methodology for Point-to-Area Rainfall Frequency Ratios. Vance A. Myers and Raymond M. Zehr, February 1980, 180 p. (PB80 180102)

NWS 25 Comparison of Generalized Estimates of Probable Maximum Precipitation With Greatest Observed Rainfalls. John T. Riedel and Louis C. Schreiner, March 1980, 75 p. (PB80 191463)

NWS 26 Frequency and Motion of Atlantic Tropical Cyclones. Charles J. Neuman and Michael J. Pryslak, March 1981, 64 p. (PB81 247256)

NWS 27 Interduration Precipitation Relations for Storms--Western United States. Ralph H. Frederick, John F. Miller, Francis P. Richards, and Richard W. Schwerdt, September 1981, 158 p. (PB82 230517)

NWS 28 GEM: A Statistical Weather Forecasting Procedure. Robert G. Miller, November 1981, 103 p. (PB82 192584)

NWS 29 Analyses of Elements of the Marine Environment for the Atlantic Remote Sensing Land Ocean Experiment (ARSLOE)--An Atlas for October 22 through October 27, 1980. Lawrence D. Burroughs, May 1982, 116 p. (PB82 251281)

NWS 30 The NMC Spectral Model. Joseph G. Sela, May 1982, 38 p. (PB83 115113)

NWS 31 A Monthly Averaged Climatology of Sea Surface Temperature. Richard W. Reynolds, June 1982, 37 p. (PB83 115469)

NWS 32 Pertinent Meteorological and Hurricane Tide Data for Hurricane Carla. Francis P. Ho and John F. Miller, August 1982, 111 p. (PB83 118240)

NWS 33 Evaporation Atlas for the Contiguous 48 United States. Richard K. Farnsworth and Edwin S. Thompson, December 1982, 85 p. (PB83 161729)

NWS 34 Mean Monthly, Seasonal, and Annual Pan Evaporation for the United States. Richard K. Farnsworth and Edwin S. Thompson, December 1982, 85 p. (PB83 161729)

NWS 35 Pertinent Meteorological Data for Hurricane Allen of 1980. Frances P. Ho and John F. Miller, September 1983, 73 p. (PB84 104322)

NWS 36 Water Available for Runoff for 1 to 15 Days Duration and Return Periods in the Northwest United States. Francis P. Richards, John F. Miller, Edward A. Zurndorfer, and Normalee S. Foat, April 1983, 59 p. (PB84 120591)

NWS 37 The National Weather Service Hurricane Probability Program. Robert C. Sheets, 1984, 70 p. (PB84 182757)

NWS 38 Hurricane Climatology for the Atlantic and Gulf Coasts of the United States. Marshall Hansen, April 1987, 195 p. (PB88 114657)

NWS 39 Monthly Relative Frequencies of Precipitation for the United States for 6-, 12-, and 24-h Periods. John S. Jensenius, Jr. and Mary C. Erickson. September 1987, 262 p. (Contact: John Jensenius, 301-763-8151)

NWS 40 An Eight-Year Climatology of Meteorological and SBUV Ozone Data. Ronald M. Nagatani, Alvin J. Miller, Keith W. Johnson, and Melvyn E. Gelman. March 1988, 123 p. (Contact: Ronald Nagatani, 301-763-8071)

NWS 41 A Precipitation Climatology of Five-Day Sequences. Edward S. Epstein. October 1988, 160 p. (Contact: Edward Epstein, 301-763-8155)

NWS 42 Multilevel calibration strategy for Complex Hydrologic Simulation Models. Larry E. Brazil, February 1989, 196 p. (Contact: Ginny Radcliffe, 301-713-0640)

NWS 43 A Methodology for Updating a Conceptual Snow Model With Snow Measurements. Gerald N. Day, March 1990, 133 p. (Contact: Ginny Radcliffe, 301-713-0640)

NWS 44 Functional Precision of National Weather Service Upper-Air Measurements Using VIZ Manufacturing Co. "A" Radiosonde (Model 1492-510), October 1991, p. 38. (PB92 137850)

NWS 45 Functional Precision of National Weather Service Upper-Air Measurement Using VIZ Manufacturing Co. "B" Radiosonde (Model 1492-520), October 1991, p. 39. (PB92 137868)

NWS 46 Functional Precision of National Weather Service Upper-Air Measurement Using Space Data Division Radiosonde (Model 901-10-01), October 1991, 43 p. (PB92 137843)

NWS 47 A New Perspective of Nonlinear Routing in Hydrology. George F. Smith and Wayne C. Huber, December 1991, 239 p. (Contact: Ginny Radcliffe, 301-713-0640)

NOAA SCIENTIFIC AND TECHNICAL PUBLICATIONS

The National Oceanic and Atmospheric Administration was established as part of the Department of Commerce on October 3, 1970. The Mission responsibilities of NOAA are to assess the socioeconomic impact of natural and technological changes in the environment and to monitor and predict the state of the solid Earth, the oceans and their living resources, the atmosphere, and the space environment of the Earth.

The major components of NOAA regularly produce various types of scientific and technical information in the following kinds of publications:

PROFESSIONAL PAPERS - Important definitive research results, major techniques, and special investigations.

CONTRACT AND GRANT REPORTS - Reports prepared by contractors or grantees under NOAA sponsorship.

ATLAS - Presentation of analyzed data generally in the form of maps showing distribution of rain-fall, chemical and physical conditions of oceans and atmosphere, distribution of fishes and marine mammals, ionospheric conditions, etc.

TECHNICAL SERVICE PUBLICATIONS - Reports containing data, observations, instructions, etc. A partial listing includes data serials; prediction and outlook periodicals; technical manuals, training papers, planning reports, and information serials; and miscellaneous technical publications.

TECHNICAL REPORTS - Journal quality with extensive details, mathematical developments, or data listings.

TECHNICAL MEMORANDUMS - Reports of preliminary, partial, or negative research or technology results, interim instructions, and the like.